



Faculty of Sciences
Department of Subatomic and Radiation Physics

Tomographic Imaging Techniques using Cold and Thermal Neutron Beams

by Manuel Dierick

Promotor : Prof. Dr. Luc Van Hoorebeke
Co-promotor : Prof. Dr. Ir. W. Mondelaers
Proefschrift voorgelegd tot het behalen van de graad van doctor in de
wetenschappen: natuurkunde

Academiejaar 2004-2005

Contents

| | | |
|----------|--|-----------|
| 1 | INTRODUCTION | 5 |
| 1.1 | Context of this research | 5 |
| 1.1.1 | X-ray tomography | 5 |
| 1.1.2 | Neutron tomography | 8 |
| 1.2 | The aim of this work | 9 |
| 1.3 | Major achievements of this work | 10 |
| 1.4 | The structure of this work | 12 |
| 2 | TOMOGRAPHY | 15 |
| 2.1 | Introduction | 15 |
| 2.2 | Theory | 19 |
| 2.2.1 | Parallel Beam Tomography | 19 |
| 2.2.2 | Fan beam and cone beam tomography | 27 |
| 2.3 | Neutron Tomography | 33 |
| 2.3.1 | Introduction | 33 |
| 2.3.2 | The Neutron | 33 |
| 2.3.3 | Neutrons vs. X-rays as an imaging probe | 35 |
| 2.3.4 | Status of neutron radiography and tomography | 37 |
| 2.4 | Experimental Framework | 45 |
| 2.4.1 | The basic tomography setup | 45 |
| 2.4.2 | The basic acquisition sequence | 47 |
| 2.4.3 | Acquisition and control software | 49 |
| 2.4.4 | Reconstruction software | 51 |
| 3 | OCTOPUS | 53 |
| 3.1 | Introduction | 53 |
| 3.2 | Features and User Interface | 53 |
| 3.2.1 | Data preparation | 54 |
| 3.2.2 | Reconstruction | 55 |
| 3.2.3 | Image Viewer | 58 |
| 3.2.4 | Other features | 59 |
| 3.3 | Implementation and Algorithms | 60 |
| 3.3.1 | Data preparation | 60 |

| | | |
|----------|---|-----------|
| 3.3.2 | Parallel Beam Reconstruction | 64 |
| 3.3.3 | Fan and Cone Beam Reconstruction | 72 |
| 3.3.4 | Networking | 73 |
| 3.4 | Performance | 74 |
| 3.4.1 | Timing different processing steps | 74 |
| 3.4.2 | Networking | 75 |
| 3.5 | Conclusion | 76 |
| 4 | EXPERIMENTS | 79 |
| 4.1 | Introduction | 79 |
| 4.2 | Cold Neutron Tomography at PGA | 80 |
| 4.2.1 | The SINQ spallation source | 80 |
| 4.2.2 | The PGA beamline | 80 |
| 4.2.3 | Beam characteristics | 81 |
| 4.2.4 | Experiments with the first PGA setup | 86 |
| 4.2.5 | Towards higher resolution using thinner scintillators | 91 |
| 4.2.6 | Experiments using thinner scintillators | 93 |
| 4.2.7 | Conclusion | 94 |
| 4.3 | A Focussing Neutron Lens | 95 |
| 4.3.1 | Introduction | 95 |
| 4.3.2 | The neutron lens | 95 |
| 4.3.3 | Beam characteristics | 95 |
| 4.3.4 | Experiments using the neutron lens | 98 |
| 4.3.5 | Conclusion | 99 |
| 4.4 | Measurements at NCR | 101 |
| 4.4.1 | Introduction | 101 |
| 4.4.2 | The NCR beamline | 101 |
| 4.4.3 | Experiments | 102 |
| 4.4.4 | Conclusion | 104 |
| 4.5 | Mono-energetic Neutron Tomography | 107 |
| 4.5.1 | Introduction | 107 |
| 4.5.2 | The velocity selector | 108 |
| 4.5.3 | Beam characteristics | 110 |
| 4.5.4 | Experiments | 113 |
| 4.5.5 | Conclusion | 117 |
| 4.6 | Neutron Topography at TOPSI | 119 |
| 4.6.1 | Introduction | 119 |
| 4.6.2 | Two axis neutron diffractometer TOPSI | 119 |
| 4.6.3 | The setup | 119 |
| 4.6.4 | Experiments | 123 |
| 4.6.5 | Conclusion | 127 |
| 4.7 | Dynamic Tomography at ILL | 129 |
| 4.7.1 | Introduction | 129 |
| 4.7.2 | The ILL Neutrograph beamline | 129 |

| | | |
|----------|---|------------|
| 4.7.3 | The setup | 130 |
| 4.7.4 | Optimisation of the setup | 130 |
| 4.7.5 | Beam characteristics | 132 |
| 4.7.6 | Experiments | 133 |
| 4.7.7 | Outlook | 139 |
| 4.7.8 | Conclusion | 140 |
| 5 | CONCLUSION and OUTLOOK | 141 |
| 5.1 | Conclusion | 141 |
| 5.2 | Outlook | 143 |
| 5.2.1 | Improvements of the setup | 143 |
| 5.2.2 | Software development | 144 |
| 5.2.3 | Further experiments | 145 |
| 5.2.4 | Other tomography experiments | 146 |
| A | Stepper Motor Controller | 147 |
| A.1 | Introduction | 147 |
| A.2 | Stepper Motor Theory | 148 |
| A.3 | Wiring | 149 |
| A.4 | Labview Implementation | 149 |
| A.5 | Conclusion | 151 |
| B | CCD camera characterisation | 153 |
| B.1 | Basic concepts | 153 |
| B.2 | Characteristics of the PCO Sensicam LE SVGA | 156 |
| B.2.1 | Main Features | 156 |
| B.2.2 | Quantum Efficiency | 156 |
| B.2.3 | Technical Data | 157 |
| C | Optics | 159 |
| C.1 | Optimal lens coupling | 159 |
| D | Nederlandse samenvatting | 163 |

Voorwoord

Toen ik vijf jaar geleden ervoor koos om mijn eindejaarsthesi te doen aan de elektronenversneller van het Instituut voor Nucleaire Wetenschappen kon ik niet vermoeden welke invloed dit zou hebben op mijn verdere leven. Onder leiding van Wim Mondelaers ging er voor mij een wereld open van versnellers, electronen, detectoren en straling. Als thesisstudent kreeg ik de kans om mee te gaan experimenteren aan het ESRF synchrotron in Grenoble en de neutronenbron SING in Villigen. Deze indrukwekkende top-faciliteiten hebben een blijvende indruk nagelaten en waren de bevestiging dat fysica wetenschap op zijn best is.

Ik heb dan ook niet lang getwijfeld toen de mogelijkheid zich bood om als doctoraatsbursaal in de groep te blijven werken en verder onderzoek te doen. We zijn nu vier jaar verder en ik kan terugkijken op een rijke periode vol interessante experimenten, mooie resultaten en leuke herinneringen. Daarvoor bedank ik in de eerste plaats mijn promotor Wim Mondelaers. Wim, bedankt dat je in mij geloofde en me de kans gaf dit doctoraat aan te vangen. Niet lang na de aanvang van mijn doctoraat ging Wim elders werken. Hij vond een waardige opvolger in Luc Van Hoorebeke die zich op opmerkelijke wijze in de geheimen van de versneller verdiepte. Luc nam ook het promotorschap van mijn doctoraat op zich. Luc, bedankt voor het vertrouwen en de nauwgezetheid waarmee je mijn werk hebt gelezen. Ik wens je in de toekomst minder papierwerk en meer onderzoek.

Een job zou geen goede job zijn zonder goede collega's. Ik bedank Peter Cauwels voor de goede raad die hij mij gaf bij het begin van mijn doctoraat. Jelle, onze jongste aanwinst voor de groep, bedank ik voor de gedrevenheid waarmee hij zich op het werk gooit. Wat een geluk dat we je tot tomografie konden bekeren. Bert, we werken nu al vijf jaar goed samen, we hebben veel plezier gehad en mooi werk geleverd. Onze leuze is 'al spelende leert men' en wat hebben we veel geleerd. Water, elektriciteit, planten en vissen, met LabView is alles een experimentje waard. Verder wil ik nog Pieter bedanken, voor de prachtige website van de groep. Ik bedank ook nog de mensen van het mechanisch en van het elektronisch atelier. Zonder jullie bijdragen zouden wij als experimentatoren nergens staan. Sample-houders, kleppen, elektronische sturingen, het vormden allemaal onmisbare schakels tot het bekomen van onze resultaten. Tot slot wil ik nog alle buitenlandse collega's bedanken voor de mooie samenwerkingen. Ik denk in het bijzonder aan Nikolay Kardjilov, Eberhard Lehmann en zijn groep, en Sebastien Baechler voor de experimenten aan het Paul Scherrer Instituut. Ik kijk uit naar verdere samenwerking met iedereen.

Minstens zo belangrijk als een goede job is een goede thuis. Chandra, mijn meisje, het waren drukke jaren. Samenwonen, een dochter, trouwen, ons leventje gaat als een trein. Ik weet dat het soms moeilijk was als ik je weer eens alleen achterliet voor een experiment of conferentie in het buitenland, maar ik kon altijd rekenen op je volle steun. Bedankt voor alles. Laura, bijna twee jaar geleden kwam je in ons leven en al die tijd hebben we ontzettend veel plezier beleefd. Vol verbazing staan we te kijken hoe je met een ondeugende blik de DVD-speler aansteekt. Al was het onmogelijk met jou in de buurt te werken, zonder jou was dit doctoraat veel moeilijker geweest. Mijn ouders bedank ik omdat ze me de kans gaven datgene te doen wat ik graag wou doen. Zonder hun nooit aflatende steun zou ik nooit gestaan hebben waar ik nu sta. Ik hoop dat dit doctoraat voldoening mag geven voor hun inspanningen. Bedankt. Verder dank ik nog mijn broer en zussen, schoonouders, vrienden en collega's en al wie op welke manier dan ook een positieve bijdrage levert aan mijn leven.

Manuel Dierick,

Gent, 21 maart 2005

Chapter 1

INTRODUCTION

The subject of this doctoral thesis is neutron tomography. This relatively new imaging technique exploits the penetrating abilities of neutrons to study and visualise the interior properties of objects. The basic principle behind tomography is that the interior structure of a 3-dimensional (3D) sample can be calculated based on a set of 2-dimensional (2D) projections (also called radiographies) of this sample, taken under different angles, using some form of penetrating radiation. The most common application is the medical 'computed tomography' or CT which uses X-rays to penetrate and investigate the internal parts of a patients' body. Instead of X-rays this doctoral thesis will study the use of neutrons as a penetrating probe for tomography. Neutron tomography is still very much in a developmental stage, and the main goal of this work is therefore to improve the technique, to explore and to extend the possible applications and to develop the tools needed to do so.

1.1 Context of this research

1.1.1 X-ray tomography

This research was performed within the Radiation Physics research group at the Department of Subatomic and Radiation Physics of the Ghent University. Tomography has been a research topic at the group for the last 7 years. Originally all tomography research was centred around the 15 MeV linear electron accelerator of the group. This accelerator started operation in 1987. It can produce electron beams with an energy that is continuously tunable between 2 and 15 MeV combined with a good energy resolution in the order of 1%. The electron pulse repetition frequency can be varied from single shot up to 5000 Hz, while the maximum pulse length is 10 μ s. The maximum duty factor of this pulsed machine is 2%. The electron beam current can be varied over 16 orders of magnitude, ranging from a few electrons per second up to a mean current of 2 mA. At an electron energy of 10 MeV, this corresponds to a maximum beam power of 20 kW. Nowadays, the maximum

beam current is limited to 0,5 mA. A detailed description of the machine can be found in [1]. Figure 1.1 shows the layout of the accelerator structure and the beam transport system. From left to right the following structures can be recognized: the pulser electronics (white), the electron gun (in red) followed by the prebuncher and focussing coils. Further to the right is the first accelerating section (yellow) that accelerates the electrons up to 1,75 MeV followed by the second accelerating section (also yellow) that further accelerates the electrons to their final energy. The EM field to accelerate the electrons is produced by a modulator and klystron unit seen below the sections (green). It should be noted that both sections receive their power from this single unit. The right side of the second section marks the end of the actual accelerator. To its right the beam transport system can be seen with the focussing magnets (blue) and the bending magnets (yellow) to guide the electrons to the experimental stations (see next paragraph).

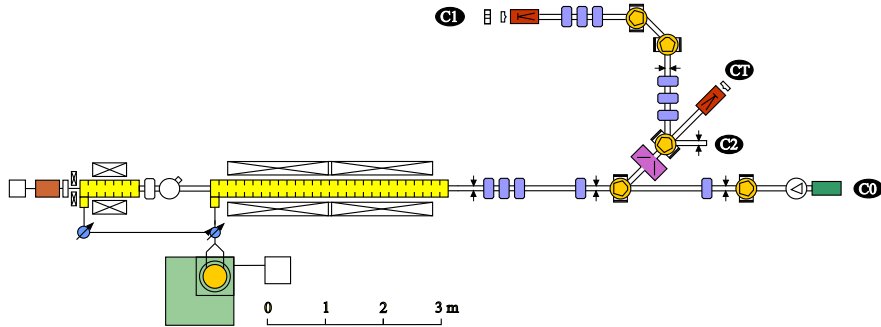


Figure 1.1: The layout of the accelerator

Originally this machine was conceived for fundamental nuclear physics research and has served this purpose for tens of thousands of hours. In recent years fundamental nuclear physics research has advanced to higher energies and large-scale international facilities. At the same time the demand from other disciplines for beamtime at the accelerator increased. Therefore the machine was gradually transformed into a more multi-disciplinary tool, thus broadening the scope of research considerably. Fields of application now include polymers, biomaterials, radiation physics, food science, electronics, medicine, agriculture... For this, four experimental beamlines are available. Two beamlines provide electron beams for high dose rate irradiations (C0 and C2 in fig.1.1). Applications include sterilisation and modification of material properties. A third beamline produces a high power X-ray beam that has been optimised for large field homogeneous irradiations (CT in fig.1.1). These X-rays are created by steering the electron beam onto a suitable target material. Upon hitting this target material the electrons are slowed down through electromagnetic interaction and give off part of their energy as X-rays, so called bremsstrahlung. The resulting spectrum

contains all energies up to the energy of the impinging electrons, typically 10 MeV. This radiation server a broad range of applications such as sterilisation of large objects, polymerisation, creating biological mutagens. . . The fourth beamline can produce a continuously tunable monochromatic X-ray beam using bremsstrahlung and diffraction (C1 in fig.1.1).

Tomographic imaging techniques were first applied at the accelerator at the tunable monochromatic X-ray source. The concept of an accelerator based tunable monochromatic X-ray source was proposed by prof. J. Jolie, at that time at the nuclear physics group at the University of Fribourg. Its functioning is based on the Bragg law of diffraction. A bent Si monocrystal is placed in the polychromatic bremsstrahlung beam in the so called Cauchois geometry. In this geometry the crystal is bent cylindrically and placed with its convex side towards the source as shown in figure 1.2a. This way the crystal redirects part of the X-rays through Bragg-diffraction in such a way that X-rays of a given energy converge on a single point [2, 3, 4, 5, 6]. For different energies these points are located on different positions along a circle, called the Rowland circle. By placing a slit system on this circle one can select the energy. The useful energy range stretches from 50 keV to about 400 keV. Among the applications we note the accurate determination of the X-ray total attenuation coefficient of (mainly) heavy elements [7].

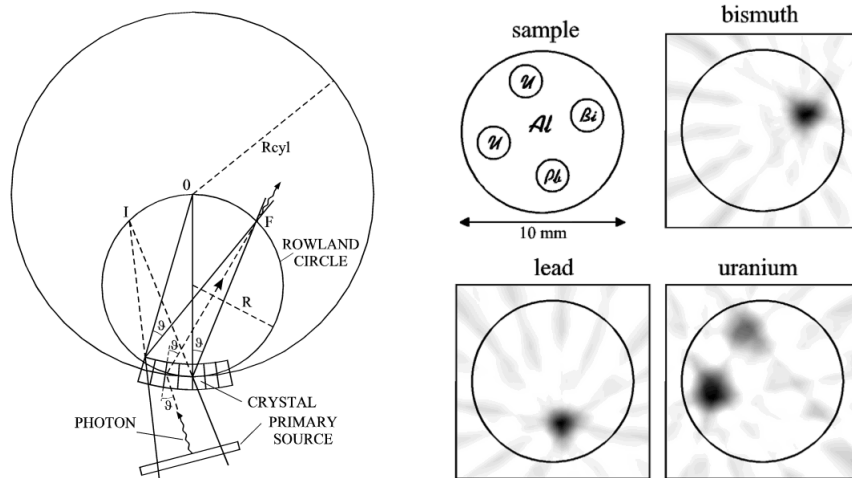


Figure 1.2: a) the monochromatic source b) element sensitive tomography

Another application is element sensitive tomography for identification of heavy elements such as uranium [8, 9]. The absorption curve of each element features specific discontinuities called absorption edges. When the photon energy increases above the binding energy of an electron in a specific shell of the atom it can eject the electron from its shell, leaving an ionised atom. This causes a sudden rise in the absorption curve. There are several of these edges, each corresponding to a different shell. The energy at which

each edge occurs depends on the selected element. If two projections are recorded, one at an energy just below a given edge and one just above that edge, then the difference image will reveal the presence of the element under study. Due to the relatively low X-ray flux the measurements were limited to a single 2D slice and were performed with a Germanium detector. Figure 1.2b shows the result of element sensitive tomography of an artificial sample containing lead, bismuth and uranium. The images had a low resolution (about 2 mm) but the different elements were successfully identified, despite their very similar atomic numbers. Even quantitative analysis proved to be possible. This was the first tomography experiment performed at the accelerator.

This technique was further developed in a series of experiments at the ESRF synchrotron facility, again in close collaboration with the nuclear physics group of the University of Fribourg. At the beamline ID15 a very intense highly monochromatic beam was available, about a million times more intense than the monochromatic source discussed above. This made it possible to record a true 3D tomography using a real 2D imaging system. This system was based on a X-ray scintillator and a very sensitive CCD camera. A stepper motor system was installed to rotate the sample. Many samples were scanned for uranium, lead, mercury. . . Spatial resolutions down to 10 μm were attained and highly detailed 3D mapping of individual elements was performed [10, 11, 12]. Quantitative analysis of different elements was also performed.

1.1.2 Neutron tomography

Another activity of the nuclear physics group of the University of Fribourg was Prompt Gamma Activation analysis (PGA) with cold neutron beams. This experiment was installed at the Paul Scherrer Institut (PSI) in Villigen (Switzerland). The neutron beam that was used in this experiment had particular characteristics that made it suitable for tomographic experiments, most importantly a high neutron flux, a large useful beam area and a homogeneous beam profile. Our collaboration was therefore extended and a series of experiments was initiated around the subject of neutron tomography.

Neutron radiography and tomography offers interesting possibilities for Non Destructive Testing (NDT). The fundamentally different characteristics of neutrons as a penetrating probe compared to X-rays opens up new possibilities. Neutrons are for example very sensitive to water or other hydrogen rich compounds. On the other hand neutrons can penetrate easily through metals such as aluminum or even lead, in contrast to X-rays. This implies that neutron tomography can yield information in cases where other NDT techniques fail. Neutron tomography already proved to be useful in many different areas such as archaeology, geology, biology, aviation. . . Currently neutron tomography still remains mainly limited to research environments

due to the lack of intense portable neutron sources. The spatial resolution of the detectors available today is relatively limited compared to that in X-ray applications. However the technique is quickly catching up with X-ray tomography in terms of performance and applicability. The first commercial neutron radiography services are emerging, offering industry new ways to study their samples in a non-destructive way [13].

All this makes neutron tomography a challenging subject with plenty of research opportunities. It has the potential to become a standard NDT technique in a broad range of fields, both scientific and industrial. Therefore the choice was made to direct research within the framework of this thesis towards the development of neutron tomography as an imaging technique and towards the exploration of new applications. These two goals required the development of a substantial set of new experimental tools. This doctoral thesis will cover the scientific research performed in this field during the last four years.

1.2 The aim of this work

- The first main goal is **the development and the improvement of neutron tomographic imaging techniques**. This involves many different parameters, but is mainly situated in three basic domains: the spatial domain, the energy domain and the temporal domain. The first and most obvious aim is improving the spatial resolution. Any imaging technique is limited by a certain spatial resolution which is either dictated by the laws of physics or, as in the case of neutron tomography, by the currently available technology. A typical spatial resolution for neutron tomography is $200\text{ }\mu\text{m}$. The second aim is the exploitation of the energy dependency of the obtained signals. Similar to X-ray beams neutron beams have a certain energy spectrum, and this can be exploited to get more information from the sample. The third aim is increasing the temporal resolution. Recording a tomography with neutrons can be a time-consuming task. Imaging of time-dependent phenomena is therefore mostly limited to 2D radiography. We will attempt 3D tomography of time dependent phenomena.
- The second main goal is **to find new applications and methods for neutron tomographic techniques**. Throughout the experiments different kinds of samples were scanned and the results investigated. Samples of both industrial and scientific nature were selected based mainly on the ability of neutrons to penetrate metals and/or sense hydrogen. Special attention was paid to finding samples that pose problems when investigated with other NDT techniques, mainly X-ray imaging. We also tested different methods and procedures to acquire the data in an optimal way.

- The third and final goal is **the development of the experimental tools needed to achieve the previous two goals**. First there is the development of a suitable experimental setup. In terms of performance it should be efficient and performant, but also in terms of practicality. It should be highly mobile, compact and modular to be applicable at a number of very different experimental locations. This requires thoughtful design. Second there is the need for equally flexible acquisition- and control-software to control the motors, camera and peripherals. The software is a key factor in the sometimes difficult experimental procedures. It should be easily adaptable to the different circumstances of individual experiments. A third and final requirement to do research on tomography is good reconstruction software. The large amounts of data, the long calculation times required to reconstruct the volumes and the specific character of different experiments led us to develop also the reconstruction software ourselves. The construction of a multi-purpose experimental setup and the development of highly performant acquisition-, control- and reconstruction software was crucial to reach the two primary goals mentioned above.

1.3 Major achievements of this work

The experimental setup

In the course of this work acquisition and control software was developed to handle all the practical aspects of a tomography experiment. This includes the camera control and readout, the motor control, and control and monitoring of peripherals such as beam monitors, counters, triggers and shutters. Many aspects were developed specifically for the experiments performed during this thesis, such as special acquisition sequences for time dependent applications or statistical procedures for extreme low light applications. A software based stepper motor controller was developed to enable faster and much more flexible motor control. This proved crucial in a series of experiments for high speed tomography. Finally everything was successfully integrated into a single user interface. The result proved to be a highly flexible and adaptable tool that served at a number of beamlines under very different conditions.

The reconstruction software

For the actual reconstruction of the acquired data a software package was developed called Octopus. In the course of this work it evolved from a set of basic routines to a full featured package. It includes routines for data preprocessing, actual reconstruction and image postprocessing. The effect of each processing step on the end result was investigated. A number of

algorithms were developed to optimize the speed and quality of the reconstruction. A server client structure was implemented to allow the reconstructions to be distributed over a network. In this way multiple computers can assist with the reconstruction, reducing the calculation time drastically. Reconstruction of a tomographic dataset is a time consuming and often repetitive task. Therefore a fully automatic reconstruction mode was implemented. This proved indispensable for the time dependent experiments where tens of tomographies were recorded of each sample. The software can handle datasets for all common beam geometries, making it applicable in other domains than neutron tomography too. Additionally an extensive image viewer was written for detailed analysis of the data.

Experimental results

With the experimental framework in place the actual experiments can be considered. The first experiments took place at the PGA beamline at PSI. The main goal was to become familiar with the technique and its possibilities, to characterize the setup and to explore new possible applications. Improvements were made in terms of spatial resolution by applying thinner scintillators, neutron collimators and a combination of both. Similar experiments were done at another beamline at PSI called NCR. At PGA we also performed experiments with a rather exotic piece of neutron optics called a neutron lens. This device focusses the incoming parallel neutron beam to a single point resulting in a divergent beam that can be used to magnify the recorded shadow image. Although not entirely successful the approach proved to have potential but needs further technological developments.

Then we turned our attention from the spatial domain to the energy domain. With the experiences with element sensitive X-ray tomography in mind an experiment was set up based on a neutron velocity selector. With this device a relatively monochromatic neutron beam can be extracted from an incoming polychromatic beam. Although the acquisition times are subsequently longer a monochromatic beam offers clear advantages for neutron radiography and tomography. It was shown that it can provide better relative image contrast and higher quality tomographic reconstructions. It can provide information that cannot be obtained using polychromatic beams. It also offers the additional advantage of an increased spatial resolution. Finally it can be used in particular cases for element identification.

A second experiment that was situated in the energy domain was neutron topography. In topography the aim is to visualise the orientation of crystal planes inside a sample. This experiment was done at the TOPSI diffractometer at PSI. The extremely low neutron flux made this experiment a real challenge. It was shown that useful information can be obtained from real-life samples. The orientation of crystal domains was successfully visualised. The goal of extending the experiment to topo-tomography was not

obtained, but the feasibility was clearly proved. This will allow visualising crystal domain orientations in three dimensions, taking full benefit of the high penetrating power of neutrons.

In a final series of experiments we addressed the time domain. Most research done in the field of time dependent neutron imaging focusses on high speed radiography. Tomography of time dependent phenomena had not been done yet. Therefore a setup was designed specifically for high speed applications. This setup was installed at the ILL in Grenoble where an extremely high neutron flux is available. As a result we could record a complete tomography in less than 10 seconds. This made it possible to monitor for example the distribution of fluids in bulk materials in 3D. These experiments are to our knowledge the first dynamic tomography experiments with neutrons ever performed. The feasibility of the technique was proven. Some clear advantages over the existing 2D techniques have been demonstrated, as well as possible applications and improvements. Specially adapted routines were developed for preprocessing, reconstructing and visualising the high amounts of data that come with such experiments. Without these routines 3D dynamic tomography experiments would not have been possible.

1.4 The structure of this work

The chapters of this thesis will be organised as follows:

After this introduction, chapter 2 will describe all aspects of tomography. First we will describe the theoretical framework of tomographic reconstruction. This is necessary to understand the different steps in the experimental procedures and the main issues to achieve good tomographic reconstructions. Two fundamentally different beam geometries are relevant here: parallel beam on one hand and fan and cone beam on the other. The case of parallel beams will be described in detail. This is the most common beam geometry in neutron tomography and is also found in synchrotron X-ray tomography. The theory for cone beam geometries will be described too since it is used in some of our experiments and is generally the most common beam geometry in other tomographic applications. Algorithms for fan and cone beam reconstruction are also included in the reconstruction software that was developed. Second we will give an overview of the current status of neutron tomography to give an impression of what is already possible, and what remains to be done. We will describe the available sources and detectors, explain how neutron tomography compares to classical X-ray tomography and show some of the typical applications. Finally we explain the practical experimental framework needed to do tomography research. This includes the basic components needed, the basic steps in the acquisition and reconstruction process, and the hardware and software that was developed for this purpose.

Chapter 3 will describe the reconstruction software that was developed for the analysis of the data generated during the experiments. During this work it evolved into a complete package for tomographic reconstruction. An important feature of Octopus is its capability to perform reconstructions in parallel by distributing the workload from the server computer to a number of client computers over a regular TCP/IP network. Octopus was the first tomography software to have this feature. It gained a lot of interest and is currently used and evaluated by a number of research groups active in neutron and X-ray imaging. It represents a major part of the effort that went into this research. An overview will be given of the features and functionality. Some of this functionality was developed specifically for particular experiments. Then the actual implementation and the algorithms that were developed will be explained. Finally we will evaluate the performance of the software.

Chapter 4 will give an extensive description of the scientific experiments performed for this doctoral thesis. These were all performed at the Paul Scherrer Institut (PSI) in Villigen (Switzerland) and the Institut Laue Langevin (ILL) in Grenoble (France), two leading facilities in the field of neutron research. The first experiments were performed in the context of the above mentioned collaboration at the PGA beamline at PSI. Subsequent experiments at PSI were carried out within the European COST action 524 (Neutron Imaging Techniques the Detection of Defects in Materials) [14]. From this other collaborations grew and experiments were performed at other beamlines at PSI (NEUTRA, NCR and TOPSI) and finally at the Neutrograph beamline at ILL. The aim of these experiments was to further develop the possibilities of neutron radiography and tomography. Obvious improvements were pursued such as higher spatial resolution and faster acquisition, but also more specialised goals such as energy selective neutron imaging or imaging of dynamic phenomena.

Finally chapter 5 will draw the conclusions on the achieved results and give an outlook on the future.

Chapter 2

TOMOGRAPHY

2.1 Introduction

Radiography is the recording of a shadow image of an optically opaque object using penetrating radiation and a recording medium. The first radiographies were recorded by Konrad Röntgen soon after he discovered the existence of X-rays in 1895 [15]. The most famous radiograph by Röntgen is shown in figure 2.1 and is often wrongly referred to as 'the first X-ray picture' and 'the hand of Mrs. Röntgen' [16]. Within months after its discovery this



Figure 2.1: One of the first and most famous radiographies with X-rays

technique was already used for medical purposes. Physicians were fascinated to see fractures, kidney stones and even bullets inside the human body. Unawareness of the possible dangers of this 'new light' is clearly illustrated by the photograph in figure 2.2 showing a person looking at his own hand with X-rays, a common practice at the time¹ [16]. Konrad Röntgen was awarded with the first Nobel prize in Physics in 1901 [17]. To this day X-ray radiography is one of the most common medical investigations.

¹Image copyright Radiology Centennial Inc., 1993

Soon all kinds of objects were being investigated with X-rays. As the detectors and sources were developed further, the range of applications broadened and the performance improved. Eventually radiography became a standard technique for non-destructive testing in industry and science.



Figure 2.2: A striking example of early radiography practice.

Tomography is an extension of radiography. In general terms it is a non-destructive technique to investigate the inner structure of an object in 3D. Basically the 3D object under study is reconstructed based on a set of 2D projections (or radiographies) taken from different angles by rotating the sample around a defined axis. The original mathematical framework was developed by Radon in 1917 [18]. It provided the solution for the reconstruction of a distribution of a given parameter based on its projections taken with a parallel beam of penetrating radiation. However it wasn't until 1972 that Hounsfield developed the first X-ray CT scanner [19]. CT quickly became a very important diagnostic tool and just 7 years after his invention Hounsfield was awarded with the Nobel prize in Medicine [20]. More recently X-ray tomography has become an important technique for non-destructive testing (NDT) in other fields too. It is used in biology, geology, archaeology, industry... For a detailed history of tomography we refer to [21]. The resulting 3D distribution can be presented to the user in different ways. Commonly the user gets to see slices through the volume, as shown in figure 2.3a, or a rendered 3D representation as shown in figure 2.3b.

Over the years the resolution of CT imaging systems has steadily improved. Modern medical scanners now have a resolution of a few hundred microns [22]. The reason for this limitation is the fact that for medical purposes the radiation dose has to be as low as possible and the radiation energy is generally limited to about 100 keV, resulting in relatively large detector elements. Non-medical devices do not suffer from dose or energy restrictions. Resolving powers below 1 micron have been achieved [23, 24]. Synchrotron

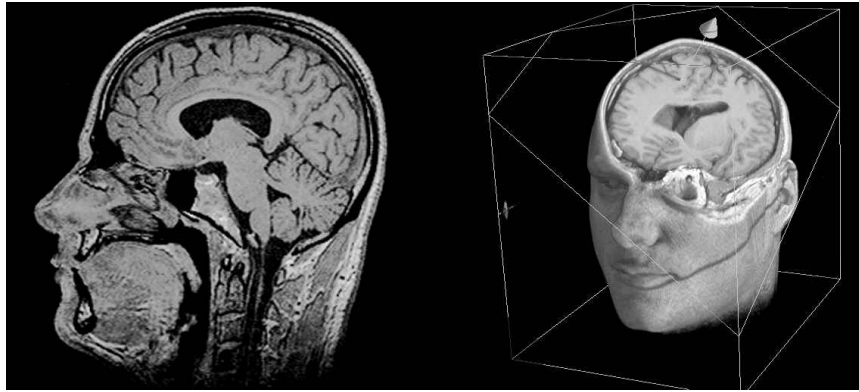


Figure 2.3: The reconstructed 3D volume presented a) as slices (left) b) as rendered volume (right)

based CT facilities have obtained resolutions of the order of tens of nanometers using specialised optical devices called Fresnel zone plates [25]. Through diffraction these devices can focus a highly parallel synchrotron beam onto a nanometre sized spot, thus transforming the beam into a divergent beam that can be used to magnify the shadow image of the sample.

X-rays are the most common probe used for tomographic imaging, but other forms of penetrating 'radiation' can be used as well to investigate different properties of an object. PET (Positron Emission Tomography) [26, 27] and SPECT (Single Photon Emission Computed Tomography) [28] use the gamma radiation emitted by radioactive tracer compounds to visualise certain features inside the human body. Optical tomography uses near-infrared light to visualise optical properties of a sample [29]. Electrical impedance or capacitance is used in industry to reconstruct the distribution of fluids and gasses inside pipes or reactor vessels [30]. Acoustic signals are used to map the the earth's inner structures (based on earthquakes) [31] or to map temperature distributions in the oceans [32]. Even radiowaves are used for ionospheric tomography [33].

Neutrons will be the probing radiation that forms the basis of this doctoral thesis. The properties of neutrons for tomographic purposes will be explained further. Neutron tomography is conceptually very much the same as classical X-ray tomography. Unlike some other kinds of tomography such as electrical impedance tomography, neutron tomography uses the same algorithms, the same scanning geometries and procedures as X-ray tomography. Of course neutron tomography has its own characteristics and peculiarities. These will be described in section 2.3.3.

2.2 Theory

In this section we will describe the theory of tomography. We will start with the parallel beam geometry. This is the most common geometry in neutron tomography due to the nature of the available neutron sources, and in synchrotron based tomography. This geometry is conceptually and mathematically the easiest. Cone beam geometry is the most common geometry besides neutron or synchrotron based tomography applications. However, it is also encountered in some neutron tomography applications as will be explained in the next chapter. In addition there is a growing trend to install X-ray tubes at existing neutron tomography facilities to enable comparative measurements. These X-ray sources also result in cone beam geometry. We will therefore describe the basics of cone beam reconstruction.

2.2.1 Parallel Beam Tomography

The theory of tomographic reconstruction using parallel beams has been extensively described in [34]. A summary will be given here. The coordinate system we will use is shown in Figure 2.4. The volume coordinate system is (x, y, z) , the projection coordinate system is (x', z) and the axis or centre of rotation is indicated by COR. Because of the parallel nature of the beam slices with different z -values are independent of each other. We will therefore only consider a single slice $f(x, y)$ and omit the index z to simplify the notations.

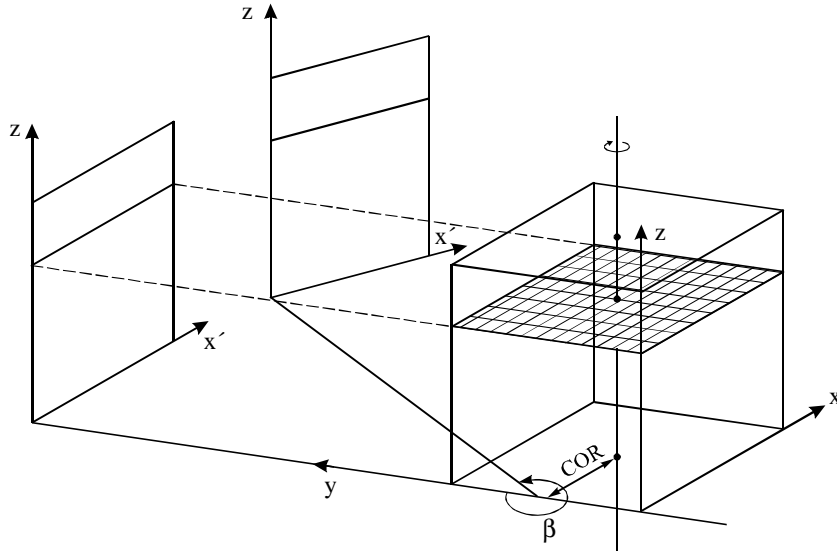


Figure 2.4: The coordinate system used for parallel beam geometry.

$$\begin{aligned}x' &= COR + (x - COR) \cos\beta + (y - COR) \sin\beta \\y' &= COR - (x - COR) \sin\beta + (y - COR) \cos\beta\end{aligned}\quad (2.1)$$

For the sake of simplicity we will put COR at zero, i.e. place the origin on the axis of rotation. We will reintroduce COR when appropriate. Let us call $I_\beta(x')$ the recorded intensity when projecting a distribution of attenuation coefficients $\mu(x, y)$ at an angle β using an impinging beam with intensity distribution $I_0(x')$. Then it follows from Lambert-Beers' attenuation law that:

$$I_\beta(x') = I_0(x') \cdot e^{-\int \mu(x, y) dy'} \quad (2.2)$$

By dividing by $I_0(x')$ and taking the natural logarithm one obtains:

$$P_\beta(x') = \ln \frac{I_\beta(x')}{I_0(x')} = - \int \mu(x, y) dy' \quad (2.3)$$

At this point we replace $-\mu(x, y)$ with a more general function $f(x, y)$. By using delta-functions the previous equation can be rewritten as:

$$P_\beta(x') = \int_{-\infty}^{\infty} \int_{-\infty}^{\infty} f(x, y) \delta(x \cos \beta + y \sin \beta - x') dx dy \quad (2.4)$$

This function is known as the Radon transform of the distribution $f(x, y)$.

The Fourier Slice Theorem

When we define the two-dimensional Fourier-transform of the distribution $f(x, y)$ as

$$F(u, v) = \int_{-\infty}^{\infty} \int_{-\infty}^{\infty} f(x, y) e^{-j2\pi(ux+vy)} dx dy \quad (2.5)$$

and consider the line along $v = 0$ then the expression simplifies to

$$F(u, 0) = \int_{-\infty}^{\infty} \int_{-\infty}^{\infty} f(x, y) e^{-j2\pi(ux)} dx dy \quad (2.6)$$

which can be rewritten as

$$F(u, 0) = \int_{-\infty}^{\infty} \left[\int_{-\infty}^{\infty} f(x, y) dy \right] e^{-j2\pi(ux)} dx \quad (2.7)$$

The term in brackets can now be recognized as $P_{\beta=0}(x)$, the projection of the distribution $f(x, y)$ at an angle $\beta = 0$, because $x' = x$ for this angle. After substitution this becomes:

$$F(u, 0) = \int_{-\infty}^{\infty} P_{\beta=0}(x) e^{-j2\pi(ux)} dx \quad (2.8)$$

The right-hand side of this expression represents the 1D Fourier transform of the projection $P_{\beta=0}(x)$. Clearly this result is independent of the angle β since the orientation of the coordinate system with regard to the distribution $f(x, y)$ is arbitrary. This therefore leads to the following general form of the Fourier Slice theorem: *The Fourier transform of a parallel projection of a distribution $f(x, y)$ taken at an angle β yields a slice of the two-dimensional transform $F(u, v)$, subtending an angle β with the u -axis.*

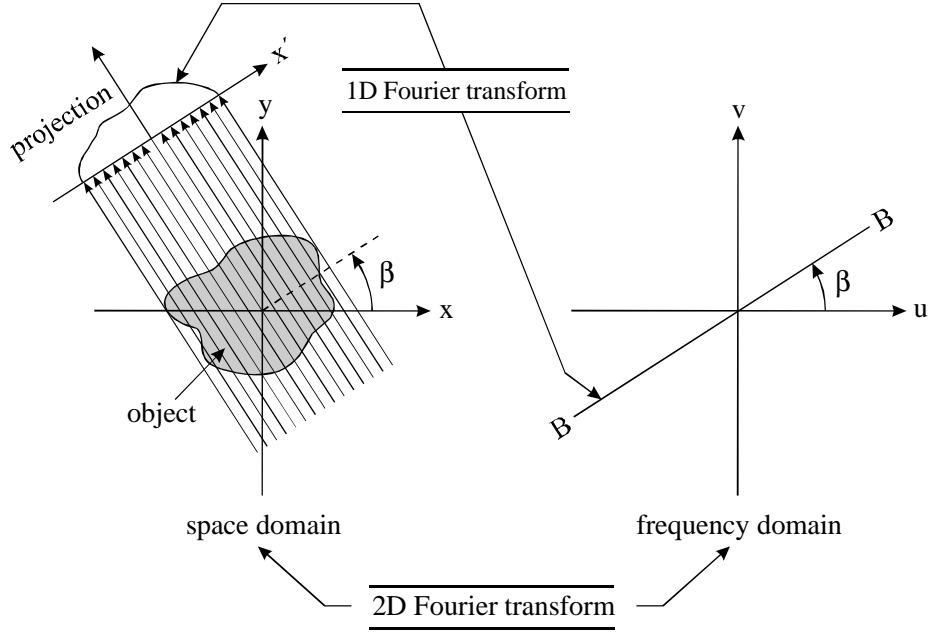


Figure 2.5: The Fourier Slice Theorem

This hands a solution to the problem of recovering a distribution $f(x, y)$ through its projections $P_{\beta}(x')$. The 1D Fourier transform of each projection $P_{\beta}(x)$ yields a slice of the 2D Fourier transform $F(u, v)$ as illustrated by figure 2.5. Given enough projections over different angles, $F(u, v)$ can be estimated completely. The wanted distribution $f(x, y)$ is then found by calculating the inverse 2D Fourier transform of $F(u, v)$. While this provides a simple conceptual model of tomography, practical implementations require a different approach.

The general form of the Fourier Slice Theorem can be derived by considering the coordinate system $x'y'$ as defined in 2.1. The 1D Fourier transform of the projection $P_{\beta}(x')$ is by definition:

$$S_{\beta}(w) = \int_{-\infty}^{\infty} P_{\beta}(x') e^{-j2\pi w x'} dx' \quad (2.9)$$

If we now replace $P_{\beta}(x')$ by its definition 2.3 but with the general function

$f(x,y)$ we get:

$$S_\beta(w) = \int_{-\infty}^{\infty} \int_{-\infty}^{\infty} f(x', y') e^{-j2\pi w x'} dx' dy' \quad (2.10)$$

Reverting to the original coordinate system (x,y) results in:

$$S_\beta(w) = \int_{-\infty}^{\infty} \int_{-\infty}^{\infty} f(x, y) e^{-j2\pi w(x \cos \beta + y \sin \beta)} dx dy \quad (2.11)$$

The right-hand side of this equation can now be recognized as the 2D Fourier transform of $f(x,y)$ at a spatial frequency of $(u = w \cos \beta, v = w \sin \beta)$. This yields in polar or rectangular coordinates respectively:

$$S_\beta(w) = F(w, \beta) = F(w \cos \beta, w \sin \beta) \quad (2.12)$$

This equation is the essence of straight ray tomography and proves the Fourier Slice Theorem.

Filtered BackProjection

$F(u,v)$ was defined as the 2D Fourier transform of $f(x,y)$. The inverse Fourier transform then gives:

$$f(x, y) = \int_{-\infty}^{\infty} \int_{-\infty}^{\infty} F(u, v) e^{j2\pi(ux+vy)} du dv \quad (2.13)$$

Exchanging the rectangular coordinate system (u, v) in the frequency domain for a polar coordinate system (w, β) by making the substitutions

$$\begin{aligned} u &= w \cos \beta \\ v &= w \sin \beta \end{aligned} \quad (2.14)$$

and then changing the differentials by using

$$du dv = w dw d\beta \quad (2.15)$$

yields the following form for the inverse 2D Fourier transform of a function $F(w, \beta)$:

$$f(x, y) = \int_0^{2\pi} \int_0^{\infty} F(w, \beta) e^{j2\pi w(x \cos \beta + y \sin \beta)} w dw d\beta \quad (2.16)$$

This can be split into two by considering β from 0° to 180° and 180° to 360° :

$$\begin{aligned} f(x, y) &= \int_0^\pi \int_0^\infty F(w, \beta) e^{j2\pi w(x \cos \beta + y \sin \beta)} w dw d\beta + \\ &\int_0^\pi \int_0^\infty F(w, \beta + \pi) e^{j2\pi w(x \cos(\beta+\pi) + y \sin(\beta+\pi))} w dw d\beta \end{aligned} \quad (2.17)$$

Using equation 2.1 and the fact that $F(w, \beta + \pi) = F(-w, \beta)$ this results in:

$$f(x, y) = \int_0^\pi \int_{-\infty}^\infty F(w, \beta) |w| e^{j2\pi w x'} dw d\beta \quad (2.18)$$

Based on the Fourier Slice theorem $F(w, \beta)$ can be substituted with $S_\beta(w)$:

$$f(x, y) = \int_0^\pi \int_{-\infty}^\infty S_\beta(w) |w| e^{j2\pi w x'} dw d\beta \quad (2.19)$$

Finally this can be expressed as:

$$f(x, y) = \int_0^\pi Q_\beta(x') d\beta \quad (2.20)$$

where

$$Q_\beta(x') = \int_{-\infty}^\infty S_\beta(w) |w| e^{j2\pi w x'} dw \quad (2.21)$$

This represents a filtering operation where the frequency response of the filter is given by $|w|$. Therefore $Q_\beta(x')$ is called a 'filtered projection'. The resulting projections for different angles β are then added to form the estimate of $f(x, y)$. The word backprojection can be explained by looking at figure 2.4. The filtered projection Q_β contributes to the reconstruction to those points in the image plane for which $x' = x \cos \beta + y \sin \beta$. Therefore one could say that in the reconstruction process each filtered projection Q_β is smeared back, or backprojected, over the image plane.

The convolution theorem states that $\mathcal{F}(f(x) * g(x)) = \mathcal{F}(f(x)) \cdot \mathcal{F}(g(x))$. Combined with the fact that $S_\beta(w) = \mathcal{F}(P_\beta(x'))$ equation 2.19 becomes:

$$f(x, y) = \int_0^\pi P_\beta(x') * h(x) d\beta \quad (2.22)$$

where $h(x) = \mathcal{F}^{-1}(|w|)$, representing the filter in spatial coordinates.

Discretisation

The inverse fourier transform of $|w|$ does not exist because the integral does not converge. However, a solution can be found when considering the fact that in practice one has only a limited number of discrete samples. From the Nyquist theorem it follows that using a detector with pixel size Δ the highest resolvable frequency is $1/2\Delta$. Therefore the integration can be limited to the frequency band $[-1/2\Delta, 1/2\Delta]$. If we define a window function $W(\omega)$ that has a value of 0 outside this band and a value of 1 inside, then the filter in frequency coordinates becomes:

$$H(w) = |w| \cdot W(w) \quad (2.23)$$

or in spatial coordinates:

$$h(x) = \int_{-1/2\Delta}^{1/2\Delta} |w| e^{j2\pi wx} dw \quad (2.24)$$

The result is:

$$\begin{aligned} h(x) &= 1/4\Delta && \text{for } x=0 \\ &= 0 && \text{for } x \text{ even and not } 0 \\ &= -1/(\Pi^2 \Delta x^2) && \text{for } x \text{ odd} \end{aligned} \quad (2.25)$$

This represents the theoretically correct filter, but limited to the frequency band $[-1/2\Delta, 1/2\Delta]$. It is therefore known as the bandlimiting filter. The highest frequencies are amplified the most, and in practical circumstances these contain mostly noise. Therefore other filters have been described that attenuate these highest frequencies, leading to smoother and better looking reconstructions [35]. Two well known filters are described below.

The Shepp-Logan filter in frequency coordinates is given by:

$$H(w) = \left| \frac{1}{\pi\Delta} \sin(\pi w\Delta) \right| \cdot W(w) \quad (2.26)$$

The result in spatial coordinates is:

$$h(x) = \frac{2}{\pi^2 \Delta (1 - 4x^2)} \quad (2.27)$$

This filter supposedly gives the best compromise between resolution and smoothness and is commonly used in medical imaging.

The Cosine filter in frequency coordinates is given by:

$$H(w) = |w| \cos(\pi w\Delta) \cdot W(w) \quad (2.28)$$

The result in spatial coordinates is:

$$h(x) = \frac{2}{\pi^2 \Delta} \left(\operatorname{sign}(x) \frac{\pi}{2} - \frac{1 + 4x^2}{1 - 4x^2} \right) \frac{1}{1 - 4x^2} \quad (2.29)$$

The cosine filter drastically reduces the high frequency content, resulting in smooth looking reconstructions. Figure 2.6 shows all three filters in frequency coordinates. Figure 2.7 shows them in spatial coordinates.

If we go back to the Fourier Slice Theorem we now notice that the discretisation implies that the frequency domain is sampled in discrete points along radial lines. If the detector consists of N elements with a width of Δ each, then the distance between two consecutive samples along a single radial line is given by $1/N\Delta$ as shown in figure 2.8. The distance between two samples on two consecutive radial lines increases towards higher frequencies.

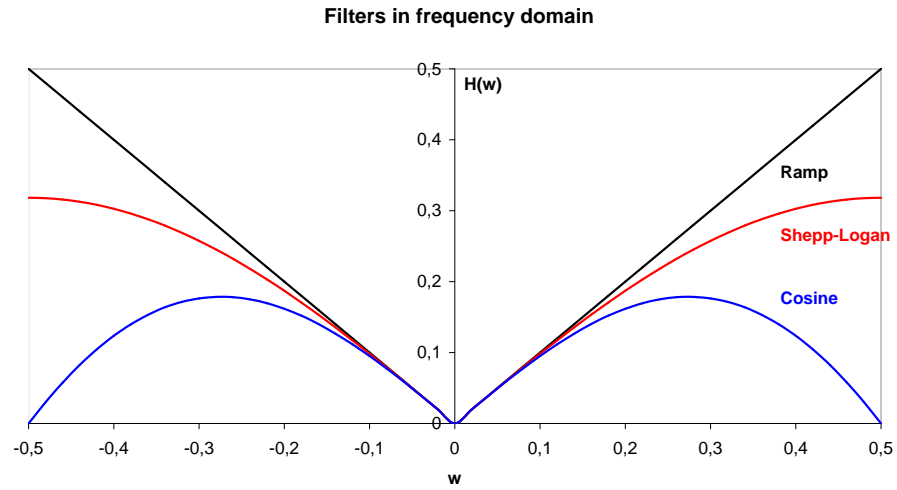


Figure 2.6: Filters in the frequency domain

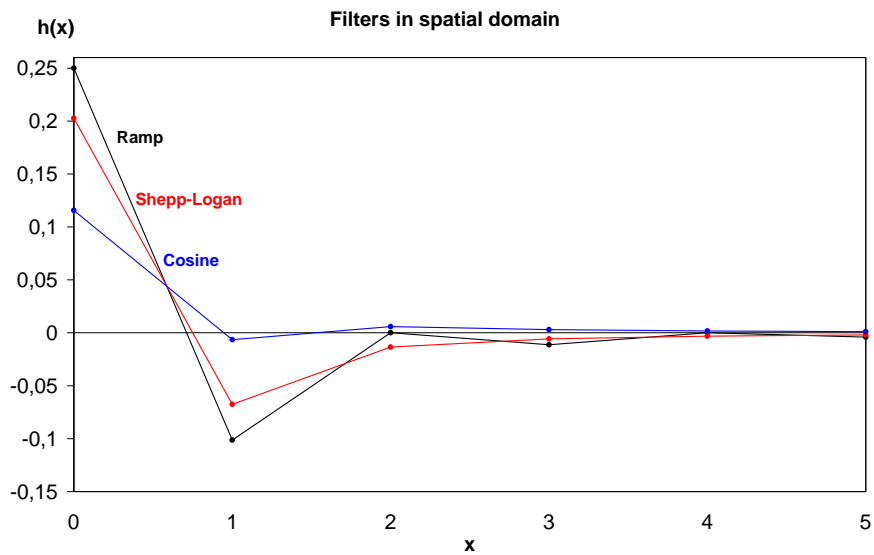
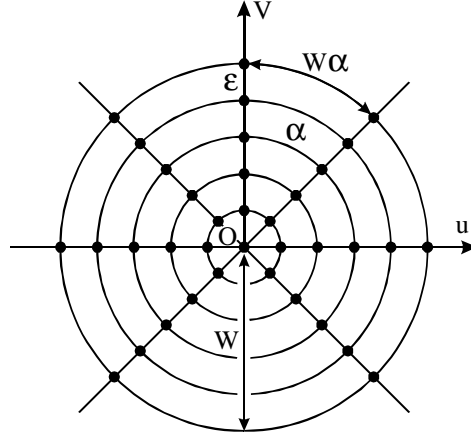


Figure 2.7: Filters in the spatial domain



frequency domain

Figure 2.8: Adequate sampling in Fourier space implies equal spacing of sampling points in both radial and angular directions

To have sufficient sampling of the frequency domain this distance should be the same as that between samples on a radial line.

If P is the number of projections then the angle between two consecutive radial lines becomes:

$$\alpha = \frac{\pi}{P} \quad (2.30)$$

From the Nyquist theorem we know that with a detector with pixel size Δ the highest resolvable frequency is $W_{max} = 1/2\Delta$. The largest distance between samples is found on the outside radius:

$$W_{max}\alpha = \frac{\pi}{2\Delta P} \quad (2.31)$$

If there are N sampling points in each projection, the total number of independent frequency domain sampling points will also be N , equally spaced on the radial line. Therefore the distance between these frequency points is:

$$\epsilon = \frac{1}{\Delta N} \quad (2.32)$$

Adequate sampling implies that the distance between points in azimuthal and radial direction are of the same order. This results in the following criterion for the number of projections P to take in order to get a good reconstruction:

$$P = \frac{\pi N}{2} \quad (2.33)$$

2.2.2 Fan beam and cone beam tomography

Fan beam geometry is most common in medical CT machines where a conical beam is used in combination with a detector that consists of a single row (a line detector). In this case only a fan of rays contributes to the recorded projection. We will not describe this geometry because it is not used in our experiments. Furthermore a simple conversion of the acquired data allows to use the parallel beam algorithm to reconstruct fan beam data. Most NDT applications with X-rays are based on X-ray tubes and a 2D detector. Such an arrangement requires a cone beam algorithm to reconstruct the recorded data. There is also a growing trend to install X-ray tubes in the existing neutron facilities to allow comparative measurements with neutrons and X-rays under identical circumstances. For these reasons a cone beam algorithm has been implemented in the reconstruction software we developed.

The cone beam geometry is much more complex than the parallel beam geometry. As shown in figure 2.9 the slices along the z -direction can no longer be treated independently because a single ray traverses different slices. Differently said a voxel² receives contributions from different detector rows when backprojecting the data. An additional problem is the fact that the intensity of the beam drops as it expands along a given direction. All this makes cone beam reconstruction more complicated, more memory demanding and slower to reconstruct.

The theory of tomographic reconstruction using cone beams has also been extensively described in [34]. The basics will be explained below. Three coordinate systems will be used as shown in figure 2.10. The (x, y, z) axes are related to the volume to reconstruct. The (t, s, z) axes are related to the detector plane. Finally the $(\tilde{t}, \tilde{s}, r)$ axes are related to the tilted fan. Any ray originating from the source can be described by the intersection of two planes:

$$\begin{aligned} t &= x \cos \beta + y \sin \beta \\ r &= -(-x \sin \beta + y \cos \beta) \sin \gamma + z \cos \gamma \end{aligned} \quad (2.34)$$

The coordinate system $(\tilde{t}, \tilde{s}, r)$ is obtained by two consecutive rotations of the (x, y, z) axes. The first rotation, as in the parallel beam case, is by β degrees yielding the (t, s, z) axes of the detector plane. The second rotation is done out of the (t, s) -plane around an axis (not drawn) parallel to the t -axis and through the source by an angle of γ . In matrix form this becomes:

$$\begin{pmatrix} \tilde{t} \\ \tilde{s} \\ r \end{pmatrix} = \begin{pmatrix} 1 & 0 & 0 \\ 0 & \cos \gamma & \sin \gamma \\ 0 & -\sin \gamma & \cos \gamma \end{pmatrix} \begin{pmatrix} \cos \beta & \sin \beta & 0 \\ \sin \beta & \cos \beta & 0 \\ 0 & 0 & 1 \end{pmatrix} \begin{pmatrix} x \\ y \\ z \end{pmatrix}$$

²A voxel is the 3D equivalent of a pixel. It is the smallest unit in a discretized volume and is identified by its (x, y, z) -coordinate.

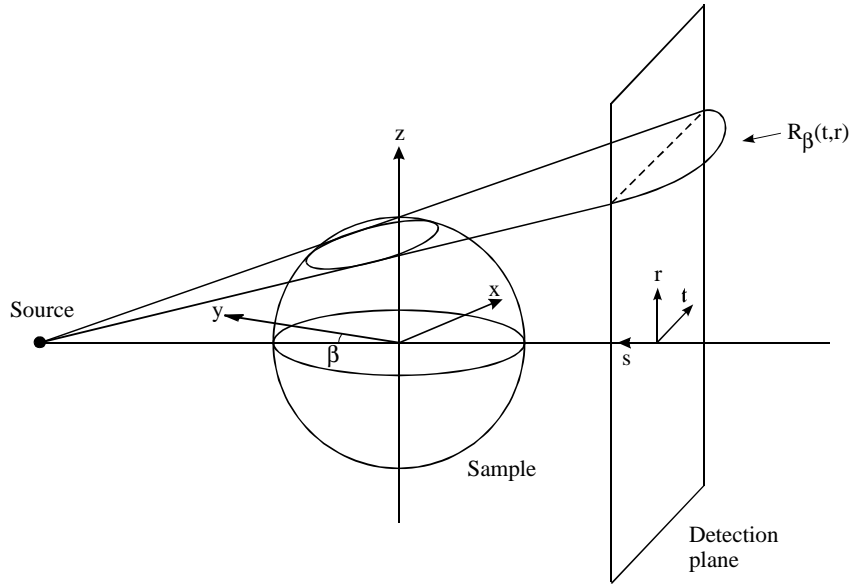


Figure 2.9: In cone beam geometry a fan of rays corresponding to a single projection traverses multiple slices

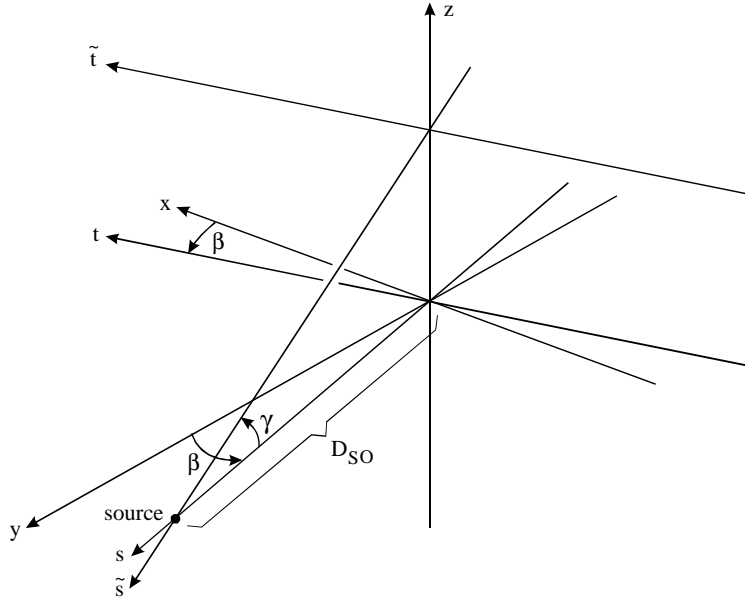


Figure 2.10: The cone beam coordinate systems. The (x, y, z) axes are transformed to $(\tilde{t}, \tilde{s}, r)$ by a rotation over β around the z -axis, followed by a rotation over γ around the axis parallel to the t -axis and through the source location

In a parallel configuration the line integral for a given ray is described by the following integral:

$$P_{\beta,\gamma}(t, r) = \int f(t, s, r) ds \quad (2.35)$$

Note that four variables are needed to describe a single ray: (t, β) for the distance and angle in the (x, y) plane and similarly (t, γ) for the (s, z) plane. In a cone beam configuration a single detector row records $R_\beta(p', \xi')$ (see figure 2.10). To find the equivalent parallel ray we first define two additional parameters:

$$p = \frac{p' D_{SO}}{D_{SO} + D_{DE}} \quad \xi = \frac{\xi' D_{SO}}{D_{SO} + D_{DE}} \quad (2.36)$$

Then it follows that for a given cone beam ray, $R_{p,\xi}$, the parallel projection ray is given by:

$$t = p \frac{D_{SO}}{\sqrt{D_{SO}^2 + p^2}} \quad \beta = \theta + \tan^{-1}(p/D_{SO}) \quad (2.37)$$

where t and β define a ray in a given tilted fan, and similarly

$$r = \xi \frac{D_{SO}}{\sqrt{D_{SO}^2 + \xi^2}} \quad \gamma = \tan^{-1}(\xi/D_{SO}) \quad (2.38)$$

where r and γ define the location of the fan itself.

Cone Beam Filtered Backprojection

We will follow the algorithm as it is described in [34]. The reconstruction is based on filtering and backprojecting a single plane within the cone. Each elevation in the cone, described by z or ξ , is considered separately and the final 3D reconstruction is obtained by summing the contribution to the object from all the tilted fan beams.

The algorithm is best derived by starting with the filtered backprojection algorithm for fan beam (not derived here, see [34]). In a cone beam geometry each fan is angled out of the source-detector plane of rotation. This leads to a change of variables in the backprojection algorithm. First consider the 2D fan beam reconstruction formula for the point (r, ϕ) :

$$g(r, \phi) = \frac{1}{2} \int_0^{2\pi} \frac{1}{U^2} \int_{-\infty}^{\infty} R_\beta(p) h(p' - p) \frac{D_{SO}}{\sqrt{D_{SO}^2 + p^2}} dp d\beta \quad (2.39)$$

$$p' = \frac{D_{SO} r \cos(\beta - \phi)}{D_{SO} + r \sin(\beta - \phi)} \quad (2.40)$$

$$h(p) = - \int_{-W}^W |\omega| e^{j\omega p} d\omega \quad (2.41)$$

$$U(r, \phi, \beta) = \frac{D_{SO} + r \sin(\beta - \phi)}{D_{SO}} \quad (2.42)$$

Here U is the distance from the source to the point defined by the projection of the point (r, ϕ) on the central ray of the fan. The function h is defined similarly as 2.22 in the parallel case. We will now replace the coordinate system (r, ϕ) by the rotated coordinates (t, s) . The expressions:

$$t = x \cos \beta + y \sin \beta \quad s = -x \sin \beta + y \cos \beta \quad (2.43)$$

$$x = r \cos \phi \quad y = r \sin \phi \quad (2.44)$$

lead to:

$$p' = \frac{D_{SO} t}{D_{SO} - s} \quad U(x, y, \beta) = \frac{D_{SO} - s}{D_{SO}} \quad (2.45)$$

$$(2.46)$$

This leads to the following expression for the fan beam reconstruction:

$$g(t, s) = \frac{1}{2} \int_0^{2\pi} \frac{D_{SO}^2}{(D_{SO} - s)^2} \int_{-\infty}^{\infty} R_{\beta}(p) h \left(\frac{D_{SO} t}{D_{SO} - s} - p \right) \frac{D_{SO}}{\sqrt{D_{SO}^2 + p^2}} dp d\beta \quad (2.47)$$

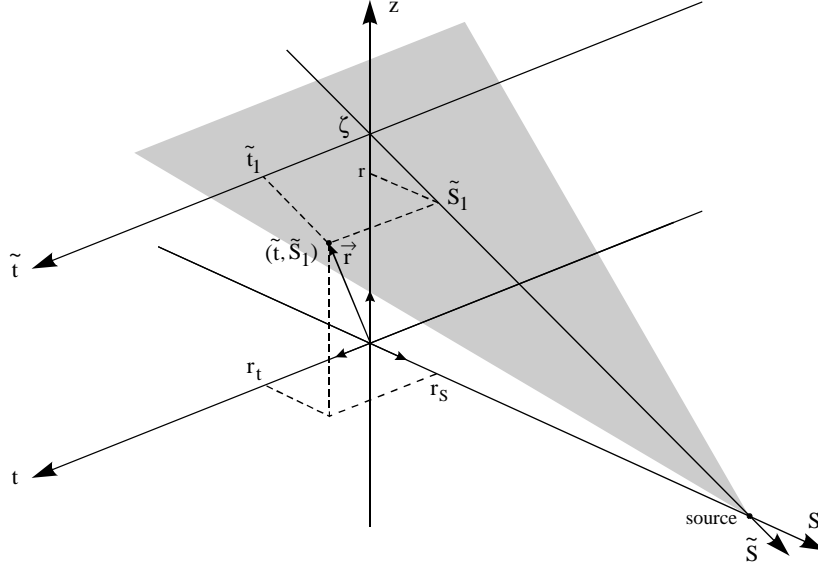


Figure 2.11: The tilted fan coordinate system

For cone beam reconstruction it is necessary to tilt the fan out of the plane of rotation. This alters the size of the fan and thus the coordinate system of the reconstructed point changes. Figure 2.11 shows how a new coordinate system (\tilde{t}, \tilde{s}) is defined that represents the location of the reconstructed point with respect to the tilted fan. Because of the changing

fan size both the source distance and the angle β change. The new source distance is given by:

$$D_{SO}'^2 = D_{SO}^2 + \zeta^2 \quad (2.48)$$

where ζ is the height of the fan above the centre of the plane of rotation. In addition, the increment of angular rotation $d\beta'$ becomes:

$$D_{SO}d\beta = D_{SO}'d\beta' \quad d\beta' = \frac{d\beta D_{SO}}{\sqrt{D_{SO}'^2 + \zeta^2}} \quad (2.49)$$

Substituting these new variables, D_{SO}' for D_{SO} and $d\beta'$ for $d\beta$, and writing the projection data as $R_{\beta'}(p, \zeta)$ 2.47 becomes:

$$g(\tilde{t}, \tilde{s}) = \frac{1}{2} \int_0^{2\pi} \frac{D_{SO}'^2}{(D_{SO}' - \tilde{s})^2} \int_{-\infty}^{\infty} R_{\beta'}(p, \zeta) h\left(\frac{D_{SO}'\tilde{t}}{D_{SO}' - \tilde{s}} - p\right) \frac{D_{SO}'}{\sqrt{D_{SO}'^2 + p^2}} dp d\beta' \quad (2.50)$$

To return to the original coordinate system (t, s, z) we make the following substitutions:

$$\tilde{t} = t \quad \frac{\tilde{s}}{D_{SO}'} = \frac{s}{D_{SO}} \quad \frac{\zeta}{D_{SO}'} = \frac{z}{D_{SO} - s} \quad (2.51)$$

combined with 2.48 and 2.49 to find eventually:

$$g(t, s) = \frac{1}{2} \int_0^{2\pi} \frac{D_{SO}^2}{(D_{SO} - s)^2} \int_{-\infty}^{\infty} R_{\beta, \zeta}(p) h\left(\frac{D_{SO}t}{D_{SO} - s} - p\right) \frac{D_{SO}}{\sqrt{D_{SO}^2 + \zeta + p^2}} dp d\beta \quad (2.52)$$

This way the cone beam algorithm can be broken down into the following three steps:

Step 1: Multiply the projection data, $R_{\beta}(p, \zeta)$ by the function $D_{SO}/\sqrt{D_{SO}^2 + \zeta^2 + p^2}$ to find $R'_{\beta}(p, \zeta)$:

$$R'_{\beta}(p, \zeta) = \frac{D_{SO}}{\sqrt{D_{SO}^2 + \zeta + p^2}} R_{\beta}(p, \zeta) \quad (2.53)$$

Step 2: Convolve the weighted projection $R'_{\beta}(p, \zeta)$ with $h(p)/2$ by multiplying their Fourier transforms with respect to p . This should be done independently for each elevation, ζ . The result, $Q_{\beta}(p, \zeta)$ is written:

$$Q_{\beta}(p, \zeta) = R'_{\beta}(p, \zeta) * \frac{1}{2}h(p) \quad (2.54)$$

Step 3: Each weighted projection is backprojected over the three-dimensional reconstruction grid:

$$g(t, s, z) = \int_0^{2\pi} \frac{D_{SO}^2}{(D_{SO} - s)^2} Q_{\beta}\left(\frac{D_{SO}t}{D_{SO} - s}, \frac{D_{SO}z}{D_{SO} - s}\right) d\beta \quad (2.55)$$

We conclude this theoretical explanation by noting that there are many forms and implementations of cone beam algorithms. Most important are the ones based on a circular source trajectory³ as presented above. In order to be able to perform an exact reconstruction the data has to meet the so called Tuy-Smith sufficiency condition [36], which states that all planes intersecting the object must intersect the source trajectory at least once. It is important to realise that in the circular cone beam geometry this condition is not met. As a result an exact reconstruction is not possible, even with an 'exact' implementation. The most common implementation for reconstruction in the circular geometry is the so called Feldkamp or FDK algorithm by Feldkamp, Davis and Kress [37]. Although the FDK algorithm is an approximative method it is a relatively simple method yielding good results for small cone angles within reasonable calculation times. For an overview of the current state-of-the-art in cone-beam tomography we refer to [38, 39].

³In medical applications the source and detector rotate around the sample. In non-medical setups the sample is rotated and the source and detector remain in place.

2.3 Neutron Tomography

In this section we will explain the details of neutron tomography. We will describe the properties of neutrons in the context of imaging applications. The historical background and current status of neutron radiography and tomography will be evaluated and compared to classical X-ray tomography. Then an overview will be given of the available technology as well as the current range of applications.

2.3.1 Introduction

Using neutrons to investigate the inner structure of objects is a rather unknown technique as opposed to using X-rays. Radiography with X-rays was already used for medical purposes just months after the actual discovery of X-rays themselves in 1895. The medical importance was immediately apparent, and the technology has evolved and improved continuously. An extra dimension was added with the advent of 3D tomography around 1972 through the work of Hounsfield and Cormack [20].

The exact same methods apply when using neutrons as an investigating probe, yet neutron radiography and neutron tomography in particular are relatively new. The main reason for this is (or was) the lack of high flux neutron beams. Possible neutron sources are nuclear reactors, spallation sources, particle accelerators and to a lesser extent radioactive sources. These are all less common than X-ray sources and more complex to build. As a consequence the equipment needed for neutron imaging has also been less developed than that for X-ray imaging, most particularly on the part of the detectors [40].

The first neutron radiographies were recorded around 1935 by Kallmann and Kuhn [41] using a Ra-Be photo-neutron source, just 3 years after the discovery of the neutron in 1932 by Chadwick [42]. After World War II many research reactors were built, boosting the neutron radiography research. Practical neutron tomography became possible when the first high power research reactors were built around 1960. A second boost came with the development of digital imaging devices such as the CCD camera [43]. Currently neutron tomography is quickly catching up with X-ray tomography [44]. However it still remains mainly limited to research environments due to the lack of intense portable neutron sources. The first commercial neutron radiography services are emerging, offering industry new ways to study their samples in a non-destructive way [13].

2.3.2 The Neutron

The modern concept of an atom as a small dense nucleus surrounded by an electron cloud emerged at the beginning of the 20th century. Rutherford

| | | | |
|-----------|-----------------------|--------------|-----------------------|
| mass | 939,56533(4) MeV | spin moment | 1/2 |
| charge | 0 C | magn. moment | -1.9130427(5) μ_N |
| radius | 8.10 ⁻¹⁶ m | quark comp. | ddu |
| mean life | 885,7 \pm 0.8 s | | |

Table 2.1: Some basic properties of the neutron [45]

discovered that this nucleus was composed of even smaller particles, protons. On a search to account for the excess mass observed in the nucleus his assistant Chadwick discovered the neutron in 1932 [42]. The neutron is an electrically neutral particle, composed of three quarks, one up-quark and two down-quarks. As a free particle the neutron is unstable, decaying into a proton, an electron and an electron antineutrino, with a half-life of $648,0 \pm 9,6$ seconds or roughly 11 minutes. Some basic properties of the neutron are listed in table 2.1 [45].

The wave-nature of the neutron is expressed through the following equation that relates the neutron's speed to its wavelength:

$$E = \frac{mv^2}{2} = \frac{h^2}{2m\lambda^2} \quad (2.56)$$

Expressed in the commonly used units [meV] and [\AA] this becomes:

$$E[\text{meV}] = \frac{81,8}{\lambda^2[\text{\AA}]} \quad (2.57)$$

It is common practice to express the energy of a neutron as a wavelength, an energy or even in terms of the speed of the neutron. According to their energy neutrons are categorized in more or less arbitrary energy ranges as shown in figure 2.12. The energy range that is important in the context of this thesis includes the cold and thermal neutron range, yet also intermediate and fast neutron beams are used for tomographic purposes. We will focus mainly on high resolution tomography of relatively small samples (sample thickness ≤ 10 cm). Especially cold neutrons with their high cross-sections are ideally suited to study very small samples (sample thickness ≤ 2 cm).

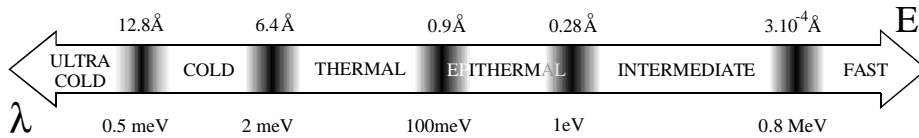


Figure 2.12: The different neutron energy ranges

2.3.3 Neutrons vs. X-rays as an imaging probe

Neutrons interact with matter in a much different way compared to X-rays. X-rays interact with the electron cloud of the atom through electro-magnetic interactions such as photo-electric effect, Compton-scattering and, for high enough energies, pair production. X-ray cross-sections increase with the atomic number Z of the atom and decrease with higher energy. This can be observed in figure 2.13 showing the total attenuation coefficient of Si (left) and Hg (right) as function of the X-ray energy [46, 47, 48]. The dominant effect over the energy range relevant for X-ray based NDT applications, roughly 10 keV to 100 keV, is the photo-electric effect. The X-ray cross-section for photo-electric effect depends on the atomic number and the X-ray energy as follows:

$$\sigma_{PE} \cong k \frac{Z^n}{h\nu^m} (cm^2/g) \quad (2.58)$$

In this equation k is a constant and m and n are energy dependent [49]. Over the relevant energy range m and n equal about 4 and 3 respectively. Notice the occurrence of strong discontinuities called 'edges'. Above a specific energy an X-ray photon can excite an electron of the atom's inner shells (K,L,...). This causes an abrupt rise in the cross-section curve. These energies are characteristic for each element and lie in the keV range.

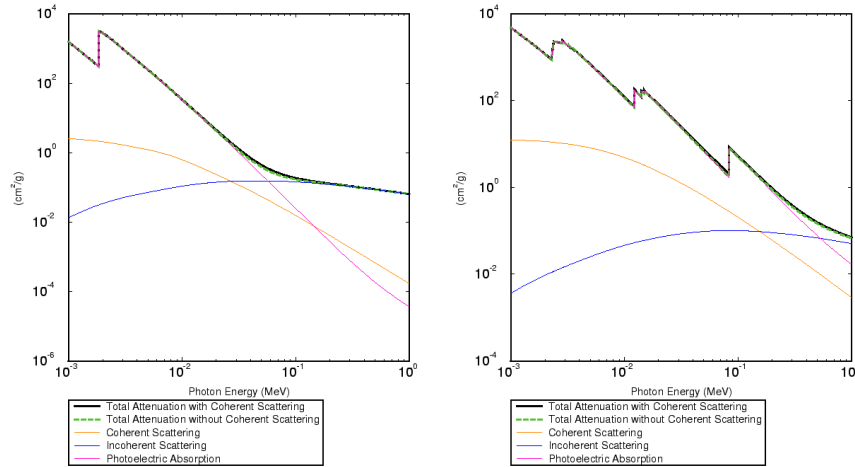


Figure 2.13: Total X-ray attenuation as function of energy for Si (left) and Hg (right)

For neutrons the situation is more complicated. Neutrons interact with the nucleus of the atom mainly through the strong interaction and to a lesser extent through the electro-magnetic interaction by their magnetic moment. The signal to look for in tomography is attenuation of the impinging beam. This beam attenuation has two distinct causes. It can be due to scattering, or due to absorption through a nuclear reaction. Scattering can be either

elastic or inelastic. At the neutron energies relevant for this work inelastic scattering does not occur and is thus irrelevant. The elastic scattering cross-section for neutrons is largely independent of the neutron energy and is composed of a coherent part and an incoherent part [50]. The coherent part is in most radiography applications irrelevant because it cannot be discerned from the neutrons that did not interact with the sample because of the small scattering angles⁴. Only in crystalline samples coherent scattering over larger angles can occur (Bragg diffraction) and should be considered. The incoherent part can present a problem for tomographic purposes, because it can result in erroneous recorded attenuations and thus bad reconstructions. This is especially true with samples containing elements having a high scattering cross-section like for example hydrogen. The absorption cross-section for neutrons with thermal energies and below is approximately inversely proportional to the neutron's speed v_n . The cross-section that is relevant for neutron radiography and tomography can therefore be expressed as:

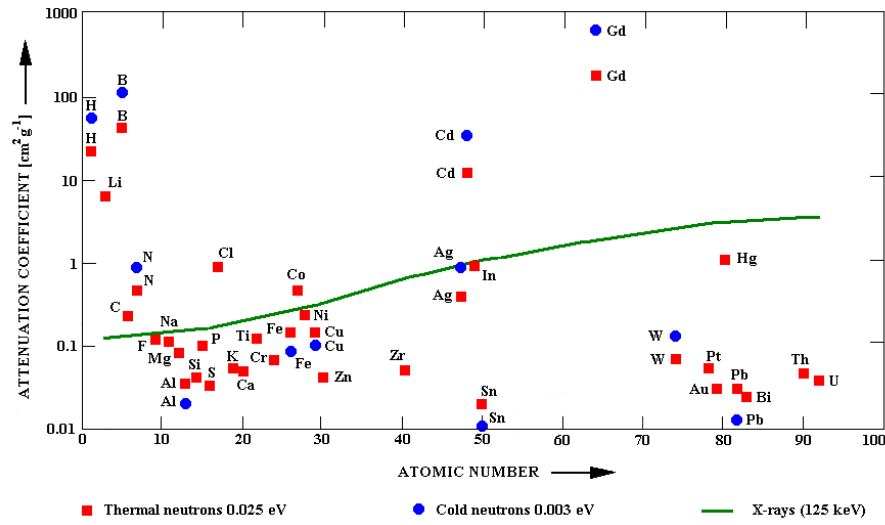
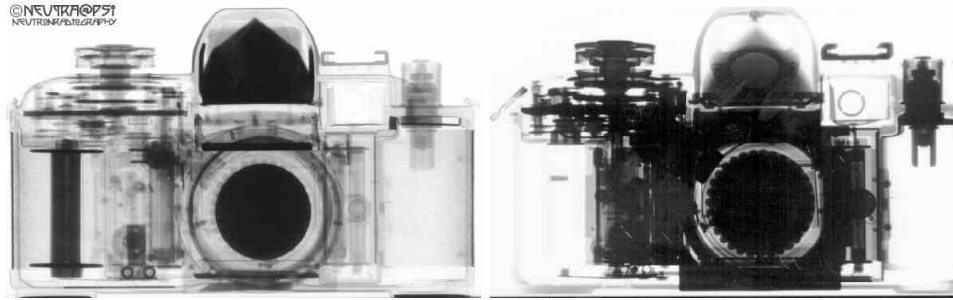
$$\sigma = \sigma_{is} + \sigma_{abs, v_{ref}} \cdot \frac{v_{ref}}{v_n} \quad (2.59)$$

where σ_{is} stands for the inelastic scattering cross-section, $\sigma_{abs, v_{ref}}$ for the absorption cross-section at a certain reference energy, and v_n for the neutron velocity (i.e. energy). At higher energies the absorption cross-section drops quickly but it can show strong resonances spread over the keV range. There is also no simple relation with Z as can be seen in figure 2.14. Light elements like hydrogen, lithium and boron show high cross-sections, but so do some heavy elements like cadmium and gadolinium. On the other hand both light elements like aluminium and heavy elements like lead are almost transparent for neutrons. As a consequence neighbouring elements in the periodic system or even isotopes of the same element can show big differences in neutron attenuation.

As a result neutron radiography yields complementary information to X-ray radiography. The high scattering cross-section of hydrogen yields a good contrast for water, organic materials, lubricants and plastics. These are typically low contrast subjects in X-ray images. The low cross-section for most metals such as for example aluminium, copper, iron, lead or uranium allows the penetration of samples that are impossible to image using X-rays.

A clear example of all this is shown in figure 2.15 (image courtesy Neutra, <http://neutra.web.psi.ch>). Notice how the neutron radiography on the left shows mainly plastic parts like the film spindle (outer left). The X-ray image on the right gives a clear view of the metal parts, while the plastic spindle is now invisible. This makes neutrons especially useful for non destructive

⁴Under special circumstances the coherent part can be used to enhance radiographic information by looking at interferences caused by phase shifts in the sample. This is called phase contrast radiography [51].

Figure 2.14: Mass attenuation coefficient versus atomic number Z Figure 2.15: Neutron radiography (left) versus X-ray radiography (right) (image courtesy [Neutra@PSI](#))

testing in situations where X-rays fail like for example samples inside metal casings. More examples and applications will be presented in the next section and in chapter 3.

2.3.4 Status of neutron radiography and tomography

Neutron facilities in the world

There are basically four kinds of sources that can be used for neutron radiography and tomography. First there are nuclear reactors, mostly dedicated research reactors. In a nuclear reactor uranium or plutonium fission is used in order to produce a controlled chain reaction that frees energy and neu-

trons.⁵ Two leading nuclear research reactors in Europe are located at ILL (Grenoble, France) and FRM-II (Garching, Germany). A second type of neutron sources are spallation sources like ISIS (Didcot, UK), SNS (Oak Ridge, USA) and SINQ (Villigen, Switzerland), where most experiments for this doctoral thesis were performed. Then there are accelerator driven sources that use D-D, D-T or other nuclear reactions. Typically deuterons or tritons are accelerated through a potential difference of the order of 100 kilovolts. They hit a deuterium target producing 2.5 MeV neutrons (D-D reaction) or a tritium target resulting in the release of 14 MeV neutrons (D-T reaction). Finally one can use neutrons emanating from radioactive nuclide sources like Ra-Be, Po-Be or Sb-Be. The first two are indirect sources in which alpha particles spontaneously emitted by radium or polonium bombard beryllium atoms and cause neutrons to be ejected out of the beryllium nuclei. In a Sb-Be source the antimony emits high energy gamma rays that eject neutrons out of the beryllium nuclei. Antimony/beryllium sources are especially used as a 'match' to start nuclear reactors. Although historically important both accelerator driven and isotopic sources are of smaller importance in terms of imaging applications, mainly due to their low neutron flux. This is especially true for tomographic purposes that require about two orders of flux extra compared to radiography.

Below follows an overview of the most important neutron research facilities in Europe:

- SINQ: The world's only continuous spallation neutron source located at the Paul Scherrer Institut near Villigen, Switzerland. Isotropic flux of $6 \cdot 10^{16}$ neutrons/s, typical flux at targets in the order of $1 \cdot 10^8$ n/cm²/s. Currently there are two beamlines for neutron imaging: [NEUTRA](#), providing thermal neutrons and [NCR](#) that will provide cold neutrons (under construction) [53].
- ILL: The Institut Laue-Langevin is an international research centre and world leader in neutron science and technology. It is located in Grenoble (France). The ILL operates the most intense neutron source in the world at the world's most powerful research reactor (58 MW). There is a dedicated beamline for neutron radiography and tomography [Neutrograph](#), thermal neutron flux at the target of $3 \cdot 10^9$ n/cm²/s, fast flux of $2 \cdot 10^7$ n/cm²/s. Main research topic is high speed dynamic radiography [54].
- FRM-II: It is the successor of the famous 'atom egg', Germany's first nuclear installation. The Forschungsreaktor MünchenII (FRM-II) started routine operation in September 2004. 20 MW producing

⁵In Oklo, a region of Gabon, 7 natural nuclear reactors operated two billion years ago. By pure coincidence all conditions were met to allow a chain reaction including a 3% high relative abundance of ²³⁵U in natural uranium and the presence of water to act as a moderator. Nowadays ²³⁵U has decayed so that this is not possible anymore anywhere on earth [52].

$8 \cdot 10^{14}$ n/cm²/s. Two dedicated beamlines for neutron radiography and tomography: [ANTARES](#) and [NECTAR](#) [55].

- BENS: The Berlin Neutron Scattering Centre at the upgraded research reactor BER II is Germany's most modern facility for cold and thermal neutron scattering research. The reactor is a 10 MW pool type reactor yielding a thermal neutron flux in the core of 10^{14} n/cm²/s. There are 7 experiments with thermal neutrons and 7 other instruments are using cold neutrons. One beamline, called [CONRAD](#), is dedicated to cold neutron tomography [56].
- ISIS: The world's brightest pulsed spallation neutron&muon source situated at Rutherford Appleton Laboratory in Didcot near Oxford, United Kingdom [57].
- BNC: The Budapest Neutron Centre has a long history of neutron radiographic imaging. This 10 MW swimming pool type reactor restarted operation in 1992 and produces a thermal core flux of 10^{14} n/cm²/s. The centre is unique in Central Europe [58].
- FRJ-2: The research reactor FRJ-2 of the Forschungszentrum Jülich (FZJ). The second most powerful research reactor in Germany [59].
- GeNF: The Geesthacht Neutron Facility (GeNF), part of GeNeSyS, the Geesthacht Neutron and Synchrotron Scattering Facility by the GKSS Forschungs-zentrum Geesthacht near Hamburg, Germany. One dedicated beamline for radiography called [GENRA-3](#) [60].
- LLB: The Laboratoire Léon Brillouin (CEA/CNRS) is a French laboratory which aim is to carry out fundamental and applied research using neutron beams supplied by the reactor Orphe [61].
- NPI-Rez: The Rez Neutron Physics Laboratory has been established in the frame of Nuclear Physics Institute of the Czech Academy of Sciences, in order to perform neutron physics experiments [62].

Some of the other facilities worldwide:

- LANSCE: Los Alamos Neutron Science Center, Los Alamos, USA. A 800-MeV proton linear accelerator feeding a spallation source. Mainly for scattering research [63].
- MNR: McMaster Nuclear Reactor at McMaster University, Hamilton, Canada. A 5 MW pool-type reactor from 1958. Active in neutron imaging, mainly radiography [64].
- NIST: Center for Neutron Research at the National Institute of Standards and Technology, Gaithersburg, USA. Advanced thermal and cold neutron source [65].
- HANARO: Korea Atomic Energy Research Institute, Taejon, South-Korea, a 30 MW open-tank-in-pool reactor from 1996. Mostly doing scattering experiments, but there is a dedicated radiography beamline NRF [66].
- JAERI: Japan Atomic Energy Research Institute, Tokai, Japan, a 125 MW heavy water reactor, started operation in 1990. Mainly scattering experiments [67].
- NECSA: Nuclear Energy Corporation of South Africa, Pelindaba, South Africa, a 20 MW swimming pool-type reactor (SAFARI-1), 1965, light-water-cooled and -moderated reactor [68].
- SNS: Spallation Neutron Source, Oak Ridge, USA. Under construction. To be completed in 2006. This accelerator based spallation source will produce the most intense pulsed neutron source in the world with an expected peak neutron flux of 20-100 times the flux at ILL [69].

For more information and references we refer to the following websites:

- European Neutron Portal : <http://neutron.neutron-eu.net/>
- Nanopolis portal : <http://www.nanopolis.net/>.

Neutron imaging detectors

In terms of spatial resolution neutron imaging is still clearly behind on X-ray imaging. This is mainly due to two reasons. First, the intrinsic resolution of neutron sources is limited due to the way they are made. This will be explained further. Second, the detection process of neutrons is fundamentally different from that of X-rays. Being neutral particles neutrons need an indirect detection process causing extra blurring. This secondary process can be either capture, fission or a collision. A lot of work is currently done on the development of better neutron detectors. Since the beginning of radiography film has long been the only available detector. Neutron radiography used the same X-ray sensitive films, but coupled to a converter. This has been the case for many decades, up to about 15 years ago. Since then a myriad of new detector technologies has emerged, mostly in the footsteps of X-ray developments. These pushed the limitations in both spatial and temporal resolution as can be seen in figure 2.16 (figure courtesy [Neutra@PSI](#)). The values in this figure are valid under the conditions at the NEUTRA beamline. These are described in [70]

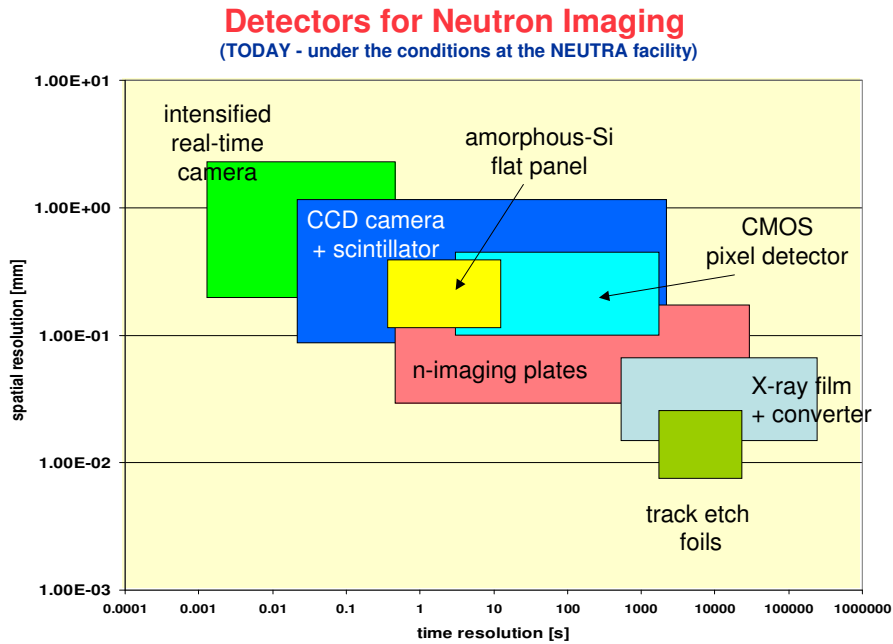


Figure 2.16: Application range for current neutron detector technologies

- Photographic film: this was the first detector and is still being used today for radiographic purposes. Film blackens by interaction with gamma radiation or secondary electrons. To act as a neutron detector converter foils like Gd are therefore needed.
- Track-etch foils: these are plastic foils coated with lithium-borate. Neutrons hitting the foil can interact through capture by the B-10, yielding α - particles. These heavy ions will produce tracks in the plastic where the molecules are damaged. This can be rendered visible by etching of the plastic with a suitable reagent. This kind of detector is unsuited for tomographic applications, but can yield high resolution radiographies.
- Imaging plates: imaging plates contain Gd as neutron absorber and BaFBr:Eu $2+$ as the agent which stores a photoluminescence signal as a measure of the neutron exposure. An imaging plate scanner then extracts the latent image information as a digitised data file from the plates by de-excitation caused by a laser signal. This detector type is unsuited for tomography, but ideal for high resolution radiography with an excellent dynamic range.
- CCD + scintillator: this represents the most common detector system in neutron tomography. A CCD camera, mostly cooled to sub-zero temperatures to allow long exposures, records the light emitted by a neutron sensitive scintillator screen. This kind of setup is highly convenient because it covers a broad range in both spatial and temporal terms. It can offer high resolution ($100\text{ }\mu\text{m}$) but can also be used for imaging large objects (40 cm). Similarly it can serve for high-speed applications (ms) as well as extreme low-light situations (1 hour). A CCD based setup offers a good dynamic range and excellent linearity, making it ideal for quantitative measurements. However it is not very efficient due to the loss of light in the coupling between scintillator and detector.
- Image Intensifiers: image intensifiers such as e.g. multi channel plates (MCP) are used in combination with CCD-cameras or even with less sensitive video-cameras. Through a multiplication mechanism of some kind they can boost the signal so that very high frame rates become possible. Such systems are less suitable for tomography due to the bad dynamic range (low signal to noise ratio). They are mostly used for high speed radiography of dynamic phenomena.
- Flat Panel detectors: this highly promising new technology is developed mainly for medical digital radiography [71, 72, 73]. The most important types are aSi:H (amorphous silicon), aSe (amorphous selenium) and finally CMOS flat panels. The amorphous types have the advantage of being inherently radiation resistant. The aSi:H type is a so called indirect conversion detector. This type of flat-panel sensor

uses thin films of silicon integrated with arrays of photodiodes. These photodiodes are coated with a scintillator (often crystalline caesium iodide or Gadox). The light photons are then converted into an electric charge by the photodiode arrays. The selenium-based technology uses an amorphous selenium-coated thin-film-transistor (TFT) array to capture and convert X-ray energy directly into digital signals. It is a direct-conversion technology that converts X-ray beams into electric charges directly. CMOS flat panels are basically different in the sense that they are made from a crystalline substrate and that each pixel has its own electronic amplifier at the pixel position. This makes them more sensitive to radiation damage. CMOS detectors are an indirect detector using a scintillator material. Application of flat panels for neutron imaging requires indirect type flat panels with specially adapted scintillators [74].

Neutron imaging applications

Some examples of scientific applications that have been demonstrated to date are:

- study of archaeological samples, in particular metallic artefacts that are too dense for X-ray examinations
- study of geological samples, also particularly suited for highly metallic rocks or water flow studies
- study of biological samples, based on the high sensitivity to water, e.g. plant roots or wood
- study of new technologies, e.g. real-time study of the hydrogen distribution in fuel cells
- study of distribution of certain chemicals

Some examples of industrial applications:

- inspection of turbine blades for aviation industry
- inspection of fuel distribution in running engines for car industry
- inspection of explosives
- detection of water intrusion
- detection of internal flaws such as cracks, inclusions, voids, bubbles, foreign materials, density variations and misalignments
- detection of bonding flaws in adhesives
- inspection of samples encased in metals, e.g. capacitor delamination
- inspection of radioactive objects through their shielding
- reliability of air bag or parachute initiators
- quality control for missing, wrongly placed or damaged O-rings

2.4 Experimental Framework

In this section we will sketch the practical side of our tomography research. We will describe the basic components that make up a tomography setup. The basic acquisition sequence will be explained step by step. It has already been mentioned before that to achieve the goals that were set out for this work a flexible and performant setup is needed in combination with equally flexible and performant software, for acquisition and control as well as for reconstruction. The highly variable experimental conditions between different experiments forced us to do all this development ourselves. An overview will follow of the acquisition and control software that was developed to make the experiments possible. The reconstruction software will be introduced, but the actual detailed description will follow in the next chapter because it represents a major part of the work done for this doctoral thesis.

2.4.1 The basic tomography setup

The basic tomography setup as it will be described here is used in more or less the same form in all the experiments. It is based on a CCD camera and a scintillator coupled with a lens⁶ as can be seen in figure 2.17. This modular setup allows for maximum flexibility, allowing it to be installed at almost any beamline. So far this setup served at at least seven beamlines, both with X-ray and neutron beams.

The camera box

The CCD camera is a Sensicam SVGA Long Exposure from PCO⁷ with a resolution of 1280x1024 pixels spanning 8,6x6,9 mm². The dynamic range is 12 bit (4096 grey-values) and the chip is Peltier cooled to -12 °C to reduce electronic noise. This is especially important in low light-level situations where long exposure times are needed. It has a fast readout time of 8 frames per second and communication with the PC happens through a fibre optic link and a PCI interface board. More details on the camera can be found in appendix B. The camera is mounted in a light-tight box that can be shielded from gamma rays with lead. A mirror bends the lightpath 90 degrees so that the camera is not positioned in the direct beam. This would cause noise in the images, activation of the camera and possible damage to the electronics. To avoid long term activation by neutrons the mirror is not the usual glass with a silver coating. Instead it is made of polished aluminium and titanium. This also ensures a good reflectivity of 90% at the wavelength of 460 nm emitted by the scintillator. In front of the lens a

⁶Another way of imaging the scintillator on the CCD is through a fibre optic taper, a bundle of optic fibres that guides the scintillator light directly to the CCD chip

⁷<http://www.pco.de>

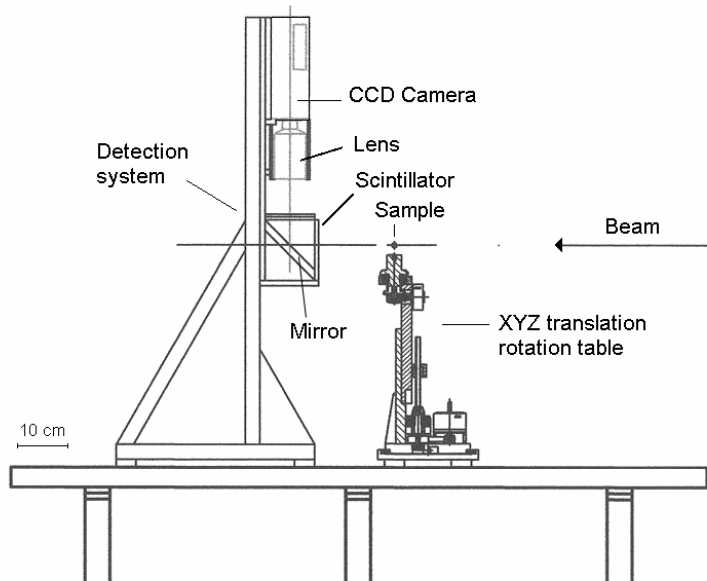
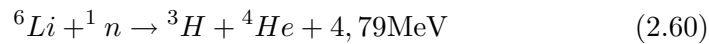


Figure 2.17: The basic components of our tomography setup include a sample stage, a scintillator, a mirror, a lens and the CCD camera

lead glass can be placed to shield the CCD from gamma rays scattered at the mirror or caused by radioactive decay due to activation. Additionally lithium or boron containing sheets can be added to shield the setup from neutrons. Different lenses can be used depending on the desired field of view, resolution and geometry of the setup. Focussing of the lens is done manually prior to the actual experiment.

The scintillator

The standard scintillator used for converting the neutrons to a visible light signal is a ${}^6\text{LiF}/\text{ZnS:Ag}$ screen (ND type) manufactured by Applied Scintillation Technologies⁸. It consists of a mixture of ${}^6\text{LiF}$ and ZnS:Ag phosphor, stabilised in an acrylic binder. Its function is based on the following reaction:



It relies on the very high neutron cross-section and low Z of ${}^6\text{Li}$ to give both a good sensitivity and a good X-ray discrimination. The ejected tritons and alpha particles interacting with the phosphor create the actual scintillation event. The range of these reaction products determines the intrinsic resolution. The technical specifications can be found in Table 2.2. The light emission peaks at a wavelength of 460 nm. This gives an excellent match

⁸<http://www.appscintech.com>

with the spectral sensitivity of the CCD camera, peaking around 480 nm. The scintillator is not transparent for its own emission, so the thickness is limited. Each detected neutron creates in the order of 10^5 visible photons, emitted in 4π . A reflective aluminium backing reflects backwards emitted photons to the forward side to increase the intrinsic efficiency. This however also decreases the effective resolution of the screen.

| | |
|-------------------------------------|--------------------------------|
| phosphor : ND ($^6\text{LiF:Ag}$) | peak emission : 460 nm (blue) |
| density : 2.4 g/cm ³ | decay time (10%) : 80 us |
| thickness : 0.42 mm | MTF@10% : 6 lp/mm (160 μ) |

Table 2.2: AST Scintillator specifications

The motor stage

The samples are placed on a 3 axis motor stage. Two axis are for translation and one for rotation. A horizontal axis perpendicular to the beam direction allows to move the sample out of the beam to take normalisation images. The typical range is 10 cm. A vertical axis allows samples higher than the beam height to be scanned in several layers. The typical range here is 15 cm. This axis is optional and not installed in every setup. The final axis is the essential rotational axis. It is a stepper motor with a main step resolution of 0,9° per step. This means 200 steps for one 180° tomography, or 400 steps when driven in half step mode. This is sufficient for most applications. The original motor control was done by hardware communicating with the PC through a serial link. In the course of this work an improved controller was developed for high speed applications. More information on this and the stepper motors can be found in appendix A.

2.4.2 The basic acquisition sequence

Preparing the setup

Before every experiment the setup has to be aligned carefully. The easiest way to do this is to place a laser at the beam exit and point it along the central ray of the neutron beam. First the mirror is positioned so that the laser beam is reflected at a perfect 90 degree angle and in the horizontal plane through the centre of the neutron beam. After that the camera is aligned so that the reflected laser beam hits the detector plane perpendicularly and in the centre. Care is taken not to expose the CCD chip to this direct laser beam to avoid possible damage. The camera should be aligned so that the pixel rows are perfectly horizontal (there can be a slight deviation between the orientation of the CCD rows and the exterior body of the camera, so this has to be judged from recorded images). As a next step the sample

stage can be placed. It is important that the axis of rotation is perfectly vertical and crosses the centre of the neutron beam. Avoiding tilting of the axis towards the scintillator is particularly critical because this cannot be corrected by software in any way. Next the scintillator can be placed between the sample stage and the camera. It is important that the scintillator is as flat as possible (using a suitable backing or frame) and perpendicular to the central ray in the neutron beam. At this point the field of view, i.e. the image area on the scintillator that is recorded by the camera, can be verified. Next the lens should be focussed on the scintillator. To do so, a printed pattern or text is attached to the scintillator. One should realise that the depth of focus in these setups is very limited. This has several reasons. One reason is the fact that to collect the maximum amount of light possible the aperture of the lens is completely open in most experiments. This reduces the depth of focus. Another reason is the fact that the camera is often closer to the scintillator than the focus range of common lenses. Therefore distance rings are used to bring the focus closer. This also strongly reduces depth of focus. So it is important to verify that the pattern is really against the scintillator, a few millimetres can make a big difference in the resolving power of the final setup.

When everything is aligned the shielding can be placed around the camera and other components. To shield against neutrons one commonly uses boron sheets. To shield against gamma rays from the reactor or due to activation lead bricks are used. Finally the setup is shielded from stray light using tape or dark cloth. After everything is put in place the motors and the limit switches are connected to the controlling PC. In some cases so called peripherals like beam monitors, beam shutters or counters are also connected to the PC. More details on this will follow in the next section when the acquisition and control software is explained.

Finally the sample is placed on the rotation table. It is important to verify that the sample is inside the field of view for all angles during the acquisition and that it does not hit the scintillator. The alignment of the axis of rotation and the vertical axis is again verified using two projections with a 180 degree difference. The sample should be stable so that it does not move during the acquisition.

The actual acquisition

As a first step one should determine the right exposure under the given conditions. This can be done manually or using an automated procedure provided in the software. Then one should measure the resolution of the setup. This is done by imaging the edge of a thin foil of highly absorbing material. This procedure will be explained in chapter 4. From this it can be decided if it is necessary to use the full resolution of the CCD chip or if the images can be 'binned'. Binning is a hardware procedure in the

CCD camera where neighbouring pixels are combined to produce a lower resolution image. Important benefits are shorter exposure times, lower noise levels, faster readout and reduced amounts of data.

Once the binning and exposure have been set the actual acquisition can start. First one should record dark current images or offset images. This is done by recording an image with the lens covered and the exposure time that will be used in the experiment. The resulting image gives an estimate of a number of noise contributions typical for CCD-camera's (see Appendix B for more details). Most important are the dark current, the ADC offset value and the readout noise. For statistical reasons it is best to record multiple dark images, typically about 10.

After that, beam profile images are recorded. For statistical reasons it is best to record many beam profile images, typically about 20. This is a crucial step in order to obtain good tomographies since every recorded projection will be divided by the resulting beam profile. Therefore any deviation in the recorded beam profile will have its effect on every projection.

Now the actual tomography is recorded. Therefore the sample is moved into the beam using the horizontal translation motor and the first projection is recorded. Then the motor rotates the sample to the next angle and the second projection is recorded. This continues until the last projection is recorded. In case the sample is too high to scan in one go it can be scanned in several layers. If so the sample is to be rotated back to the starting angle and translated in the vertical direction after which another series of projections can be recorded. In some cases a second set of beam profile images is recorded at the end of the scan. This is the case when for example the scintillator degrades noticeably during a single scan.

2.4.3 Acquisition and control software

The acquisition and control software handles the interface between the user and all the hardware involved in a tomography experiment. Everything was developed on a single platform, LabVIEW. There are three basic blocks in the software as illustrated by the block diagram in figure 2.18. One is the camera control and readout, a second is the motor controller and a third handles all the peripherals such as limit switches for the linear motor stage, beam monitors, counters or shutters. The close synchronisation that is required between these blocks is situated completely on the software level.

The camera control

For optimal control over the camera the function libraries (in the form of dll-files) that were delivered with the camera were integrated in the LabVIEW code. Two modes of operation are possible. There is the normal mode where an image is exposed, read out and written directly to harddisk. For high-

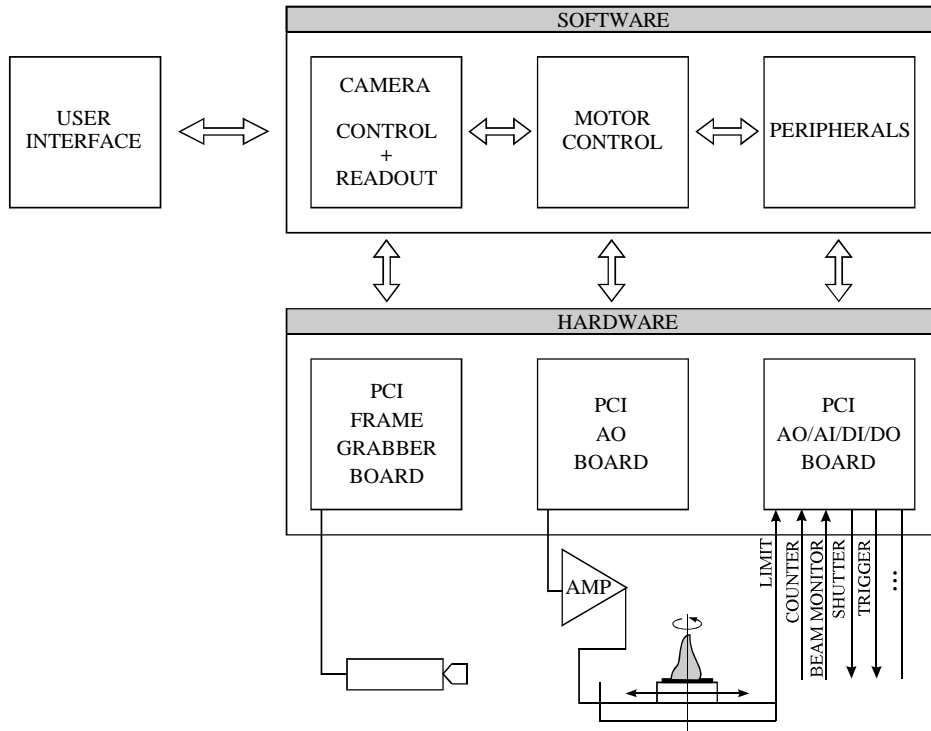


Figure 2.18: Block diagram of the acquisition and control software

speed applications there is also a DMA mode (Direct Memory Access) where the image is read out to the computer's main memory. Then the images are written to harddisk after the acquisition has finished. This mode requires a lot of memory in the acquisition PC. More details on the camera can be found in appendix B.

The motor controller

To achieve accurate rotational positioning of the sample one normally applies stepper motors with a high number of primary steps. Most stepper motor systems are composed of a digital controller, a driver (amplifier) and the motor itself. Digital pulses are sent to the controller and translated to voltage levels that are in turn amplified and put on the motor's windings. The controllers and amplifiers available for our experiments were custom built by the electronic workshop of the University of Fribourg. The controllers received commands from the PC through a serial port connector and those commands were then processed by software that was stored in EPROM chips.

There were a few problems with this approach. First of all it was slow. One cycle of sending a command, executing the motion and receiving con-

firmation took about 4 seconds. For high speed experiments like dynamical tomography this is orders too slow. Secondly there was only limited control over parameters such as speed, acceleration and step resolution. Finally the EPROM chips in the controller started to fail due to age and radiation damage. One after the other started having problems due to the deterioration of the chips. A new controller to control the amplifiers was therefore needed. Some research quickly showed that the custom built system could not be fitted with an industry standard controller because of the particular way the amplifiers were wired to the motors. Therefore a radical approach was taken to generate the voltages for the motor windings directly from LabVIEW using an analog output board, eliminating the need for a separate controller. This gave us excellent control over the motors and allowed for the best possible integration with the existing software without any overhead. The actual implementation of this controller is described in Appendix A.

Peripherals

During an experiment there are a number of so called peripherals to be monitored or controlled. There are input and output peripherals. Input peripherals are for example the limit switches of the linear motors. These are monitored to ensure that the motors don't run against the end of the shaft due to a wrong command, since this could damage the shaft. These switches are monitored in a so called watchdog loop that runs in parallel with the other parts of the software. Counters or beam monitors are input peripherals that can be monitored to record the intensity of the beam. This can be useful during the acquisition. Neutron beams, especially at spallation sources can be quite unstable. By using a beam monitor it is possible to set a threshold on the recorded intensity. If the beam intensity drops below this threshold the acquisition can be put on hold automatically until the beam intensity returns to an acceptable level. The recorded value of the beam monitor is also stored in the file header and can be used later for normalisation of the images. An example of an output peripheral is a beam shutter. Because neutron beams cause activation of everything inside the experimental bunker it is important to minimize the exposure. Some neutron beamlines are therefore equipped with small pneumatically operated shutters. Usually this is operated remotely by hand. A routine was implemented in the acquisition software to operate a shutter automatically by linking the software generated trigger signal to the shutter control box. This way the exposure was reduced to an absolute minimum.

2.4.4 Reconstruction software

Once the data has been acquired the user can start with the processing of the data for reconstruction. This will be described in the next chapter.

Chapter 3

OCTOPUS

3.1 Introduction

From the start of this doctoral thesis the need was felt for a good tomography software package. Reconstructing tomographic datasets is a time-consuming and repetitive task, both for the data preparation and the actual reconstruction. Commercially available software was often expensive and, more importantly, not flexible enough for typical experimental conditions. Each research group seemed to have written their own set of routines for reconstruction, but none of those were at the same time efficient, complete and user-friendly. Therefore we decided to develop a software package in LabVIEW that would cover all the necessary routines for performing tomographic research. The large computational demands of tomographic reconstruction inspired us to develop the software in a distributed fashion. A number of client computers, distributed over a network, can jointly reconstruct a given dataset. This eventually lead to the name of the package: OCTOPUS.

Over the years Octopus has grown from merely a script for reconstructing parallel beam data to a full-featured package. Recently Octopus became available as a stand-alone executable (previous versions required the LabVIEW environment). The following section will give an overview of the features of the latest version of Octopus. The section after that will describe the algorithms behind the most relevant functions. Finally the performance of the reconstruction part will be evaluated.

3.2 Features and User Interface

We will start the description of Octopus by giving an overview of the most important steps in a typical tomographic reconstruction of parallel beam data, starting from the original projection data and ending with the reconstructed 3D volume.

3.2.1 Data preparation

Convert data

Octopus works with its own internal file format (with extension .oct). A conversion routine is available to convert the original raw data to the oct-format (or other formats). A number of existing image formats such as tiff, fits, bmp and png can be converted as well as raw binary data. Options include transposing, flipping, resampling, cropping, rotating and spot filtering the images.

Select Files

As a first step the user selects the source data (in oct-format). These are the radiographic projections as recorded by the detection system, and optionally beam profile images and offset images. First the first projection is selected, then the last. The user is then asked if beam profile images were recorded. If so the first and the last ones are indicated. Similarly the program asks if dark images were recorded.

Resize

In many cases only part of the projection is of interest, for example when a sample is much smaller than the field of view that was recorded. To avoid processing unnecessary data the projections can be cropped to a so called Region Of Interest or ROI. Therefore the user is shown an image that is a sum of a number of projections covering the total angular range. This way one can immediately judge through which part of the detector area the sample rotated during the entire measurement. The user then indicates the Region Of Interest by dragging a rectangle or filling in the coordinates.

Spot Filter

An important step towards a good reconstruction is the filtering of spots in the images, both bright and dark spots. These spots can be caused by dead or hot pixels in the CCD (see appendix B) or direct hits by gamma rays. They can introduce strong artefacts in the reconstructions. The user chooses the filter level using a slider control whilst viewing the original image, a resulting filtered image and a differential image. There is also an option to find an appropriate level automatically.

Normalisation

Next the projections have to be normalised. normalisation in space is done by dividing the projections by a recorded beam profile. This requires no user interaction since the location of the beam profile files was indicated in the

first step. The user is asked if normalisation in time is necessary (to correct for changing exposure conditions such as a fluctuating beam intensity). If so, then the user is, as in the ROI selection, presented an image that is a sum over the complete angular range. A region is to be indicated that is never obstructed by the sample. For each projection the resulting mean greylevel of this region will be used as an indicator for the exposure to compensate for beam fluctuations. This is especially important at a spallation source like SINQ that inherently shows beam fluctuations. During the process of normalisation the user is shown the recorded average intensity in the ROI (after normalisation with the beam profile). From this it can be judged whether the beam was stable or not, and if there was significant scattering from the sample to the surroundings.

Build Sinograms

Then the data are rearranged to sinograms. Each sinogram consists of all the projections of a single slice. This step requires no user interaction. Depending on the selected reconstruction method the sinograms are arranged in individual files or a single so called volume file.

Ring Filter Sinograms

If necessary the sinograms can be ring-filtered. Ring artefacts in the reconstructions occur when a pixel shows a systematic deviation from other pixels in all projections. This can have several causes. The two main causes are bad pixels in the CCD chip and deviations introduced by the normalisation due to poor statistics in the beam profile images. The effect is most easily spotted in the sinogram as a straight vertical line. Choosing a filter level is done in the same way as was the case for the spot filter.

3.2.2 Reconstruction

Parallel Beam Reconstruction

When the sinograms are ready one can start preparing the actual reconstruction. A slice can be selected by means of a cursor on a projection that is shown. The user can set a number of parameters and preview the reconstruction of the chosen slice. There is a choice between two algorithms, the slower direct implementation of the filtered backprojection algorithm, and the much faster but slightly less accurate IMAQ10 method which will be described in paragraph 3.3.2. A key parameter is the centre of rotation. When possible this is calculated automatically from the projections at 0° and 180° but it can be manually fine-tuned here. Another parameter is the frequency filtering. It was explained in the theory in section 2.2.1 that the projections have to be filtered. A stronger suppression of high frequencies yields softer

smoother looking reconstructions but accordingly less resolution. The filter level can be chosen by means of a slider. There is also a beam hardening correction (explained further, beam hardening is less important for neutron tomography but very important for X-ray tomography). A handy feature is the offset angle. This is used to rotate the reconstructed slice over a given angle. Finally there is the option to define a Region Of Interest (ROI) to speed up reconstruction time (only in the case of the accurate algorithm).

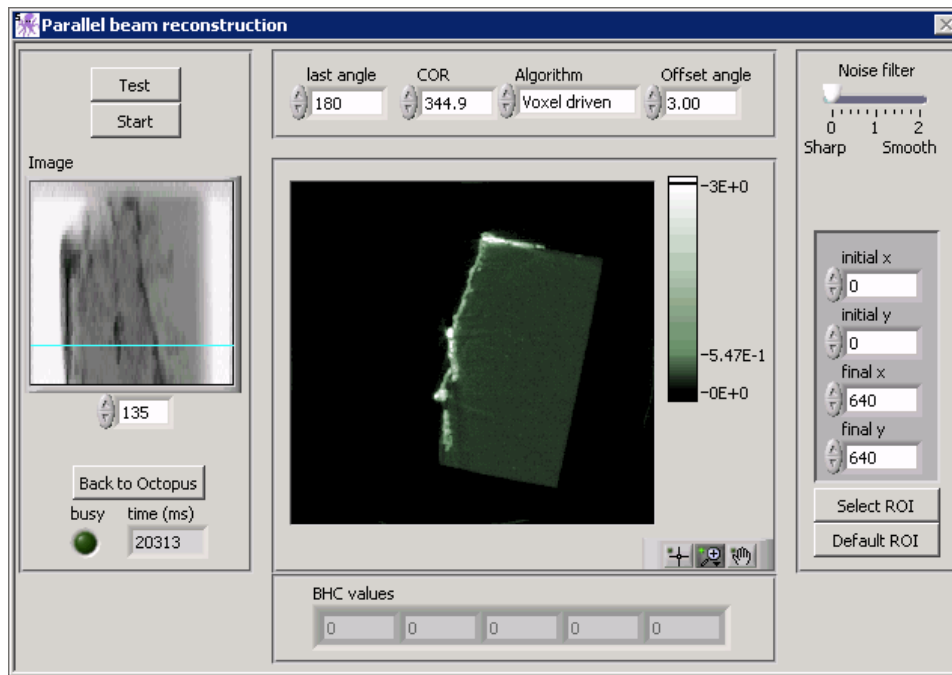


Figure 3.1: The parallel beam reconstruction panel

Cone Beam Reconstruction

The data preparation procedure in the case of cone beam data is exactly the same as described for parallel beam data. The reconstruction however requires a number of extra settings. Most importantly there is the geometry that defines the cone nature of the beam. This is essentially defined by three parameters, the pixel size (defining the size of the detector area), the source object distance (SOD) and the source detector distance (SDD). From these values then follow the magnification and the cone angle. In addition there is the vertical centre, indicating which detector pixel row is located on the central ray of the cone. Depending on the cone angle there are a number of slices at the top and bottom of the volume for which too much data are missing for a good reconstruction. Therefore a recommended range is shown and the user can choose the range to reconstruct. Finally there is the choice

between three quality settings in the cone beam reconstruction mode.

Networked Reconstruction

The ever-increasing resolution in imaging systems poses computational demands that grow faster than the available computer power. Octopus is therefore capable of doing a tomographic reconstruction on multiple computers through a server-client architecture on any Windows-based network. A client program was written that can be installed on any PC in a network. To minimise the size of the client program the choice was made only to do the reconstruction part in parallel, and not the preparation part.

When the reconstruction process is started in TCP/IP mode the network is scanned for available clients and each client is assigned a portion of the data. Each time a client finishes its portion the results are sent back to the serving machine and new data is served to the client, until all data is reconstructed. During reconstruction clients can stop (e.g. when a user needs his PC for other tasks) and new clients can join the cluster. They will be detected and be given data. At the end the main program verifies that all results have been returned. If not, the server program reconstructs the missing file(s) locally.

This distributed reconstruction decreases the absolute time needed for the reconstruction almost proportionally to the number of clients. Small losses are caused by network delays but proved negligibly small. On the server side only one setting is required: the TCP/IP port for communication, which can be chosen freely to avoid any conflicts (port numbers between 49152 and 65535 are not assigned and thus preferred [75]). The client program only needs two settings, the same TCP/IP port number and the server name. Each client should be given an arbitrary but distinct name. A client can listen to multiple servers at the same time.

Output of Results

The reconstructed slices are normally stored in the internal oct format. There is however the option to prepare the output so that it can be viewed immediately in VGStudio, a much used 3D rendering software package. Therefore the pixel values of reconstructed slices are remapped to a 16 bit integer format (greylevels 0 to 65536) based on the maximum value in the complete volume (the minimal value is set to zero since negative attenuation values are meaningless). A parameter file is then generated that will launch VGStudio when double-clicked and present the volume in 3D. Alternatively the same conversion routine used to convert source data to the oct format can be used to export the reconstructed result to most other common file formats such as tiff, png, bmp or jpg. Finally there is also the possibility to write the output to a binary volume file.

3.2.3 Image Viewer

The image viewer is an image analysis program written specifically for tomography research. A screen dump is shown in figure 3.2. It can be called at any time during the data preparation process or even during the reconstruction process to evaluate intermediate results. The following image formats can be read: oct, bmp, tiff (incl. 16 bit), png, fits, jpg, 2pi, neu, bmp, txt and b16. It contains a large number of functions. Basic functions include zooming, cropping, panning, cursors, output to other formats... A number of colour scales can be applied (grayscale, spectrum,...) and a clipping indication can be applied, for example to judge overexposure (the green area in the projection shown in 3.2 is possibly underexposed). The images can be calibrated to real world units, allowing accurate measurements to be made, e.g. on the reconstructions. This can be very useful for quality control or reverse engineering purposes. Other functions include a histogram of the image, statistical analysis (mean, variance...), Region Of Interest, intensity profiles along a line between two points, data output to EXCEL, 3D visualisation, converting stacks to AVI movie... Finally there is an edge fitting routine for accurate resolution measurements.

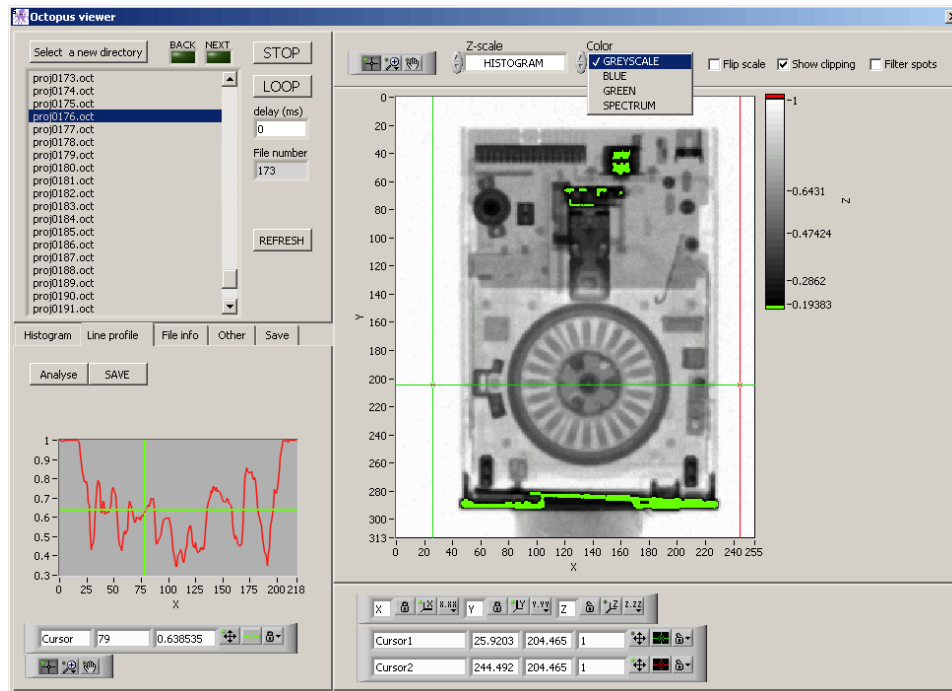


Figure 3.2: The image viewer

3.2.4 Other features

- Auto mode : a fully automatic mode for parallel beam CT that requires only the location of the source data. All processing steps are performed automatically. Where possible optimal parameters are calculated automatically (spot filtering level, COR). Other parameters use default settings. Only normalisation for beam intensity fluctuations is not included since this requires user input that cannot be automatised. The result is a reconstructed 3D volume ready for visualisation with 3D rendering software. There is also the possibility to reconstruct multiple datasets. This proved indispensable in the dynamic tomography experiments that will be described further. During these experiments tens to hundreds of tomographies were recorded per sample. Preparing and reconstructing all those datasets individually and manually would have been impossible.
- Element sensitive mode : Octopus can process dual energy datasets for element sensitive tomography. The element sensitive mode is identical to the normal mode, but the user is asked for two sets of data instead of one. After normalisation the projections at both energies are divided, leaving only a signal where the element under study is present (see [10] for more details). These divided images are rearranged into a single set of sinograms. The resulting reconstruction is a 3D distribution of the investigated element.
- Filtering : a number of kernel based filters is available for smoothing, sharpening and denoising of images.
- Resampling : for resampling single images or complete directories to other dimensions. The interpolation scheme used for this is bilinear interpolation.
- Find skew angle : routine to calculate possible skew in a tomographic data set. Skew is a rotation of the axis of rotation in the plane parallel to the detector. In that case the images should be rotated back so that the axis of rotation is aligned with the vertical direction. Based on the projections at 0° and at 180° this routine calculates the observed centre of rotation for each slice and from this estimates a tilt.
- Rotate images : to rotate images around the centre. When called after calling the 'Find skew angle' routine the resulting tilt angle is passed on automatically to this routine.
- Image arithmetics: for mathematical operations on individual images or complete directories.
- BHC : Beam hardening correction routine
- MAR : Metal artefact reduction routine
- RLD : Richardson-Lucy Deconvolution : iterative sharpening procedure

3.3 Implementation and Algorithms

3.3.1 Data preparation

File Format

Octopus works with its own file format with the appropriate extension .oct. It is a binary file with an ASCII header of 512 bytes with relevant information like the time and date the image was recorded, the dimensions, exposure time. . . The data type can be either unsigned 16 bit integer or 32 bit float. The byte order is little endian. A conversion routine has been implemented to convert other data types to the oct-format. These can be TIFF, FITS, JPG, BMP, PNG and a number of custom formats for current users. RAW binary files can be read too when the properties are known (image dimensions, bits per pixel, header length. . .)

Spot Filter

The importance of a good spot filter was mentioned earlier. It should filter out spots caused by for example direct gamma ray hits in the CCD without blurring the image. For this reason we implemented a thresholded median filter instead of the commonly used median filter acting on all pixels (or even worse, a mean filter). Each pixel value is compared to the mean of its 8 neighbours. Because of the Poisson statistics¹ the uncertainty on a given value is more or less proportional to the square root of this value. If the pixel value deviates more than this square root of the mean times the set level it is considered to be a spot. It is then replaced by the median of its 8 neighbours. The criterion is shown in equation 3.1. The index n indicates that it is a neighbouring pixel. The reason for comparing the pixel value to the mean of the eight neighbours instead of the median is purely calculation time. Finding the median requires sorting the values, which is much slower than finding the mean.

$$I - \frac{\sum_{i=1}^8 I_{i,n}}{8} \leq level \cdot \sqrt{\frac{\sum_{i=1}^8 I_{i,n}}{8}} \quad (3.1)$$

The reason for choosing a thresholded median instead of the much used mean is that most pixels remain unaffected, no blurring occurs and clusters of spots are filtered out better. All this can be seen in figure 3.3². Notice how the mean filter does not remove the spots (bottom left quarter of the image) but merely reduces them and spreads them out.

¹Recording an image is a counting process where individual photons are counted thus resulting in Poisson distributed uncertainties on the recorded values. In the case of the Sensicam CCD camera used in this work 1 greyvalue corresponds to about 5 photons.

²The limited tonal range in print makes it difficult to judge the difference. Please refer to the electronic copy of this document

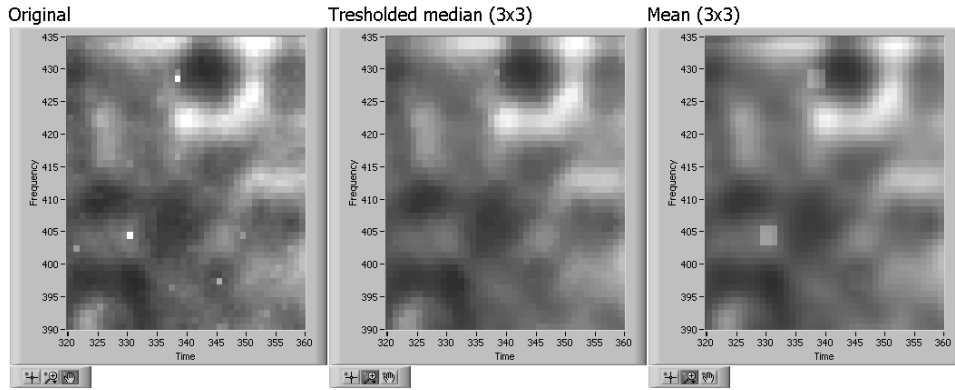


Figure 3.3: From left to right : the original image, the thresholded median result and the mean filter result

Normalisation

Normalisation is a very important step. One has to consider normalisation in the spatial domain and in the time domain. The first is to correct for the inhomogeneities in the recorded beam intensity distribution. It is determined not only by the beam intensity distribution itself, but also by the scintillator response and the imaging system. It is recorded in the so called 'open beam' images (also called 'flat field' or 'beam profile' images). All the projections have to be divided by the resulting distribution. Before this can be done the images have to be spot filtered and corrected for noise contributions like readout noise, ADC offset and dark current noise (see appendix B). The noise is recorded in the so called 'dark' images or 'offset' images. If no dark images were recorded a constant value can be used. The beam profile with which to normalize is calculated by taking the mean of the corrected open beam images, $I_0 - DI$. To reduce ring artefacts (see further) the resulting image can be again spot filtered to a high degree to reduce the influence of statistical noise. The importance of the beam profile images should be noted here. Every single projection will be divided by the same final beam profile image. Any deviation in this image will become a systematic deviation in the complete dataset, showing up mainly as a ring artefact (see further).

The second kind of normalisation is that in the time domain to correct for the beam intensity fluctuations during the acquisition of the projections. If this was selected then the user indicated a Region Of Interest (ROI). This region is supposed to be never obstructed by the sample, thus providing an accurate measurement of the actual exposure of each projection. After normalisation by the beam profile the average value in the ROI, I_{ROI} , which should already be close to one, is calculated for each image. The image is then again divided by the resulting value. Ideally the end result should show

a flat background with a value of exactly one.

This results in the following equation for the normalised image:

$$I_{norm}(x, y) = \frac{I(x, y) - DI(x, y)}{I_0(x, y) - DI(x, y)} \cdot \frac{1}{I_{ROI}} \quad (3.2)$$

$I(x, y)$ stands for the recorded image, $DI(x, y)$ for the dark image, $I_0(x, y) - DI(x, y)$ for the corrected beam profile image and I_{ROI} for the average intensity value in the Region Of Interest. The top row of figure 3.4 shows the beam profile that was calculated from five open beam images and a corrected original projection. The bottom row shows the recorded average intensity of the ROI throughout the entire acquisition and the normalised result. Notice how the spots on the scintillator (on the left) are invisible in the final image. Also notice how the tube on the right which is present in the open beam image is no longer visible in the final image. Only the water inside the tube that shifted slightly between both exposures remains in the final image. The intensity plot reveals that the beam intensity dropped slightly during the first half of the acquisition (about 2,5%) and slightly rose again during the second half.

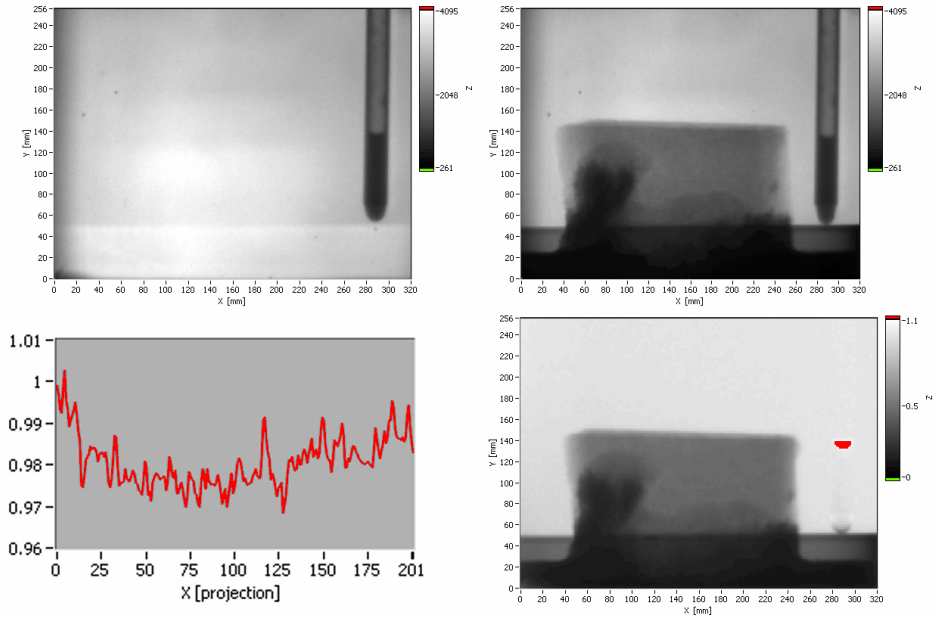


Figure 3.4: Normalisation in the spatial and time domain. The beam profile (top left), a raw projection (top right), the beam intensity plot (bottom left) and the resulting normalised image (bottom right)

Build Sinograms

Building the sinograms is nothing more than rearranging the data into files that each contain information on a single slice. This requires a lot of hard disk I/O operations. Therefore all the files get the file status 'open' before starting and the actual reading is performed using low-level file access routines to achieve the highest possible throughput. No user interaction is required at this point.

Ring Filter Sinograms

White spots caused by gamma rays occur on a random position in a random projection. They cause a straight line when backprojected. There are also spots that are present at the same coordinates in all projections. These are caused by bad pixels in the camera (either dead pixels, stuck pixels or pixels with a different linearity). These are cancelled partially by the normalisation, but sometimes an extra filtering is needed. A much neglected cause of ring artefacts is bad statistics in the beam profile image. A ring artefact is caused by a systematic deviation at a fixed pixel position through all projections. All projections are divided by the same beam profile image. So if a pixel in the beam profile image exhibits a statistical fluctuation it will show up in all the normalized images. It is therefore essential to record a sufficient number of open beam images so that the beam profile can be calculated with high enough statistics. If the main noise contribution is due to photon statistics and the beam profile is relatively uniform than the beam profile image can be smoothed to reduce ring artefacts.

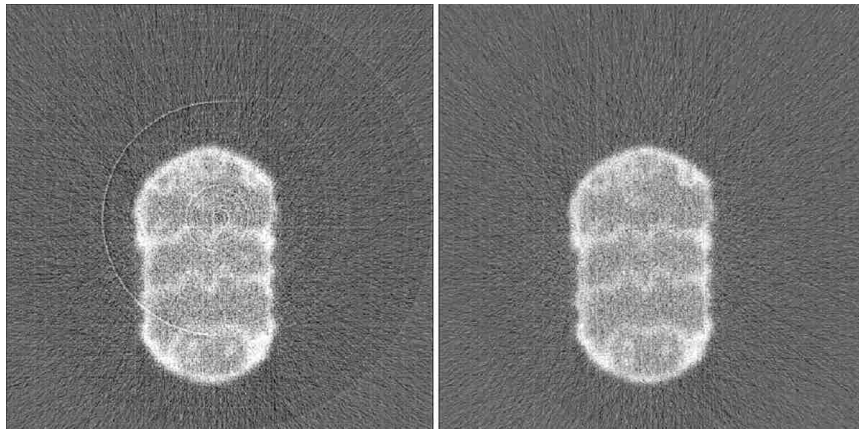


Figure 3.5: Reconstruction without (left) and with (right) ring filter

Ring artefacts can be recognized most easily in the sinograms as vertical lines from top to bottom. Filtering is done in a similar way as the white spot filtering. For each sinogram the average of each column is calculated and

compared to that of its neighbours. When deviating more than a chosen level times the variance on the averages, the pixel values in the column are multiplied by a correction factor so that the average of the column becomes equal to the median of the averages of its neighbours. This performs better than the commonly used method of applying a low pass filter in the perpendicular direction which introduces unnecessary blurring. To filter out rings that are wider than one pixel this procedure is repeated a number of times. Each iteration takes more neighbouring columns into account. Figure 3.5 shows the result of the spot filtering on a reconstructed slice.

3.3.2 Parallel Beam Reconstruction

A lot of the effort in developing Octopus was spent in writing a fast but accurate filtered backprojection algorithm. This paragraph will describe the different types of algorithms that were developed. They are all different implementations and approaches of the same basic filtered backprojection algorithm.

Finding the centre of rotation

One of the discerning features of Octopus is its automatic detection of the centre of rotation. Usually one carefully aligns the sample stage such that the axis of rotation coincides perfectly with the central line of the detector. This can be very cumbersome, especially in frequently changing setups. We implemented a software detection of the centre of rotation, eliminating the need for alignment. The algorithm works as follows: the projections taken at 0° and at 180° are in theory mirror images, mirrored around the wanted axis of rotation. In reality this is not exactly true due to for example scattering effects or beam geometry effects. Nevertheless this seldom proves to be a problem and will be neglected in the following explanation. To speed up calculation the two images are summed along the columns resulting in two 1D profiles. The second profile is reversed. If the centre of rotation coincides exactly with the centre of the image these two profiles will be the same. If not then the second profile will be shifted relative to the first. The second profile is therefore shifted along the first and each time the sum of the square differences is calculated. This results in a curve with a clear minimum. A second degree polynomial is fitted to the datapoints resulting in a sub-pixel resolution estimate for the centre of rotation. The actual accuracy depends largely on the rotational symmetry of the object. If there is little difference between the projections at 0° and at 180° then the estimate will be less accurate. For cylindrical objects it is wise to deliberately place the object off-centre with regard to the axis of rotation to allow a more accurate calculation of the centre of rotation. Figure 3.6 shows the effect of a wrong centre of rotation (left) compared to a correct setting (right). It gives rise

to clear arc-shaped artefacts with a radius that is equal to the error on the centre of rotation that was chosen.



Figure 3.6: The effect of a wrong centre of rotation on the reconstruction

The classical filtered backprojection

The goal of tomography is to reconstruct a 3D distribution of a certain physical quantity from a set of 2D projections acquired from different angles. Figure 3.7 recalls the coordinate system as it was introduced in Chapter 2. Considering one horizontal 2D slice through the 3D volume one can see that this corresponds to a set of 1D lines in the projection data. Ordering these lines into an image yields a so-called sinogram, giving a view through the slice from all angles. All the information needed to reconstruct the slice is contained in this sinogram.

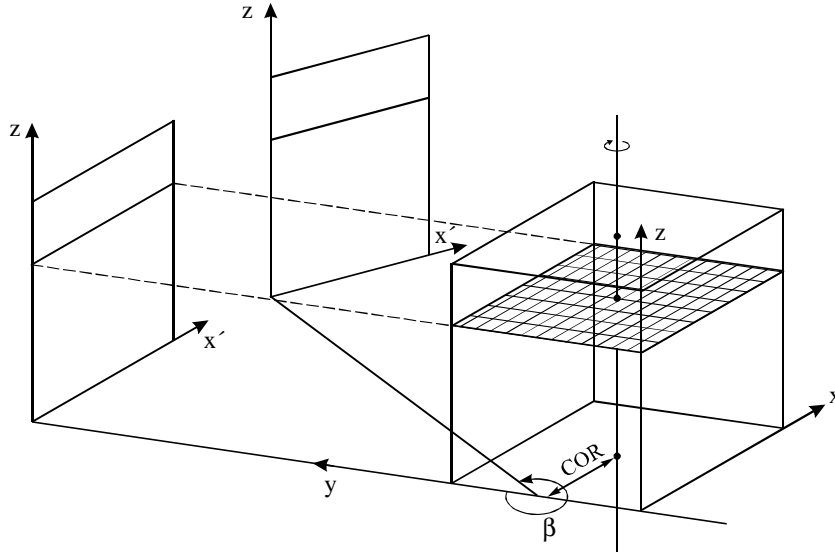


Figure 3.7: The coordinate system for parallel beam geometry.

Reconstructing the slice is conceptually done by backprojecting each line from the sinogram onto an initially empty grid under its proper angle and adding those images together. In the actual implementation one often goes

the other way round. For each pixel (x,y) in the slice one samples the contributions to this pixel, for each angle, by projecting it onto the corresponding line in the sinogram. This describes a sinusoid in the sinogram, hence the name. Adding these contributions together then gives the reconstructed value of that pixel. Such an approach is called 'voxel driven' reconstruction.

It was explained in the theory that the sinogram has to be deconvolved with an appropriate filter before backprojecting. This is to account for the fact that the impulse response of the backprojection operator is not a Dirac impulse. A deconvolution in real space corresponds to a multiplication in Fourier-space and is therefore implemented as such. The sinogram is read line per line. Each line is padded on both sides with zeroes to a width equal to the nearest power of 2, so that the Fast Fourier Transform algorithm can be used which executes faster than a general Fourier Transform. The result is then multiplied with the filter coefficients also given in frequency space as formulated in 2.2.1. The result is then transformed back to spatial coordinates using the Inverse Fourier Transform.

Now the actual reconstruction can be described. From this point on we will refer to 'the filtered sinogram' as 'the sinogram'. Consider each slice to be $N \times N$ pixels, the number of projections is P , α is the angular increment between successive projections, therefore $\alpha = 180/P$, and β is the angle of projection. COR stands for centre of rotation of the sample. Let us call the reconstructed slice $R(x,y)$ and the sinogram $S(x,\beta)$. The projection of pixel $R(x,y)$ under an angle β has an x' coordinate in the sinogram given by equation 2.1. Let us recall it here:

$$x' = COR + (x - COR) \cos\beta + (y - COR) \sin\beta \quad (3.3)$$

Then the value of pixel $R(x,y)$ is found by summing the contributions for all the different angles:

In pseudocode:

```

for x=1 to N
  for y=1 to N
    for  $\beta=0$  to  $180-\alpha$  step  $\alpha$ 
       $R(x,y) = R(x,y) + S([COR+(x-COR)\cos\beta + (y-COR)\sin\beta],\beta)$ 
    end for  $\beta$ 
  end for y
end for x

```

This is the classical way of implementing the Filtered Backprojection algorithm and we therefore named it the Hard Way (HW). As a test a sinogram of 512 pixels wide and 200 projections was reconstructed, resulting in a 512x512 pixel image. It took a Pentium4 1.7 GHz with 1GB RIMM using LabVIEW version 7.1 about 4.8 seconds. This includes the filtering of the sinogram and file I/O operations. All further timing results refer to this

same configuration. This straightforward implementation was also written in C-code and embedded in the LabVIEW environment (HWc). This algorithm takes about 3 seconds. It should be stated that reconstruction times can depend a lot on the architecture of the CPU used, the software environment and, in case of C-based implementations, on the compilers that are used. Timing results are to be taken as a rough indication only.

A more intuitive approach : The IMAQ method

In an attempt to reduce the reconstruction times needed we approached the problem from another angle. Intuitively the backprojection can be broken down into two steps: the actual backprojection along a fixed main axis, which is nothing more than repeating the line N times, and then rotating the resulting $N \times N$ image to the right angle. This image is then added to the intermediate result. The computational complexity lies in the rotation of the image. This approach was implemented using the code libraries that come with LabVIEW's image processing toolkit IMAQ. We therefore named our implementation the IMAQ method.

In pseudocode:

```

for  $\beta=0$  to  $180-\alpha$  step  $\alpha$ 
  for  $i=1$  to  $N$ 
    backprojection( $x,i$ )= $S(x,\beta)$  - repeating the line  $N$  times -
  end for  $i$ 
  rotate backprojection over  $\beta$ 
  add backprojection to intermediate image
end for  $\beta$ 

```

This first implementation was called IMAQ180 and proved to be about 20% faster than the classical implementation, taking 4,2 seconds to complete. This approach allows for considerable optimization. When the number of projections from 0 to $180-\alpha$ (α being the angular step-size) is even, the projections can be divided into two orthogonal sets going from 0 to $90-\alpha$ and from 90 to $180-\alpha$ degrees. Presented here is a method to calculate much faster the contribution of two orthogonal projections to the intermediate result. Consider the projections at β and $\beta+90$. In the previous implementation these were both backprojected, rotated over β and $\beta+90$, and then both added to the intermediate result. But the following implementation precalculates the result of backprojecting the first, backprojecting the second and rotating it 90 degrees, and summing both. This leaves only one rotation over β to be done, and one addition to the intermediate result. This makes a big difference since it is especially cosine and sine functions that execute slowly on a CPU.

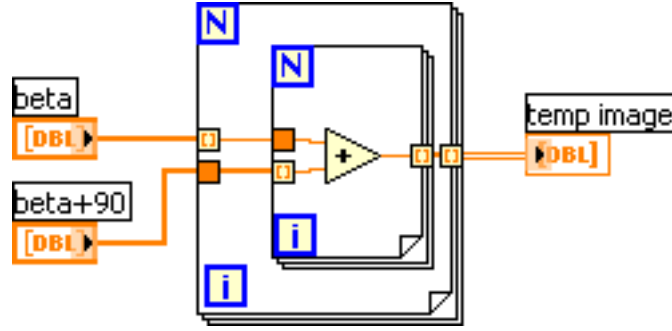
In pseudocode:

```

for  $\beta=0$  to  $90-\alpha$  step  $\alpha$ 
  for i=1 to N
    for j=1 to N
      backprojection(i,j)=S(i, $\beta$ )+S(j, $\beta+90$ )
    end for j
  end for i
  rotate backprojection over  $\beta$ 
  add rotated backprojection to intermediate image
end for  $\beta$ 

```

Or more elegantly in Labview (only the inner two loops):



This implementation was called IMAQ90 and is now about 80% faster than the classical HW algorithm, taking just 2.7 seconds to complete one slice. The condition that the number of projections has to be even is hardly a constraint since this is mostly the case anyway.

A different approach : The STRETCH method

In a third and final approach we tried to calculate the rotated images in an entirely different way. Consider again equation 3.3. As stated before this gives the x-coordinate of the projection of pixel S(x,y) under an angle β onto the sinogram. Now consider transforming each line in the sinogram by stretching it by a factor $1/\cos(\beta)$. Then the coordinates in the newly prepared sinogram become:

$$x' = \frac{COR}{\cos\beta} + x - COR + (y - COR) \frac{\sin\beta}{\cos\beta} \quad (3.4)$$

This operation actually implies oversampling the line and therefore interpolation between the existing values is needed. Simple linear interpolation proved to be sufficient. From this expression it follows that:

$$x' = \frac{COR}{\cos\beta}(1 - \sin\beta - \cos\beta) + y\tan\beta + x \quad (3.5)$$

$$x' = C + y \tan \beta + x \quad (3.6)$$

C is a constant combining all terms independent of x and y . Now consider the first line of the slice to be reconstructed, this means $y=0$. Then 3.6 becomes:

$$x' = C + x \quad (3.7)$$

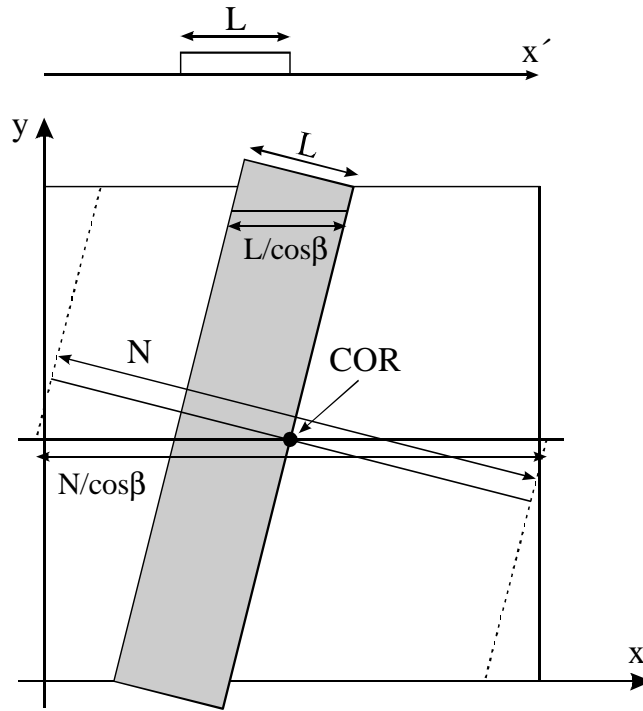


Figure 3.8: Building the rotated backprojection

So the first line of pixels is simply a subset of the stretched line, starting at position C , and N pixels long. For each subsequent line y increases by 1 and the starting position shifts by $\tan \beta$. This means that the rotated backprojected image can be built by repeatedly taking an N pixel long subsection from the stretched projections, starting at a position only dependent on y (the coordinate of the line) and β . Because the starting position can be less than zero or the end position larger than $N/\cos \beta$ the stretched line must be padded with zeroes. Looking at the top of figure 3.8 we see one line from the unprocessed sinogram taken at an angle β with a shadow of L pixels long, the right side of it being exactly on the centre of rotation. Also shown

is the slice with the backprojection of this line under the angle β . Bear in mind that the backprojected image is built in horizontal lines, crossing the shadow under an angle β . This explains the stretching factor of $1/\cos\beta$. The dashed lines show the edges of the projection. The regions outside of these have to be padded with zeroes. It can be shown that on both sides of the stretched line a length of $N \cdot (1 + \tan(\beta) - 1/\cos(\beta))/2$ zeroes has to be padded. Now the rotated image is easily built from this prepared line. There is a complication though. Stretching the projection by a factor $1/\cos(\beta)$ is fine as long as β is relatively small, but for angles approaching 90 degrees the factor $1/\cos(\beta)$ goes to infinity. This can be avoided by building the image in the orthogonal direction, along y instead of x . Therefore the sinogram is subdivided in four intervals of 45 degrees. The lines are stretched with the following factors:

$$\begin{array}{lll} 1/\cos\beta & \text{for } 0 & \leq \beta < 45 \\ 1/\cos(90-\beta) & \text{for } 45 & \leq \beta < 90 \\ 1/\cos(\beta-90) & \text{for } 90 & \leq \beta < 135 \\ 1/\cos(180-\beta) & \text{for } 135 & \leq \beta < 180 \end{array}$$

This way no projection is stretched by more than a factor $\sqrt{2}$ keeping the number of interpolations to be done reasonable. The modified sinogram now looks like Figure 3.9. It can be shown that with a few simple symmetry operators like reversing and transposing, any rotation between 0 and $180-\alpha$ can now be constructed. In the second and third range x and y are reversed, this implies that afterwards a transpose function will have to be performed before adding them to the intermediate result. In the last range it can be seen that the sign before the x is negative, meaning that the line has to be reversed before building the rotated image. Similar routines are used for the remaining ranges. This implementation proved to be more than two times faster than the classical FBP algorithm, taking just 2.3 seconds.

The final result : The IMAQ10 method

We implemented and tested many variations and combinations of the methods described above. The final outcome of this was the IMAQ10 method. It combines the IMAQ method with part of the stretch method to come empirically to an optimal performance. The basic idea is to use the STRETCH method to perform rotations over small angles and to use the IMAQ method for rotations over larger angles. The sinogram is therefore subdivided in a number of strips, each containing typically 20 projections. Each strip is again subdivided in two subsets, one containing the projections with even indices and one containing those with odd indices. We define a main angle as the angle that corresponds to the first projection of each subset (each strip containing two subsets). Now consider a single subset. For each projection

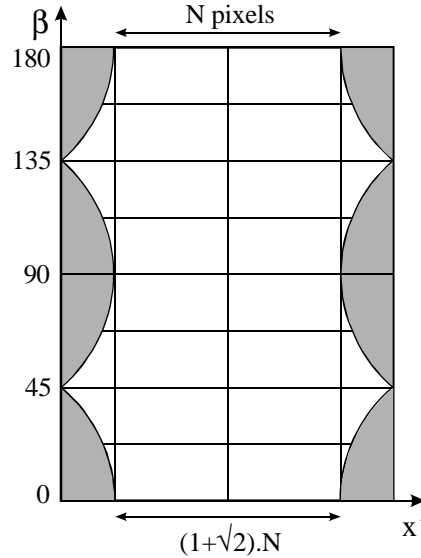


Figure 3.9: The stretched sinogram (the grey areas contain no data)

an intermediate contribution is calculated using the STRETCH method using the angular difference between the projection under consideration and the main angle of this subset. After summing all the intermediate contributions for a single subset there remains a rotation to be performed over the main angle. This rotation is performed using the IMAQ method. The reason for splitting each subset in an even part and an odd part is due to rounding errors in the STRETCH method. For the smallest angles the rounding errors increase rapidly. By splitting each subset the angular difference is doubled, largely eliminating the rounding errors. This implementation reconstructs one slice in exactly 1 second. The results are bundled in the second column of table 3.1.

| Algorithm | Time (s) 256x256x200 | Time (s) 512x512x200 | Time (s) 512x512x400 |
|--------------|----------------------|----------------------|----------------------|
| Hard Way | 1.3 | 4.8 | 9.6 |
| Hard Way (C) | 0.8 | 3.0 | 6.0 |
| IMAQ180 | 1.1 | 4.2 | 8.4 |
| IMAQ90 | 0.7 | 2.7 | 5.4 |
| STRETCH | 0.6 | 2.3 | 4.6 |
| IMAQ10 | 0.3 | 1.0 | 2.0 |

Table 3.1: Comparison of the timing performance of the different algorithms

Also included in this table are the results for two other data sets, one of 200 projections of 256 pixels wide (first column), and another of 400 projections of 512 pixels wide (last column). From this we can deduce

that calculation times scale linearly with the number of projections and to the number of pixels in the slice (which is the square of the width of the projection). This statement holds as long as the data fits into the RAM memory of the reconstructing PC.

Reconstruction Quality

To assess the quality of the reconstructions we used the classical Shepp-Logan head phantom as described in [34], consisting of a number of homogeneous ellipsoids. The corresponding sinogram was calculated and reconstructed with all methods. Eventually only two methods were integrated into Octopus, the C-based classical implementation (called HWc, which stands for the hard way in C) and the IMAQ10 method. The theoretical slice is shown (top left) in figure 3.10. Both methods give very similar results and very little information can be deduced from them in printed form. Therefore only one resulting reconstruction is shown (the IMAQ result, top right). More information can be deduced from the difference images between the reconstructions of both methods and the theoretical image (classical method bottom left, IMAQ10 bottom right). The sharpness was evaluated by making line profiles of an edge and differentiating them. Differences here were very small, the HWc method being slightly sharper but accordingly also containing more noise.

For each homogeneous region in the reconstruction the Signal to Noise Ratio (SNR) was evaluated. When we take the SNR of the classical implementation as 1 we find that the IMAQ method has a SNR of 1.11 or only 11% higher than the HWc implementation. Visual inspection showed only minor differences in reconstruction quality. So we conclude that in most cases the IMAQ10 method is the best option. In particular cases where the sample is much smaller in one dimension than in the other the HWc method is suited better because it can reconstruct a selected region of interest whereas the IMAQ method is restricted to a circular region.

3.3.3 Fan and Cone Beam Reconstruction

The implementation of the cone beam algorithm was performed mainly by J. Vlassenbroeck and will not be described here. The algorithm is a variation on the true FDK (Feldkamp-Davis-Kress) cone beam algorithm [37] that performs the backprojection in a polar coordinate system instead of a rectangular coordinate system. The resulting reconstruction is then remapped to a rectangular coordinate system. This implementation is based on the works of H. Turbell [76] and N. Sorokin [77].

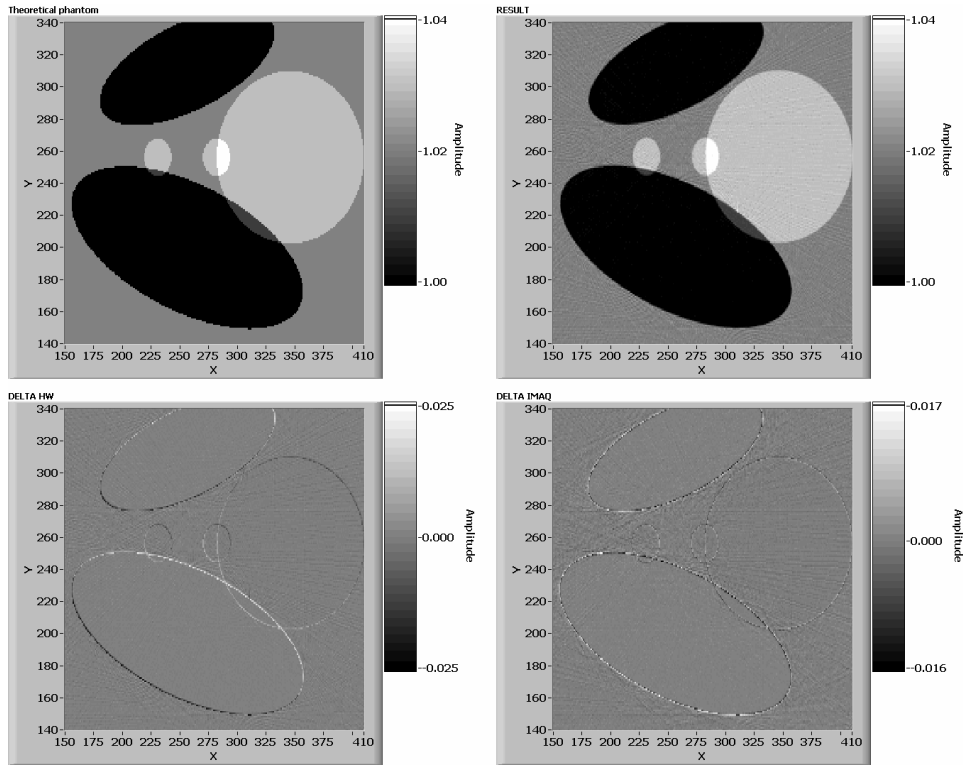


Figure 3.10: The theoretical phantom (top left), the resulting reconstruction (top right) and the difference images for the HW (bottom left) and the IMAQ method (bottom right)

3.3.4 Networking

The distributed reconstruction is based on a self-written TCP/IP based protocol for the handshaking and further communication of settings and file locations. The actual transfer of the data, i.e. the sinogram data from the server to the client and the reconstructed data from the client to the server, is based on the native Windows file access routines. When a client program is launched it is assigned a list of possible servers by the user. When a client program is running it continuously polls its list of servers for an available TCP/IP connection at a given TCP/IP port number. When successful it is registered at that server and it receives a binary string that contains all the necessary parameters and settings such as the reconstruction mode (parallel or cone), the network location of the sinograms, the destination of the reconstructions, the centre of rotation, filter level... In the distributed reconstruction mode the sinograms are not stored as individual files but as a single so called 'volume file' on a network drive (this drive is automatically shared by the main program so that it is accessible through the local network). This choice was made because it results in much higher performance

than using individual files.

Once the reconstruction settings are received the client reads the appropriate portion of sinogram data from the volume file on the network drive. Then the client starts reconstructing one or more slices and saves the result at the right location. The reconstructed slices are saved as individual files. If there remains data to be reconstructed the client again receives a binary string, reads the corresponding sinogram data and reconstructs it. This process is repeated until all slices are reconstructed. At any time a client can leave the reconstruction cluster. In that case the ongoing reconstruction will be completed and the client sends a disconnect command to the server. The client is then removed from the cluster and the client program is closed.

3.4 Performance

3.4.1 Timing different processing steps

Data preparation

To evaluate the performance of the data preparation steps we use a typical dataset of 200 projections of 512x512 pixels stored as 16 bit integers, resulting in about 100 MB of data. Table 3.2 gives an overview of the time needed for the different preprocessing steps. Notice that for the first steps there are 208 images, 200 projections, 5 beam profile images and 3 dark current images. It should be taken into account that these results are only indicative, since they depend on a number of factors such as the fragmentation state of the hard disk and other processes running on the PC.

| process | time per image (ms) | # images | total time (s) | fraction file I/O |
|-------------|---------------------|----------|----------------|-------------------|
| crop | 111 | 208 | 23 | 0.65 |
| spot filter | 207 | 208 | 43 | 0.35 |
| normalise | 130 | 200 | 26 | 0.58 |
| sinograms | 29 | 512 | 15 | 1.00 |
| ring filter | 35 | 512 | 18 | 0.83 |

Table 3.2: Time needed for the different preparation steps

From this table we can draw the following conclusions:

- all data preparation steps roughly take the same time to execute
- a large fraction of the time to execute is spent in file I/O
- these times are too short to benefit from a distributed approach
- in total data preparation takes about 5 to 10 minutes, including user interaction
- for larger datasets data preparation takes much less time than the actual reconstruction

Parallel Beam Reconstruction

The reconstruction algorithms were already discussed in 3.3.2. Reconstructing the complete 512x512x512 pixel volume based on 200 projections takes 1860 seconds or 31 minutes using the classic method and a Pentium4 1.7 GHz with 1GB RIMM using LabVIEW version 7.1. Using the IMAQ10 method requires 490 seconds or just over 8 minutes. The current implementations are optimized as much as possible. Future improvements will require other approaches. One approach is embedding C-based routines, although only limited improvements are to be expected based on previous tests. A second approach will be based on fundamentally different algorithms that reduce the computational complexity from $O(N^3)$ to $N^2 \log(N)$. There exist a number of such algorithms [78, 79, 80] and we intend to evaluate which one is suited best for implementation and integration into the existing software.

Cone Beam Reconstruction

Only one algorithm was implemented for cone beam reconstruction, but with three quality settings. The dataset used for this measurement consisted of 413 projections of 1024x1024 pixels. Reconstruction was done using the default 'normal quality' setting. Because of the nature and complexity of the cone beam algorithm reconstruction times per slices are not constant but depend on the position of the slice to reconstruct and the cone parameters. The timing results presented here are therefore to be considered solely as a rough indication. Reconstruction of this dataset on the above mentioned PC takes 185 minutes or just over three hours.

3.4.2 Networking

To assess the performance of the server client architecture we installed the client program on twelve PC's in our office building. These are all regular PC's running Windows XP and connected through 100 Mbit Ethernet. The server is a workstation with a dual Intel Xeon 3.06 GHz processor and 4 GB of RAM. The dataset used for this measurement consisted of 413 projections of 1024x1024 pixels, reconstructed in cone beam geometry using the normal quality setting. For each client (their names are listed in column 1) we recorded the time for reconstruction of each slice (column 2) and from this we calculated the number of slices it could reconstruct per second (column 1). Ideally the total reconstruction speed should be the sum of the individual performances. The overhead of the communication protocol, queuing at the server side, network delays etc. causes some loss in reconstruction speed.

The measurements are summarized in figure 3.11. Because the measurements are done using a cone beam data set the time per slice depends on the progress of the reconstruction. The slices at the top and bottom of the volume require more sinograms to be reconstructed and thus more time.

| computer | seconds/slice | slices/seconde |
|--------------|---------------|----------------|
| dquark | 11.80 | 0.08 |
| neutron | 11.30 | 0.09 |
| bquark | 7.70 | 0.13 |
| electron | 7.00 | 0.14 |
| photon | 7.00 | 0.14 |
| tquark | 6.80 | 0.15 |
| inwbert1 | 5.30 | 0.19 |
| graviton (1) | 4.80 | 0.21 |
| squark | 4.40 | 0.23 |
| graviton(2) | 4.40 | 0.23 |
| gluon | 4.30 | 0.23 |
| cquark | 4.30 | 0.23 |
| cluster | 2.05 | 0.48719674 |

Figure 3.11: Measuring the performance of the server-client architecture. Notice that the client named graviton is listed twice since this is a dual processor computer running two client programs in parallel

Similarly the slices at the centre require the least number of sinograms, and thus the least time. The values listed in table 3.11 are averaged values over the entire reconstruction. From these data we could calculate that, ideally, the cluster should be able to reconstruct 2,05 slices per second on average. At the server we measured a reconstruction speed of 0,53 milliseconds per slice or 1,89 slices per second. This means that the network losses are of the order of 8%. These losses can be reduced by running the software on a dedicated reconstruction cluster, by using a Gigabit connection, by using a high throughput hard disk array and finally by reducing the number of requests at the server side. The latter can be accomplished by the 'number of slice' setting on the client panel. This setting tells the client the number of slices to retrieve from the server at each request. This way the connection load at the server is reduced. The total time required for reconstructing the 1024x1024x1024 volume is less than 9 minutes. The total time from raw data to 3D rendered visualisation takes less than 30 minutes.

3.5 Conclusion

Octopus has evolved into a complete tool for tomography research. It now has all the necessary routines for preprocessing, reconstruction and post-processing of the recorded data. It supports most common scanning geometries namely parallel, fan and cone. Its server-client architecture makes it possible to reconstruct extremely large datasets within acceptable time-limits enabling users to use the full capabilities of their imaging systems. Octopus proved to be indispensable during the numerous experiments done

during this thesis. Especially the automatic mode saved hours of manual effort. Development on Octopus will continue on all domains. More functionality will be added, new beam geometries will be supported and the overall performance will be further improved.

Chapter 4

EXPERIMENTS

4.1 Introduction

This chapter will describe the scientific experiments, the main part of the work done for this thesis. It will give an extensive overview of the work done on neutron radiography and tomography. Most of the experiments were performed with cold neutron beams at the SING spallation source at the Paul Scherrer Institut (PSI) in Villigen (Switzerland). The first experiments took place at the PGA beamline and were mainly aimed at becoming familiar with the technique of neutron tomography. The setup was thoroughly characterized and the possibilities and limitations of the technique were explored. As explained in the introduction we focussed our attention on three basic domains. First the spatial resolution was addressed. For this a number of thinner scintillators were tested and the influence of neutron collimators was evaluated. A similar experiment was repeated under different conditions at a second beamline at PSI called NCR. Back at the PGA beamline an experiment was set up using a neutron lens. Subsequently we performed two series of experiments aimed at exploiting the energy information of the neutrons. The first experiment was based on a velocity selector, a device to extract monochromatic neutron beams from a polychromatic incoming beam. The aim was to explore the added value of energy tuneable neutron beams in radiography and tomography. The second was based on a technique called topography with the intention to visualise the orientation of crystal planes inside (poly)crystalline samples. This is achieved by combining the spatial information from our imaging system with the angular information from diffraction of a neutron beam in the sample. Finally the time domain was addressed. Therefore a series of experiments was undertaken at the high flux research reactor at ILL in Grenoble. The aim was to perform the first ever neutron tomographies of dynamic phenomena.

4.2 Cold Neutron Tomography at PGA

4.2.1 The SING spallation source

The main part of the research on neutron tomography was done in collaboration with Prof. J. Jolie at the University of Fribourg, Switzerland. His research group operated a beamline for Prompt Gamma Activation analysis (PGA) at the SING facility at the Paul Scherrer Institut (PSI) in Villigen, Switzerland. PSI is a centre for multidisciplinary research in fields such as life-sciences, materials, energy and environment, elementary particles,... The main components of the scientific infrastructure at PSI are a circular proton accelerator, the SING spallation neutron source that is driven by the proton accelerator, and the new SLS synchrotron. The proton accelerator provides up to 2 mA proton beam current with an energy of 590 MeV, or more than 1 MW of beam power, making this the most powerful proton beam in the world. The proton accelerator actually consists of a cascade of three accelerators. First a Cockroft-Walton accelerates the protons up to about 870 keV. After injection in the injector-cyclotron they are further accelerated to 72 MeV. Then the protons are injected into the main cyclotron to be accelerated to the final energy of 590 MeV. The extracted beam passes through two pion production targets, reducing the beam energy to 570 MeV. About 1.2 mA of this beam is guided to the target of the neutron spallation source SING.

The SING target consists essentially of a number of lead bars, enclosed in steel tubes and cooled with heavy water. Protons hitting the lead nuclei bring them in a highly excited state. The excess energy is given off by 'evaporating' mainly neutrons. A 570 MeV proton creates on average 10 of these so called spallation neutrons. In total about $3 \text{ to } 6 \cdot 10^{16}$ high energy neutrons are created per second, in a continuous regime, making SING one of the most intense neutron sources in the world. These fast neutrons (>10 MeV) are then thermalised in a 2 meter diameter cylindrical tank filled with heavy water (D_2O). A small portion of these thermal neutrons are cooled further down in a 20 litre tank filled with liquid deuterium (D_2) at a temperature of 25 Kelvin situated close to the target. All our experiments performed at PSI made use of cold neutrons. Most experimental work was done at the PGA beamline.

4.2.2 The PGA beamline

PGA stands for Prompt Gamma Activation, the main experiment at this position. The PGA beamline is situated at the end of the 64 m long neutron guide 1RNR12. The 23 meters closest to the reactor core are bent with a radius of 3612 m. The remaining 41 m are straight. The first 54 m are

supermirror coated¹ while the last 10 meters are coated with normal Ni. This leads to a characteristic cut-off wavelength of approximately 1.0 Å. The energy spectrum is a close fit to a Maxwellian distribution with a mean wavelength of 5.5 Å, spreading from about 1.8 to 10 Å. This corresponds to an energy range from 25 to 1 meV. The beam is 20 mm wide and 50 mm high and the total flux is 1.2×10^8 n/s/cm² for a typical proton current on the spallation target of 1.2 mA. The proton current is monitored continuously as a measure for the neutron flux. The gamma contamination is very low thanks to the curvature of the guide. As explained in the previous section this is favourable because the used neutron scintillators are also sensitive to gamma rays.

The PGA bunker is 3 by 4 meters wide and built with heavy concrete. The PGA experimental setup is placed on wheels to allow an easy switch to the tomography setup. A steel frame is bolted on well aligned fixation points in the floor. The camera box and the motors are placed on this frame and can be moved along the beam axis. Opposite to the beam entry, on the back wall, a lithium slab is placed as a beamstop. ⁶Li has a high absorption and low scattering cross-section thus minimising activation of the inside of the bunker.

4.2.3 Beam characteristics

One of the first tasks to be performed when doing tomographic experiments of this kind is a good characterisation of the beam parameters. As explained in Chapter 2 this is essential to obtain a good reconstruction. The spatial distribution of the beam intensity was measured first. The useful beam cross section was 20 mm wide and 50 mm high. The camera and lens were set up in such a way that the field of view covered an area on the scintillator of about 22 mm by 28 mm. As a result 1 pixel on the CCD corresponded to an area of $22,3 \mu\text{m}^2$ on the scintillator. The recorded distribution was flat within 10%. To verify the reproducibility of this result multiple exposures were taken under identical circumstances. In vertical direction the beam profile proved to be very flat. In the horizontal direction there was a clear drop to the right side. This is visible in figure 4.1 which shows a lineprofile² taken horizontally through the centre. This asymmetry is due to the curvature of the neutron guide. In general terms this is a beam profile of relatively high quality for tomographic purposes. The standard 420 μm scintillator resulted in exposure times of the order of 7 seconds. It was verified that

¹As a result of their wave-like nature neutrons have a critical angle for total reflection at a surface. Supermirrors are layered structures that exploit the wave properties of the neutron to increase the critical angle by a factor of two. The result is a higher flux, a spectrum reaching into the thermal range but, as a downside, also a higher divergence.

²A lineprofile is a plot of the intensity or greyvalues of an image along a certain line through the image

the scintillator response was perfectly linear with exposure time and that the scintillator inhomogeneity was negligible compared to the beam profile fluctuations.

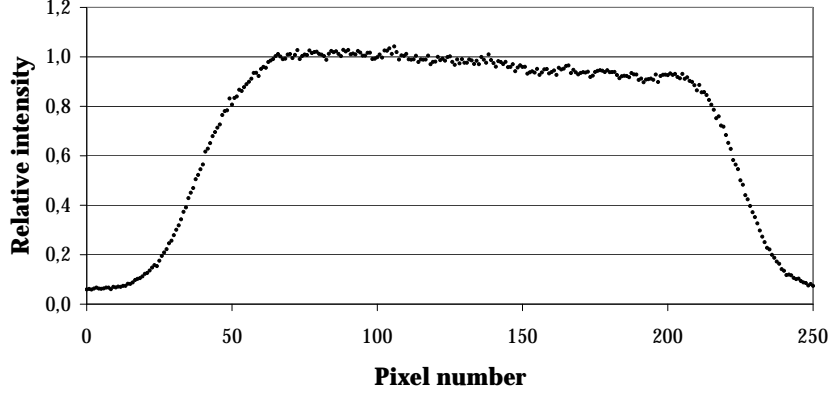


Figure 4.1: PGA beam intensity profile taken horizontally through the centre

The next important parameter to be studied is the spatial resolution. This is determined by two contributions. On one side there is the imaging system (scintillator, lenses, camera,...) and on the other side the combination of source divergence and geometry of the setup. A commonly used method to determine the resolution is the sharp knife edge method. This method has the advantage of allowing these two contributions to be separated. This can be deduced from figure 4.2 showing a strongly absorbing object being projected on the detector at a distance d by a beam with a divergence of α . The always present intrinsic resolution R_{intr} is increased due to the extra spreading R_{geom} caused by the divergence. This contribution is proportional to the distance to the detector screen, so the total resolution R_{tot} can be written as:

$$R_{tot} = \sqrt{R_{intr}^2 + R_{geom}^2} = \sqrt{R_{intr}^2 + (d \times \alpha)^2} \quad (4.1)$$

The divergence of a beam is generally expressed as a ratio of the length of the collimator L and its diameter D , resulting in the so called L/D value. From this it follows that L/D and the divergence angle α are related as :

$$1/\tan(\alpha) = L/D \quad (4.2)$$

In the case of a neutron guide there is no collimator with length L and diameter D defining the divergence but only the critical angle inside the guide. The L/D value is however also used for neutron guides for easy comparison between different kinds of beams.

First the intrinsic resolution of the imaging system was determined. This is the combination of the scintillator, the mirror, the lens and the CCD

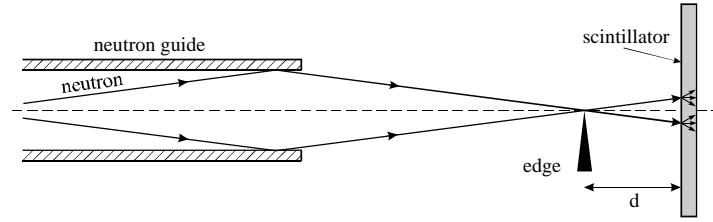


Figure 4.2: The knife edge method for measuring the beam divergence

camera. For this measurement a $25\ \mu\text{m}$ thick Gadolinium foil was placed directly against the scintillator. This yielded a strong enough beam attenuation while the foil thickness was negligible compared to the resolution to measure. By taking a line profile perpendicular to the absorbing edge we obtain the so called Edge Spread Function (ESF). Actually, one line profile yields insufficient statistics, so several line profiles along the edge have to be summed. The measured ESF is shown in figure 4.3. The derivative of the ESF gives the Line Spread Function (LSF). This typically has a Gaussian-like shape. Figure 4.4 shows the measured LSF and the best Gaussian fit to the data.

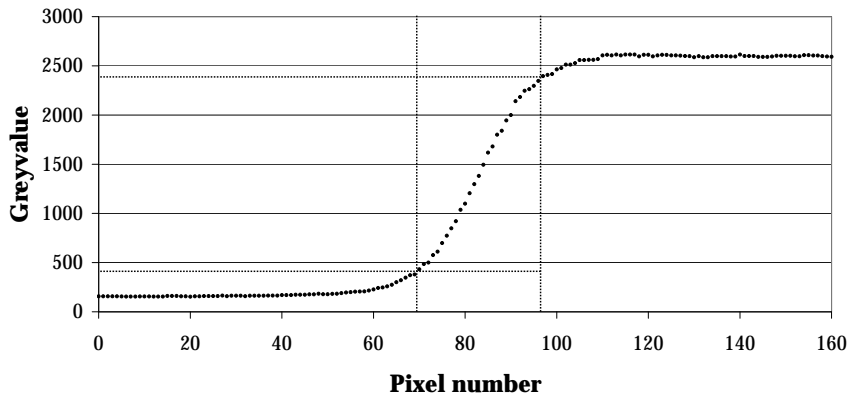


Figure 4.3: The measured Edge Spread Function (ESF)

At this point it should be pointed out that there is no single definition for resolution, nor does it characterise the complete imaging system. Resolution is often stated without properly explaining the way it is defined. Commonly used is the Full Width at Half Maximum (FWHM) of the LSF. Defined as such we obtained an intrinsic resolution of $322\ \mu\text{m}$. We will however use another definition for resolution, namely the distance over which the edge spread function rises from 10% to 90% (see figure 4.3). Using this method we get an intrinsic resolution of about $540 \pm 20\ \mu\text{m}$. This is almost 2 times

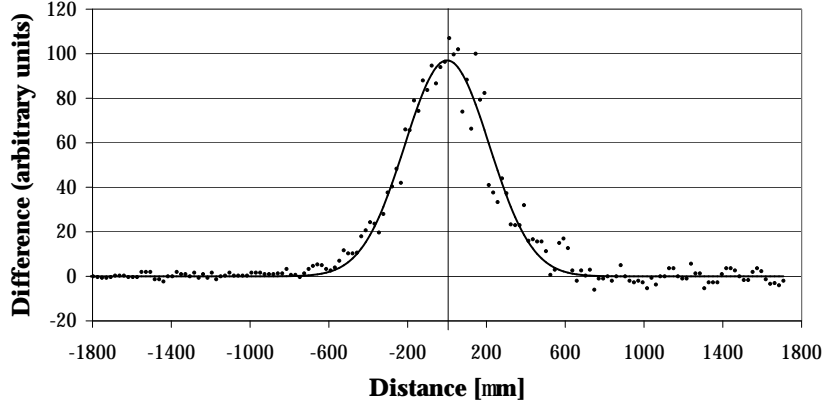


Figure 4.4: The resulting Line Spread Function (LSF)

more than the FWHM, so this should be carefully considered when comparing resolution statements. The main advantage of the 10% to 90% method is the fact that all common edge responses have similar shapes, resulting in similar resolutions. Their corresponding line spread functions however vary from Lorentzian to Gaussian shapes resulting in larger differences. In addition, a commonly used concept in this context is the Modulation Transfer Function (MTF). This is the 1D Fourier Transform of the LSF and gives an indication of the contrast obtained after imaging a sine pattern as function of its spatial frequency, usually expressed in linepairs per millimeter. An imaging system with a 10%-90% rise over a distance x has a limiting resolution (10% contrast) of approximately 1 linepair per x .

Now that the intrinsic resolution is known the divergence contribution can be assessed. From the geometry and the theory of neutron guides it follows that the beam divergence is twice the angle of critical reflection inside the guide at the exit side. For a Ni coated guide the critical angle is 0.1° per \AA . Using a mean energy of 5.5 \AA this yields an effective divergence of 1.1° . In reality the situation is a little more favourable because the reflectivity starts dropping for angles below the critical angle due to imperfections in the coating of the guide. To determine the contribution from the divergence the edge was imaged at different distances from the scintillator and each time the resolution was calculated as described above. The result can be seen in figure 4.5. At close distances the intrinsic resolution is dominant while for increasing distances the linear rise due to the geometric unsharpness becomes apparent. This is in agreement with the theory that states that the geometrical unsharpness increases with a factor $1/(L/D)$ relative to the distance. Using the intrinsic resolution of $540 \text{ }\mu\text{m}$ we calculated the best fit to equation 4.1. For the PGA beamline this results in a measured L/D of $1/0.0166$ or 60. This is in relative good agreement with the theoretical

lower boundary of $1/\tan(1.1)=52$.

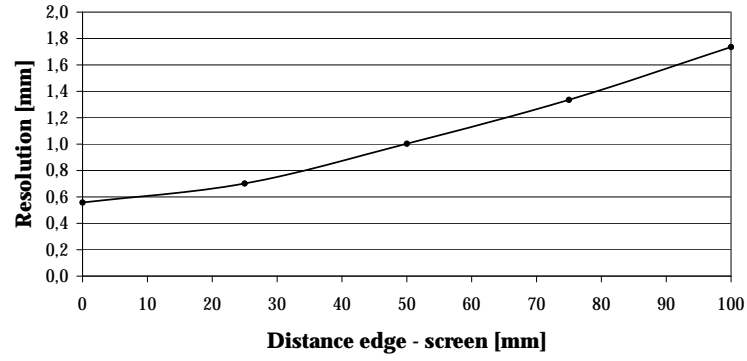


Figure 4.5: Resolution as function of distance to scintillator [mm]

In a practical tomography setup the sample has to rotate in front of the detector. The shape of the sample and the motor stage define the closest possible distance and thus also the best possible resolution. In this setup the typical distance between the detector and the rotation axis is about 25 mm. From figure 4.5 it then follows that the effective resolution in that case will be around $700 \mu\text{m}$.

4.2.4 Experiments with the first PGA setup

The first experiments performed at the PGA beamline were mainly intended to explore the possibilities and limitations of the setup as described above. Different types of samples were examined to become familiar with the technique, to explore possible applications and to identify typical problems and limitations in neutron tomographic imaging. A selection of the good results is presented here.

A tooth with mercury-containing amalgam fillings.

A possible medical application is the study of human teeth with amalgam fillings. Dental filling amalgam contains about 50% metallic mercury (the remaining 50% is composed mainly of silver and tin). Because of the high toxicity of mercury to the human body, especially to the nervous system, there is an increased interest in the study of the diffusion of mercury from the fillings into the tooth. A heavy high Z metal such as mercury poses a big challenge for X-ray based tomography. Due to the extremely high absorption of the mercury in the amalgam these samples cannot be penetrated using X-rays. This became clear in experiments we performed at the ESRF [10].



Figure 4.6: Neutron tomography of teeth with amalgam fillings.

Figure 4.6 shows some tomographic reconstructions of different teeth that were imaged with cold neutrons. The vertical cut of the three-dimensional reconstruction shows the core composed of soft pulp (black), surrounded by a layer of dentine (yellow) that is coated with enamel. The filling is the strongest neutron absorber and can be clearly distinguished (purple). No evident trace of mercury has been found in the inspected teeth, but further analyses have to be done to determine the limits of the method. To illustrate the difference in resolution figure 4.7 shows the comparison between a cross-section of a scan made with neutrons (left) and one recorded with X-rays from a similar experiment at the ESRF (right). It is immediately clear that the resolution of the neutron tomography cannot compete with X-ray tomography. Cracks in the teeth (caused by drying) that are easily

visible in the X-ray reconstructions are not visible in the neutron image. In terms of dynamic range however the neutron images are better, because the neutrons penetrate the amalgam more easily. The camera recorded a useful signal even in the most absorbing parts of the teeth. This was not the case with the X-ray scans, resulting in severe artefacts in the reconstructions.

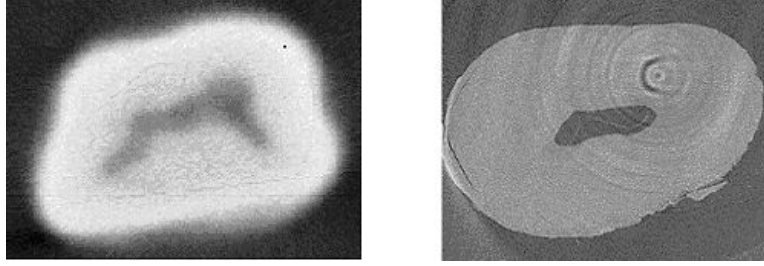


Figure 4.7: Comparison of the spatial resolution with neutrons (left) and X-rays (right)

Rat skull.

To illustrate that neutron beams can be used to study bony materials a small animal skull was scanned resulting in good, contrast-rich images shown in figure 4.8. The contrast is similar or even better than that obtained with X-rays, but the resolution is worse. The densities were classified into three categories. The main matrix was rendered grey, medium densities in green and the highest densities, corresponding with the teeth, in red.

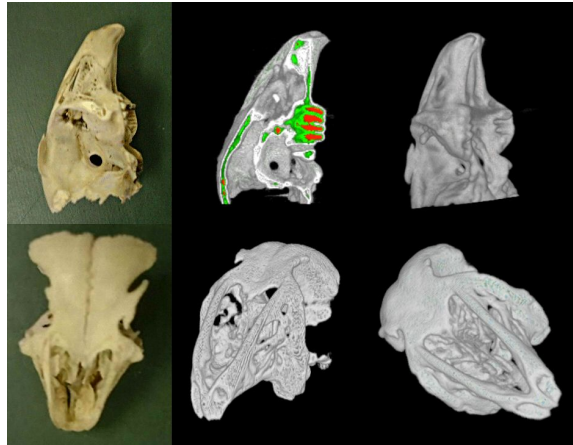


Figure 4.8: Different views of a neutron tomography of a rat skull (3 cm long).

A marble sample from a statue.

In the case of architectural or geological samples, iron rich inclusions often prove problematic for X-ray based tomography. The highly attenuating iron causes strong artefacts in the reconstructed images. The relatively low cross-section of iron for neutrons eliminates this problem. An example is shown in figure 4.9, featuring a marble sample of a roman statue. Neutron tomography enables the study of the size and distribution of the inclusions in a non-destructive way. This can provide added value when combined with elemental analysis data, for example from neutron activation analysis, because these techniques yield no spatial information.

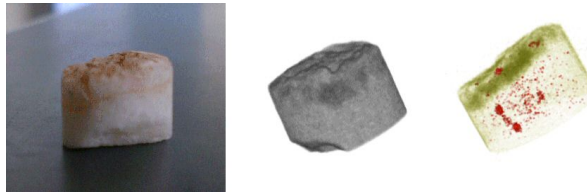


Figure 4.9: Neutron tomography of a marble sample (1 cm wide). The stone matrix is rendered transparent to reveal high density inclusions (red).

A mercury containing ore called cinnabar.

Another geological sample is an ore from the Toscana region in Italy. This ore called cinnabar contains high amounts of mercury (as mercury-sulfide) and the mercury distribution was known from previous experiments at the ESRF using element sensitive tomography. The reconstruction of the neutron tomography of this ore is shown in figure 4.10. Neutron tomography also allowed to discriminate the mercury from the stone matrix, with good contrast, but again the resolution cannot compete with the X-ray results. The layered deposit of mercury can be located on the outside of the sample.

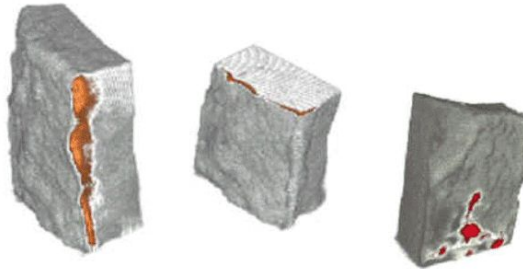


Figure 4.10: Neutron tomography of a mercury rich ore (2 cm high, mercury in red and orange)

Electronic components.

Electronic components often contain metal parts. Figure 4.11 shows an EPROM (Erasable Programmable Read Only Memory) chip in a plastic socket. Both can be discerned easily, allowing segmentation and separation of the different components. The metal pin connectors can be identified too. Figure 4.12 shows a steel encased electromotor. This type of component with solid metal parts is hard to image with X-rays because of the strong absorption. Neutron tomography has a particularly strong potential for quality control of metal containing or metal encapsulated objects such as capacitors, spark plugs, relays and switches.



Figure 4.11: Neutron tomography of an EPROM chip (2 cm long) in its plastic socket (left), the chip by itself (middle) and the socket by itself (right).

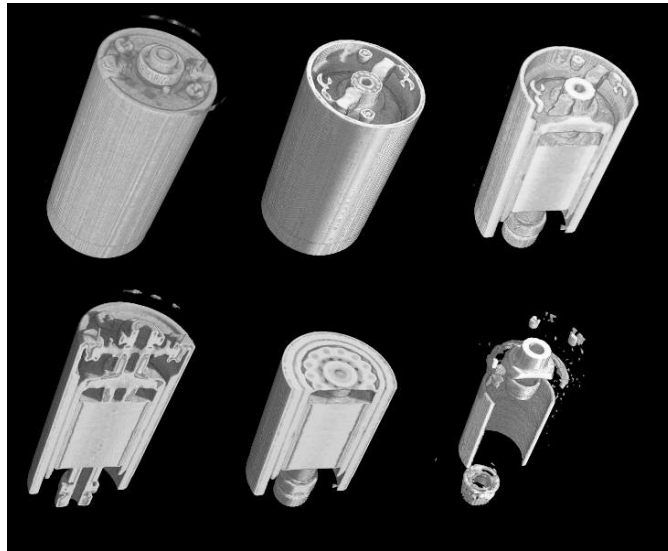


Figure 4.12: Different views of a neutron tomography of a small electromotor (2 cm long). By making cuts through the virtual volume or rendering particular densities transparent we can make the different components visible.

First dynamic radiography experiments.

The relatively high flux at the PGA setup combined with the fast frame-rate of the Sensicam camera made it possible to perform some early dynamic neutron radiography experiments with cold neutrons. Most research groups that are active in this field use thermal neutrons to study big dense objects like car engines to visualise the oil distribution on the inside. The cold neutrons at PGA show higher cross-sections and are therefore better suited for small objects. A sample was prepared that would also illustrate the complementary character of neutron imaging compared to X-rays. It consisted of a lead cylinder with a wall thickness of 1.5 cm. A small amount of water was inserted together with a paper tissue. This tissue paper immediately starts absorbing water so acquisition was started as quickly as possible after insertion of the tissue. The field of view was about 3 by 4 cm, so the beam with its width of 2 cm only illuminates part of the field of view. A sequence of 38 radiographs was shot at a rate of 1.4 Hz and figure 4.13 shows 5 of these frames. The dark horizontal line indicates the top of the lead container (the outer limits of the container are outside the illuminated area). The rising water is clearly visible through the centimetres of lead, something that would be impossible using X-rays. The camera hardware allows a full frame rate of 8 Hz and even more when using binning or limiting the so called Region Of Interest (ROI). More technical specifications on the camera can be found in Appendix B. These experiments represented the first steps towards dynamic tomography. Section 4.7 will describe a much more advanced setup for dynamic tomography that was installed at the high flux research reactor at ILL in Grenoble.

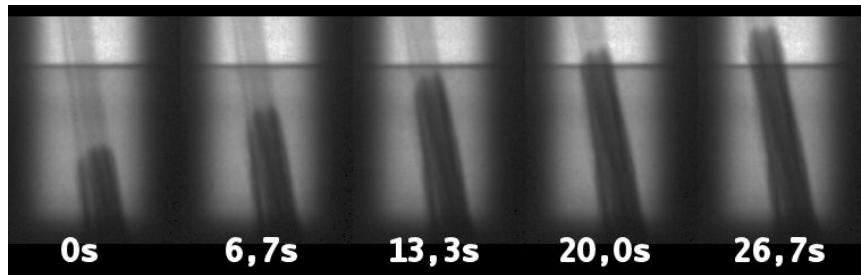


Figure 4.13: The first dynamic radiography experiments showing water rising in tissue paper inside a lead container.

4.2.5 Towards higher resolution using thinner scintillators

It was clear that the resolution was limited mainly by the scintillator and the beam divergence. To address the first problem Applied Scintillation Technologies was asked to produce two scintillators especially for this experiment. Both were made with the same composition as the standard one but without an aluminium backing and with a thickness of 200 and 100 μm . This made the scintillators very fragile and difficult to handle but should improve the resolution significantly.

The setup was the same as in 4.2.3. First the general image produced by the new scintillators was judged visually. No obvious inhomogeneities could be seen in the scintillator response so as a next step, the resolution could be measured. Only the intrinsic part of the resolution is now of interest, so the 25 μm thick Gadolinium foil was placed directly against the scintillator. Again line profiles were taken perpendicular to the edge and the corresponding ESF and LSF were measured. Figure 4.14 shows the resulting ESF for the three scintillators, the standard 420 μm and the two new ones.

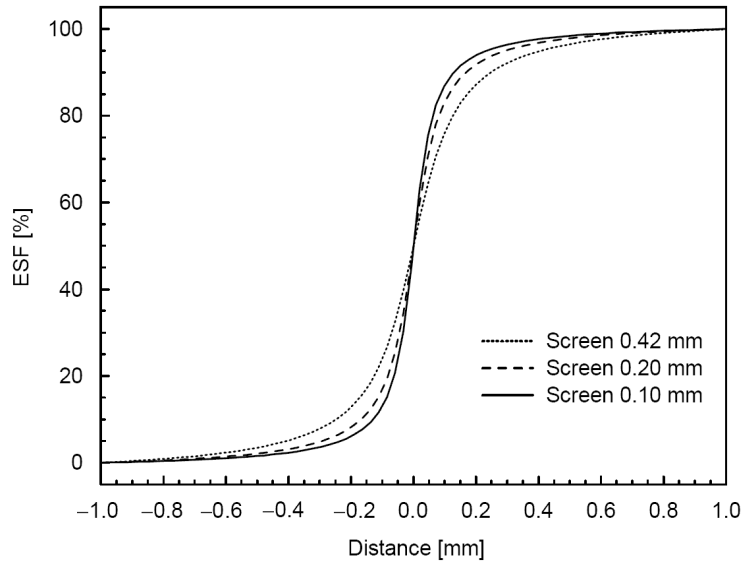


Figure 4.14: Measured ESF for the three scintillators.

It is immediately clear that the thinner scintillators show a sharper rising edge and so have a better resolution. From these ESF data the resolution was calculated, again using the 10%-90% method. The results are shown in table 4.1. The thinner scintillators show significantly improved resolutions. When the resolution is plotted against the scintillator thickness a linear relation becomes apparent. Figure 4.15 makes this clear. Whereas the resolution gets better in a linear fashion the light output does not decrease in the same way. Due to less selfabsorption in the thinner screen the efficiency drops

less than linear with the thickness. This is apparent in figure 4.16. In fact the small efficiency gain between the 200 μm screen and the standard 420 μm screen suggests that the reflective aluminium backing of the standard screen hardly contributes to the light output.

| Thickness (mm) | Resolution (mm) | Relative efficiency (%) |
|----------------|-----------------|-------------------------|
| 0.42 | 0.54 ± 0.02 | 100 |
| 0.20 | 0.34 ± 0.01 | 85 |
| 0.10 | 0.24 ± 0.01 | 64 |

Table 4.1: Resolution and efficiency as function of thickness

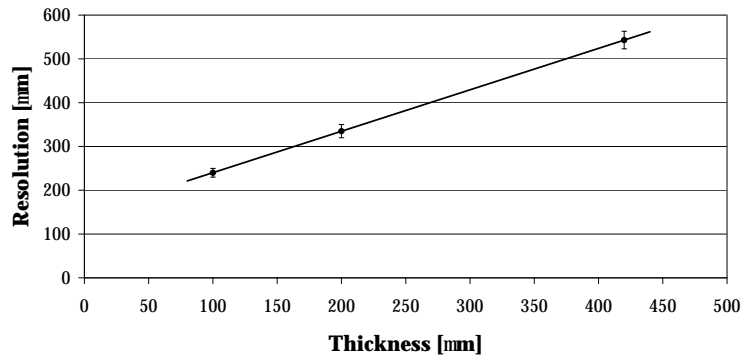


Figure 4.15: Resolution as function of scintillator thickness

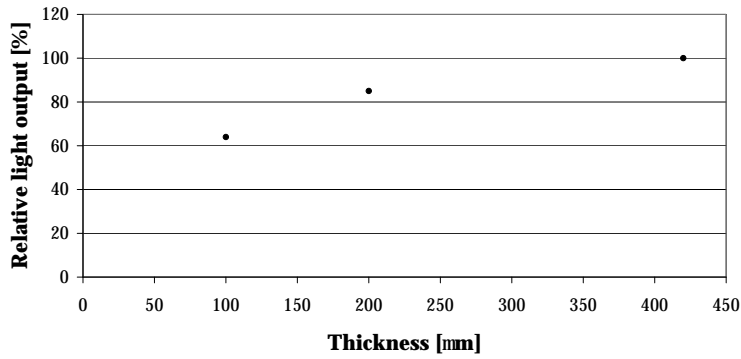


Figure 4.16: Efficiency as function of scintillator thickness

To confirm the observed results Applied Scintillator Technologies was asked to develop an even thinner screen of only 50 μm thick. Unfortunately it proved impossible to produce such a thin screen. In an attempt to go a step further the plan was conceived to take an X-ray scintillator called

Yttrium Aluminium Garnet (YAG) and dope it with ^6Li to make it sensitive to neutrons. YAG is a clear crystal scintillator, transparent for its own emission, and so it does not suffer from extra blurring caused by internal scattering. The ^6Li was implanted in the crystal using the ion accelerator at the University of Cologne. Unfortunately the ^6Li density proved to be too low to get sufficient sensitivity for neutrons to be useful. So at that moment the $100\text{ }\mu\text{m}$ screen was in terms of resolution the best solution.

4.2.6 Experiments using thinner scintillators

Some of the items that were investigated with the thinner scintillators are shown in the following pictures.

Spark plug.

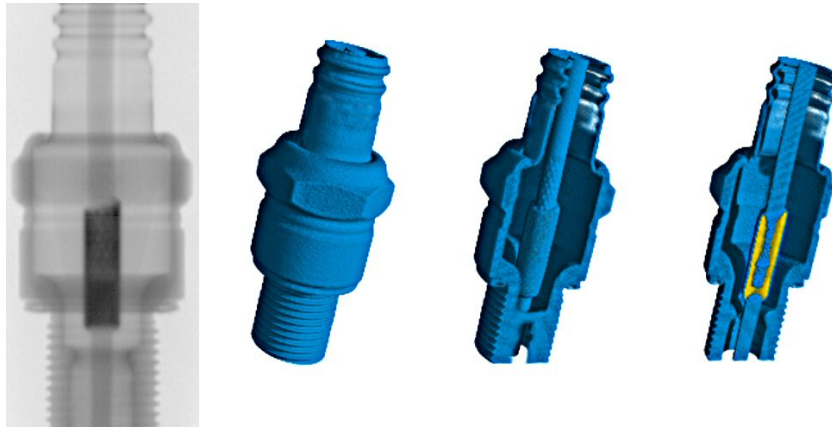


Figure 4.17: A spark plug imaged with the thin screen (4 cm high)

High current diode.



Figure 4.18: A high current diode (4 cm high).

Pyrotechnic cutter.

The higher resolution proved necessary in the quality control of a pyrotechnic rod cutter provided by Dassault-Aviation. Figure 12a and b show a picture of the object and a neutron radiography composed of 8 individual exposures. Cold neutrons were able to penetrate the object even though covered by steel cladding. The reconstructed object is shown in Figure 12c where components representing different materials were extracted from the volumetric data set. For instance, O-rings containing lots of hydrogen were easily segmented and could be controlled in minute detail³.

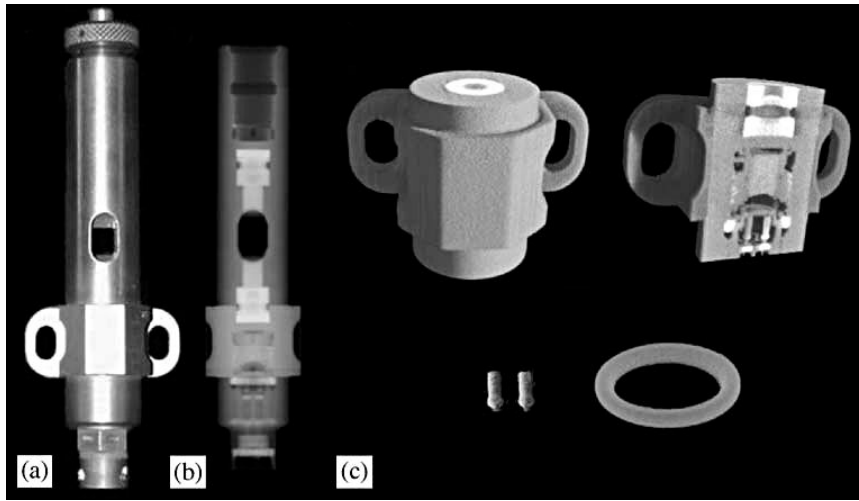


Figure 4.19: Quality control of an Ariane rocket detonator. Original photograph (a), a single radiography (b) and a number of views of the reconstructed result (c). An O-ring was easily segmented and checked for defects (bottom right)

4.2.7 Conclusion

We can conclude that the PGA setup proved highly successful. The high neutron flux enabled fast, efficient tomographic scanning. The cold neutrons provided contrast-rich images, even in thin samples. The highly sensitive CCD-camera/scintillator based detection system that was developed provided high resolution images that were in most cases limited by the divergence of the beam, caused by the neutron guide system. We demonstrated an array of diverse possible applications, and some of the measurements already provided valuable information to other researchers. Finally a lot of valuable lessons were learnt at PGA concerning the practical side of tomography. The PGA setup was reviewed in [81].

³Data analysed by Dr. S. Baechler of the University of Fribourg

4.3 A Focussing Neutron Lens

4.3.1 Introduction

The resolving power of the setup as described in the previous section is mainly limited by the scintillator, more precisely by its thickness. Using thinner scintillators proved one solution. In another attempt to circumvent this limitation an experiment was set up based on a neutron lens that would convert the essentially parallel beam to a cone beam. This way the projection of an object can be magnified on the scintillator while the resolution of the latter remains the same, thus leading to an increase in the relative resolution of the sample's projection. By changing the distance between the sample, the focal spot and the detector the magnification can be chosen. Bringing the sample closer to the focal spot will result in a larger projection and hopefully better resolution.

4.3.2 The neutron lens

Neutrons, being uncharged particles just like photons, cannot be focussed using electric fields. Their magnetic spin-moment can in theory be used to focus a neutron beam, yet practical limitations limit the application of this approach. The growing need for neutron optics has led to a new and fast evolving field of neutron optical devices. In the case of cold neutrons their wave-nature can be exploited to reflect them at a suitable surface. One recent development based on this property is a neutron lens, the first one being made in 1991 at the Institute for Röntgen Optics (IRO) in Moscow [82]. This device is a bundle of millions of glass fibres, each with a polycapillary structure. At the entrance side these are all parallel while at the exit side the fibres are bent in such a way that they converge and point to a focal spot. Neutrons entering one of the capillaries are transported through the lens in a series of total reflections. The lens can be seen in figure 4.20. The lens is approximately 16 cm long and the focal point is situated 15 cm beyond the exit side of the lens. The beam diameter at the waist at the focal point is less than 1 mm and the neutron flux at the focal spot is about 30 times higher than the incident flux accepted by the lens. The total transmittance of the lens is a mere 1%. To stop background neutrons from hitting the scintillator a 5 mm thick Li pinhole collimator with a 1 mm diameter is placed at the focal point.

4.3.3 Beam characteristics

The lens is placed directly behind the exit window of the beam guide. The resulting beam profile after the neutron lens is far from homogeneous as can be seen in the left picture in figure 4.21. From the line profile in figure 4.22 it follows that there is a three times higher intensity near the centre of

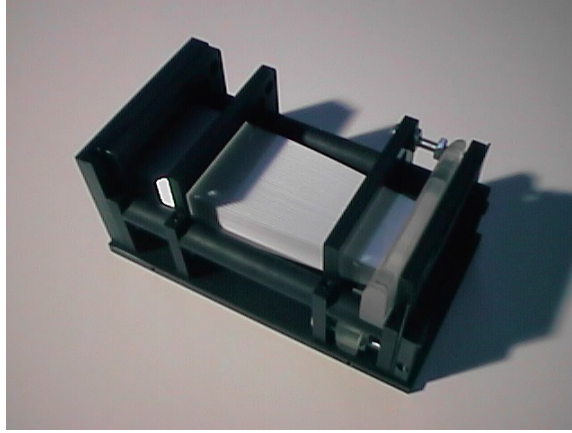


Figure 4.20: The neutron lens

the image than in the surrounding areas. This is due to the acceptance of the neutron lens, preferring neutrons near the axis. Such a beam profile is not ideal at all for tomography. Therefore a small Gd absorber was made to attenuate the centre portion of the beam at the cost of a reduced beam intensity. It consisted of two $25\text{ }\mu\text{m}$ thick discs, one with a diameter of 0.5 mm and one of 1 mm , placed on top of each other. The resulting beam profile had indeed a less pronounced central peak as shown in the right picture in figure 4.21. But there were still differences of a factor of three present (figure 4.23), so together with the even further reduced intensity this proved no real success. Most experiments were therefore done without the Gd absorber. Finally one more aspect that is evident from figure 4.21 is the high number of white spots in the image. This is a consequence of the low efficiency of the lens leading to much longer exposure times. This way more gamma rays are registered by the CCD as bright spots⁴.

The intrinsic resolution of the imaging system is still the same. The beam divergence is now completely different than in the case without lens. Instead of having a quasi-parallel beam with a certain divergence we now have a cone beam geometry. The total resolution was measured using the knife edge method for different combinations of sample and detector position. The results are presented in table 4.2.

The column OS indicates the distance between the object and the source, i.e. the focal spot. The distance between detector and source is indicated by DS. The ratio DS/OS then defines the geometrical magnification. The 10%-90% values are relative to the detector, whereas the resolution in the

⁴Some of the white spots in the image are actually rendered as black spots. The visualisation software we developed allows to set a threshold colouring all pixels with a higher intensity than the set level. This is used mostly to judge overexposure. In greylevels this causes the highest values, normally white, to be rendered black.

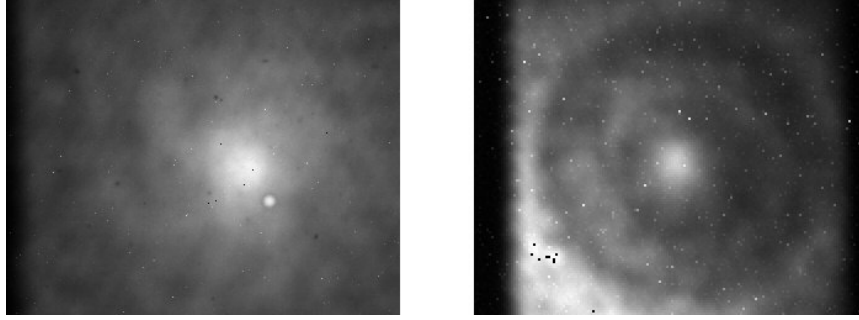


Figure 4.21: Beam profile without and with Gd disks

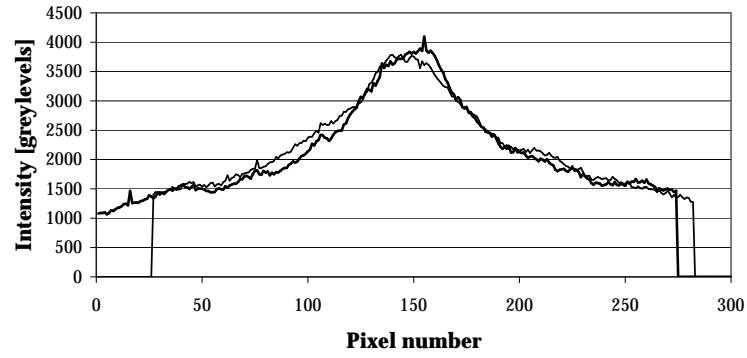


Figure 4.22: Line profiles through center without disks

| OS [cm] | DS [cm] | Magnif. | 10%-90% [pix] | 10%-90% [μm] | Resolution [μm] |
|---------|---------|---------|---------------|---------------------------|------------------------------|
| 17 | 70 | 4,12 | 24,35 | 2191 | 532 ± 16 |
| 23 | 70 | 3,04 | 17,81 | 1603 | 527 ± 14 |
| 35 | 70 | 2,00 | 9,74 | 877 | 438 ± 13 |
| 50 | 70 | 1,40 | 7,95 | 715 | 511 ± 16 |
| 65 | 70 | 1,08 | 6,66 | 600 | 557 ± 18 |
| 17 | 35 | 2,06 | 10,51 | 946 | 459 ± 13 |
| 10 | 30 | 3,00 | 17,43 | 1569 | 523 ± 24 |
| 15 | 30 | 2,00 | 12,05 | 1084 | 542 ± 26 |
| 30 | 30 | 1,00 | 6,41 | 577 | 577 ± 29 |

Table 4.2: Resolution and efficiency as function of thickness

final column is relative to the sample. From the data we can conclude that in most cases the resolution does not improve using the lens. The attainable resolution is about the same as the intrinsic resolution of the setup without lens. Only the situations 3 and 6 with a magnification of about 2 give a small but significant improvement.

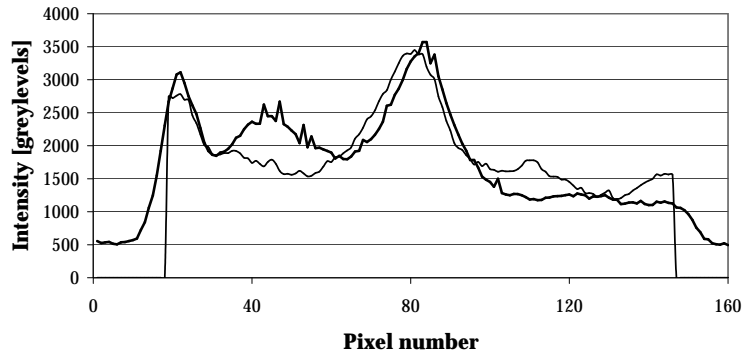


Figure 4.23: Line profiles through center with disks

4.3.4 Experiments using the neutron lens

A wasps' nest is a typical example of an object that is hardly visible with X-rays because of its low density. But due to the organic nature it is easily visible with neutrons as seen in figure 4.24. Notice the noise in the image caused by poor statistics due to the low neutron flux.

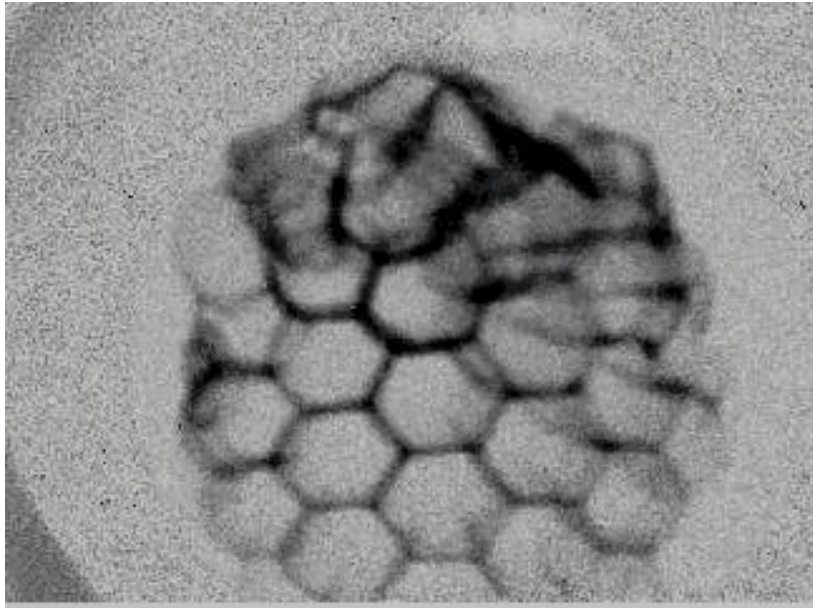


Figure 4.24: Neutron radiography of a wasps' nest (4 cm, no magnification)

As an example of a biological application we show a tomography of a reef coral (figure 4.25). The pore size distribution is studied to assess damage from worms to the reef. In this particular case the resolution of the neutron tomography was insufficient to visualise the smallest pores.

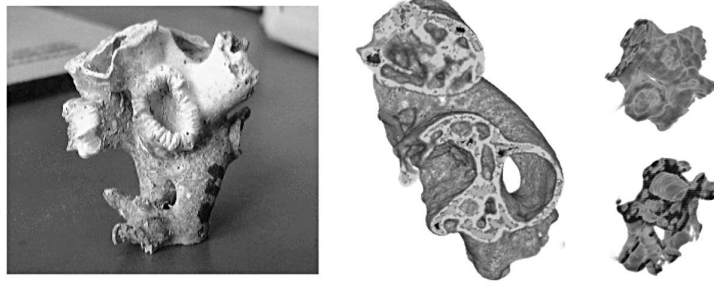


Figure 4.25: A reef coral (2 cm high) for study of pore size distributions

Another typical example of a sample that is not suited for X-ray tomography is this capacitor (figure 4.26). The metal casing blocks the X-rays, but neutrons are most sensitive to the more interesting electrolyte inside.

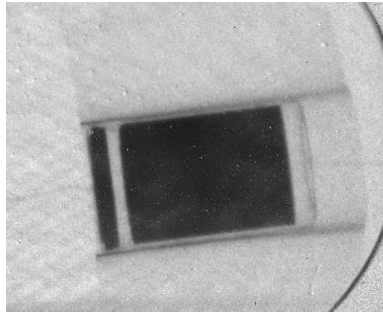


Figure 4.26: A neutron radiography of a capacitor, showing the electrolyte inside (black), without being hampered by the metal casing

4.3.5 Conclusion

In principle a neutron lens could be a solution to increase the resolution of a given setup. To be effective the size of the focal spot of the lens has to be smaller than the resolution achievable with the setup with no lens. This was not the case in our measurements, the spot size was about two times larger than the resolution achieved without a lens. In addition the resolution advantage has to be significant to overcome the disadvantage of a strongly reduced beam intensity and thus much longer exposure times. But as technology advances neutron lenses may become more important. The results of these experiments have been published in [83].

4.4 Measurements at NCR

4.4.1 Introduction

At the SINQ facility there was at the time of the experiments only one other experimental station suitable for cold neutron radiography, namely NCR, which stands for Neutron Capture Radiography. It seemed appropriate to try and compare the performance of both stations. The setup was transferred and installed in the small NCR bunker. NCR was never designed to be a radiography beamline, so the working space was limited and access was difficult. The beam parameters were investigated as in the PGA case. Resolution and divergence were measured, the different scintillators were again evaluated and this time compared to a commonly used X-ray scintillator. In an attempt to improve the divergency of the beam a device called a Soller collimator was installed and tested. Finally some more applications were explored.

4.4.2 The NCR beamline

NCR is used mainly for imaging the boron distribution in materials like biological tissues or metals. The image is recorded using track-etch foils placed behind the sample during irradiation and read out afterwards. Unlike PGA the NCR station is situated at the end of a cold neutron guide that is completely supermirror coated. As a result the neutron flux is 4.9×10^8 , again for a typical proton current on the target of 1.2 mA. This is four times higher than at PGA. Because of the supermirror coating the effective divergence of the beam is also higher. The critical angle for total reflection as function of the neutron wavelength now becomes 0.2° per Å. Using a mean energy⁵ of 5.2 Å this yields an effective divergence of 1.04° or a L/D value of $1/0.036$ or 28. Earlier measurements of L/D by others [84] resulted in a value of 50 ± 10 . The useful beam area was 30 mm wide and 120 mm high.

The camera system was set up in such a way that the field of view covered an area on the scintillator of 2.7×3.4 cm². This way 1 pixel on the CCD corresponded to a 26×26 μm² pixel on the scintillator. In the case of tomography experiments the axis of rotation of the sample could not be placed closer than 8 cm from the detector for practical reasons. This immediately strongly limits the attainable resolution because of the high divergence of the beam. The Soller collimators, intended to improve the beam divergence, could not be installed together with the motor stage because of the limited working space. As a consequence most experiments were limited to radiography.

⁵Measured by prof. Kobayashi, 1999, http://ncr.web.psi.ch/ncr_facility/

4.4.3 Experiments

The resolution measurements with the three scintillators were repeated to confirm previous conclusions under rather different circumstances. To minimise the blurring contribution from the imaging system the aperture of the lens was set at the maximum value of 22 (smallest opening)⁶. The measured Edge Spread Functions (ESF) are shown in figure 4.27. Also at our

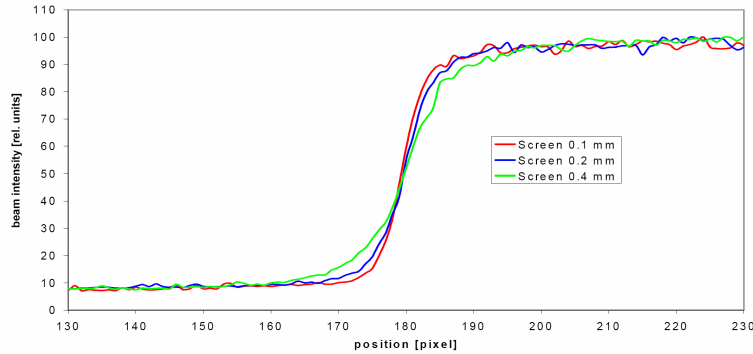


Figure 4.27: Intrinsic ESF for different scintillators measured at NCR

disposal this time was a much used scintillator screen in medical environments, a Kodak Lanex Fast Screen. Made of $\text{Gd}_2\text{O}_2\text{S:Tb}$ this screen also works as a neutron detector due to the Gd in it. It turned out to have a resolution of $290\text{ }\mu\text{m}$, halfway between the performance of the 200 and $100\text{ }\mu\text{m}$ screens. Unfortunately the efficiency was almost 8 times worse than the standard $^6\text{LiF/ZnS:Ag}$ screen and it proved to be highly sensitive to the gamma background radiation resulting in a high number of white spots in the image.

Next the divergence of the NCR beam was investigated. The ESF was measured at 5 different distances from the screen, ranging from 8 mm to 88 mm. These measurements were done with the thinnest scintillator. The top line in figure 4.30 represents these data. All the data points are on a straight line, indicating that the divergence quickly dominates over the intrinsic part. From the slope of this line, equal to $1/(L/D)$ follows that $L/D=1/0.0192=52$ confirming the earlier measurements by others [84].

To improve the divergence of the beam a device called a Soller collimator was installed and tested. Soller collimators are made by stacking thin neutron absorbing layers with spacers between them. In the case of neutron collimators this is mostly done by using thin PETP foils coated with a neutron absorbing material like gadolinium or boron. A picture of such a

⁶In hindsight this may have been a wrong assumption. General consensus says that spatial resolution improves with larger aperture settings (smaller openings). Few people know that at very small aperture settings the resolution becomes worse again due to diffraction. This is especially important with small sized detectors like CCD's.

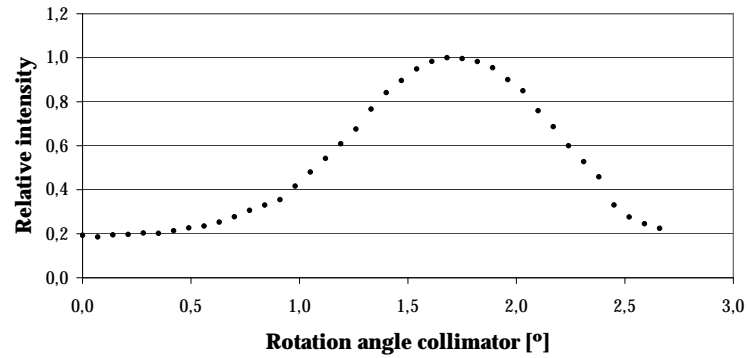


Figure 4.28: Relative transmission as function of angle



Figure 4.29: A Soller collimator and the measured beam profile

collimator is shown in figure 4.29. Typical collimation angles are of the order milliradians while typical transmittance is more than 80%. The collimator used for these experiments had a stated collimation angle of 5.8 mrad (0.33 degrees). This corresponds to a theoretical L/D of $1/\tan(5.8)=172$.

To align the Soller collimator optimally, it was placed on a high precision rotational stepper motor. The mean intensity of the white beam is plotted as function of the rotation angle in figure 4.28. A clear maximum is observed. At this optimal position the effective transmittance was measured to be about 20%. This value should not be compared to the above mentioned transmittance of 80%. The latter only holds in the ideal case of a perfectly parallel beam and gives an indication of the amount of beam area that is blocked by the absorbing layers. The recorded beam profile, as shown in figure 4.29, clearly shows the presence of the absorbing blades as vertical bands in the image. These should even out when placing the detector further away from the collimator. In addition the longer acquisition times and the very high activation in the small NCR bunker caused high numbers of white

spots in the images.

The resolution was again measured using the Gd foil and the results can be seen in figure 4.30. For comparison the data from the PGA station have been added too. The slope of this straight line indicates the L/D, resulting in a value of 133. This is in good agreement with the theoretical value of 172 that follows from the collimation angle. It should be noted that the resolution was measured along a vertically oriented edge. The collimator blades are also vertically oriented and thus the divergence is only improved in horizontal planes. To be fully effective a second Soller collimator should be installed with its planes perpendicular to the first one. Again the limited working space in the NCR bunker prevented us from trying this.

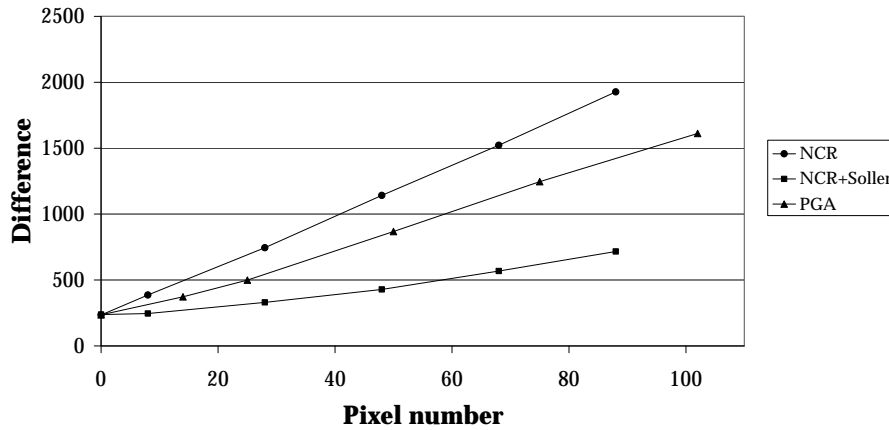


Figure 4.30: Resolution as function of distance with and without Soller

After the beam parameters had been characterised some samples were investigated. Two results are shown here showing the big improvement by using the thinner scintillator. The first images (figure 4.31) show two radiographies of a relay. It is immediately apparent that the image recorded with the 100 μm scintillator on the right shows more details and sharper outlines than the image on the left which was recorded with the standard 420 μm screen. The second set of images (figure 4.32) shows a tomographic reconstruction of a small metal lock. Again using the thin screen (right) yields clearly more detail than the standard one (left).

4.4.4 Conclusion

The NCR station was not designed for doing neutron imaging. Nevertheless it offers some good performance characteristics, namely a high flux due to the fully supermirrored guide, and a large useful beam area of 30 mm by 120 mm. In addition the high divergence allowed us to evaluate the effectiveness of using Soller collimators to improve the resolution as function of distance.

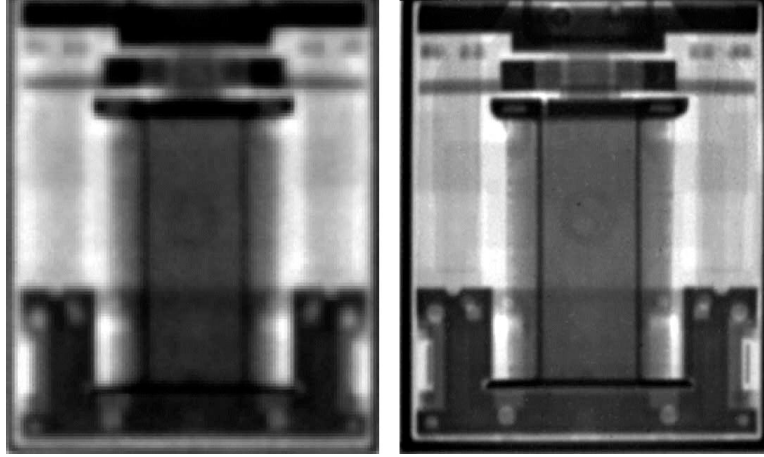


Figure 4.31: Radiography of a relay (2 cm high) recorded with the 420 μm (left) and the 100 μm screen (right)

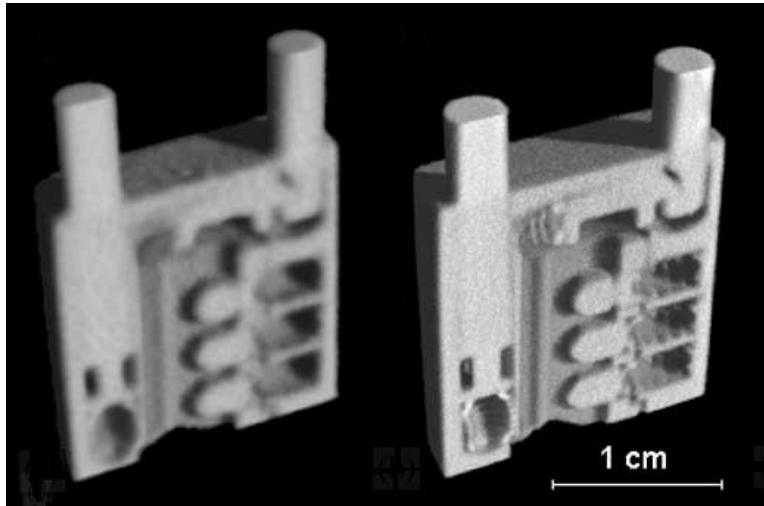


Figure 4.32: Tomography of a lock recorded with the 420 μm (left) and the 100 μm screen (right)

The conclusion here is that Soller collimators can be useful in situations where space is an issue. In other situations it is probably better just to install a drift tube and place the detector system further from the beam exit window. In the mean time the NCR station has been dismantled and a new cold neutron radiography/tomography station at the same position is under development. The experiments described here will help making the right design choices to build a high performance neutron imaging station. They were published in [85].

4.5 Mono-energetic Neutron Tomography

4.5.1 Introduction

So far the developments towards better neutron imaging methods were mainly focussed on improving the spatial resolution. But in Chapter 2 we mentioned how the neutron attenuation depends on the energy of the neutron beam. For cold and thermal neutrons the absorption part of the cross-section is roughly inversely proportional to the neutron's velocity by an element specific factor. As a natural next step, this energy dependence could be exploited to change the relative contrast between different materials and thus get more information from the samples. Therefore a tuneable monochromatic neutron beam is needed. This chapter describes how a neutron velocity selector was installed at the PGA station to make a quasi-monochromatic source. The resulting beam is characterised and possible applications are demonstrated.

The Bragg cutoff

In Chapter 2 we also mentioned that the scattering cross-section is largely independent of the energy. This is true for amorphous materials. But many polycrystalline materials (mostly metals) show a strong and sudden discontinuity in their scattering cross-section at a certain energy. This energy depends on the element and typically lies between 3.5 and 5.5 Å, so in the cold neutron range. This phenomenon is called the Bragg cut-off. The reason is that when the wavelength of the neutron becomes larger than twice the separation of the most widely spaced planes in the crystal coherent elastic scattering over large angles is no longer possible. This causes a sudden drop in the scattering cross-section. Using a tuneable monochromatic source would make it possible to image a sample at energies once below and once above the edge, thus identifying the presence of the element under study. Conceptually this is a very similar approach to work done in our research group in Ghent using the K-edge seen in X-ray absorption curves [6, 9, 7].

Monochromatisation methods

Most facilities that have monochromatic neutron beams are pulsed neutron sources. The neutron energy can be chosen using a Time-of-Flight technique (TOF). When dealing with a continuous source a chopper system can be used in combination with TOF to achieve energy selection. Both result in a well defined energy spectrum and a relatively high neutron flux. For highly monochromatic beams one can use the classical Bragg reflection on a monocrystal, similar as with X-rays. But the narrow acceptance results in a very weak beam, making it difficult to perform tomography or even radiography. Many other techniques exist based on refractive compound

lenses, thin-film multilayers etc. In the context of radiography the main issue is a sufficiently high flux to achieve reasonable exposure times. In this case the best option is a neutron velocity selector because of its broad transmitted spectrum and thus high flux.

4.5.2 The velocity selector

Theory

A neutron velocity selector is a high speed turbine with helicoidal lamellae that are highly neutron absorbing. Only neutrons travelling along the axis with the right speed will manage to pass between two lamellae. Faster neutrons will hit the leading lamella while slower neutrons will be absorbed by the trailing lamella. For a detailed theoretical description of the functioning of a velocity selector we refer to [86]. Only a summary of the important equations and conclusions is given here. The selector is most easily described in the so called velocity space (\vec{v} -space). In this context the selector acts as a Soler collimator that is tilted and moving perpendicular to the axis of the neutron beam (figure 4.33). A simple formula for the transmission $T(v)$ can be derived if the \vec{v} -space distributions are approximated by Gaussian functions [87]. Then the transmission function is also a Gaussian with a width

$$\Delta v(FWHM) = \frac{v_0 \sqrt{\alpha^2 + \beta_0^2}}{\tan(\gamma)} \quad (4.3)$$

and a maximum transmission of

$$T_m = T(v_0) = \frac{T_m^0 \beta_0}{\sqrt{\alpha^2 + \beta_0^2}} \quad (4.4)$$

Technical Specifications

The velocity selector used in these experiments is a new generation selector manufactured by Astrium GmbH (formerly Dornier Satelliten Systeme GmbH) and is shown in figure 4.33. It has a maximum rotational speed of no less than 28300 RPM (stability 0.2 %) and a correspondingly high circumferential speed u of 430 m/s. Most mechanical selectors have a u -value of no more than 100 m/s. The rotor has a diameter of 290 mm and a length of 250 mm. It has 72 lamellae that are 0.4 mm thick and 60 mm high, twisted over 48.3° along the length of the rotor. To maintain the critical helicoidal shape at such speeds the lamellae are made of a carbon fibre reinforced epoxy resin. These are then individually glued in specially machined grooves in the rotor axle. The lamellae are coated with ^{10}B as a neutron absorber (35 g/m^2). To reduce friction and subsequent heating the turbine is placed inside a vacuum aluminium cylinder. Still a water cooling system

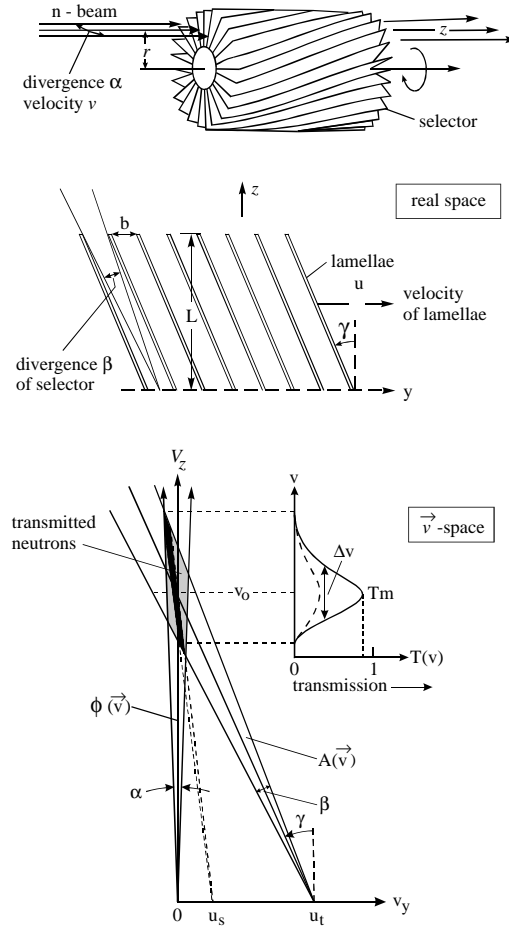


Figure 4.33: Selector description and representation

is needed to dissipate the heat caused by electrical losses. The two facing sides each have a 0.4 mm thick aluminium window for entry and exit of the neutron beam. The control and operation of the selector is done on a PC placed outside the bunker. Figure 4.35 shows a graph of the selected neutron wavelengths versus the rotational speed. This graph is only valid for this setup, based on a tilting angle of 12.7° . Notice the gaps in the graph, indicating frequency bands that are prohibited because of resonances in the construction. As a result the energies from 4.48 to 5.24 Å and from 8.08 to 9.35 Å could not be selected. The selector was placed at 25 cm from the neutron guide exit window, leaving 40 cm between the back of the selector and the camera system.

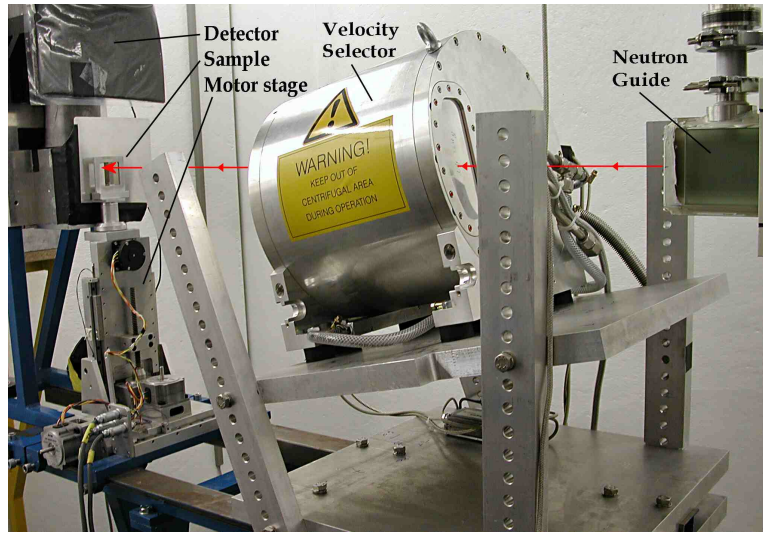


Figure 4.34: The Velocity Selector

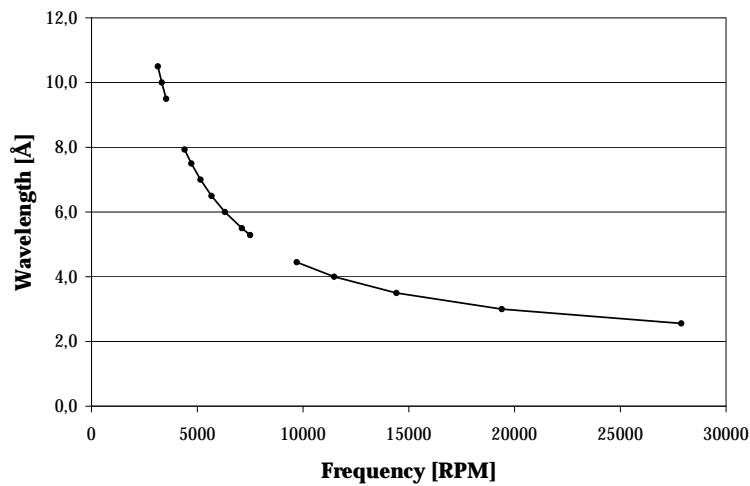


Figure 4.35: Selected energy as function of RPM

4.5.3 Beam characteristics

The beam profile was evaluated first for different energies and line profiles through the centre are plotted in figure 4.36. The general shape and profile of the monochromatic beams is similar to the white beam profile. In detail we notice for short wavelengths a pronounced breakdown to the right. For the middle range the profile is quite similar to the white beam profile, with only a slight breakdown. For the longest wavelengths the breakdown is towards the left side. The peak of the distribution gradually shifts towards the right

as the wavelength increases. The reproducibility of the velocity selector settings was verified by repeating the sequence of RPM settings twice. The line profiles in figure 4.36 are normalised to one, so the relative intensity information is lost. Therefore the mean intensity in a selected region of interest is calculated and normalised by the exposure time. The resulting relative intensity can be compared to that of the same area in the white beam image. The results are plotted in figure 4.37. This plot represents a rough estimate of the spectrum of the white beam, or more precisely a convolution of the spectrum with the transmission function of the selector. A maximum transmission of around 16% of the white beam intensity is observed at a selected energy of 5.4 Å. This confirms the Maxwellian distribution with a mean wavelength of 5.5 Å. The energy resolution $\Delta\lambda/\lambda$ was calculated to be about 30%.

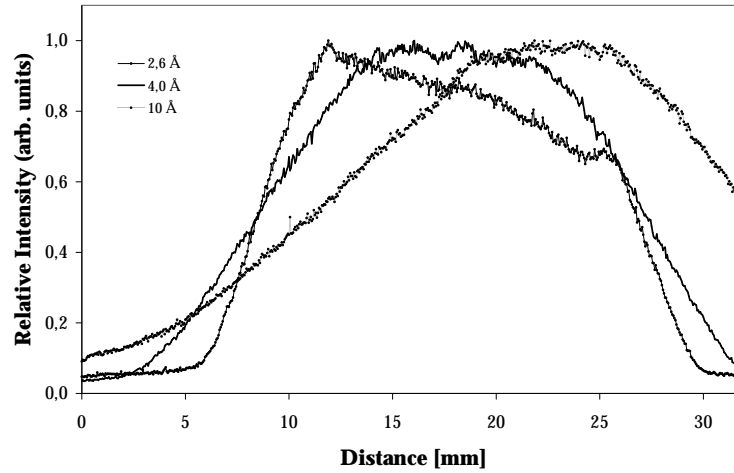


Figure 4.36: Line profiles for different energies

Next the resolution was measured as function of the energy using the knife-edge method. In the general theory of the selector it was mentioned that a selector acts as a Soller collimator moving sideways with respect to the beam. So an influence on the divergence and thus the resolution is to be expected. This time the Gd-foil was placed at a distance of 5 cm from the scintillator. The setup using the white beam had a resolution of 850 μm . As stated in 4.2.3 the divergence of the neutron beam at the PGA station was defined by the critical angle of 0.1° per Å. For the extremes of 2.7 and 10 Å this would result in a resolution of the order of 450 and 1700 μm respectively. The measurements are plotted in figure 4.38 and show a clear influence on the resolution. At the shortest wavelength of 2.7 Å the measured resolution is 450 μm , so defined solely by the divergence inside the neutron guide at this energy. The resolution gets worse in a linear fashion

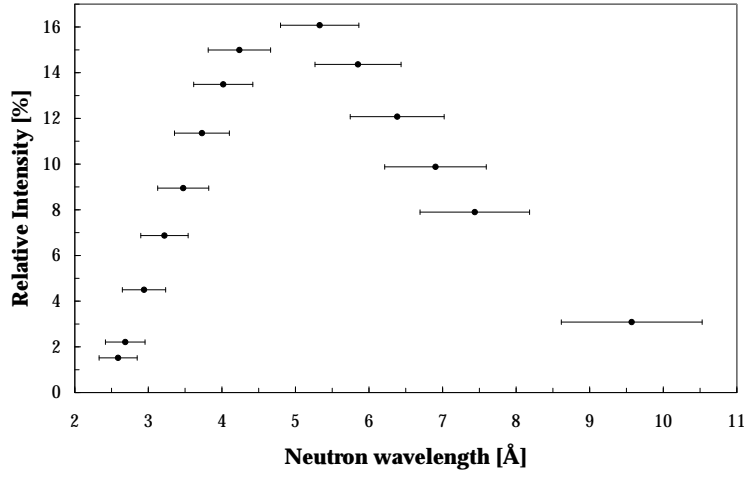


Figure 4.37: Relative intensity as function of energy

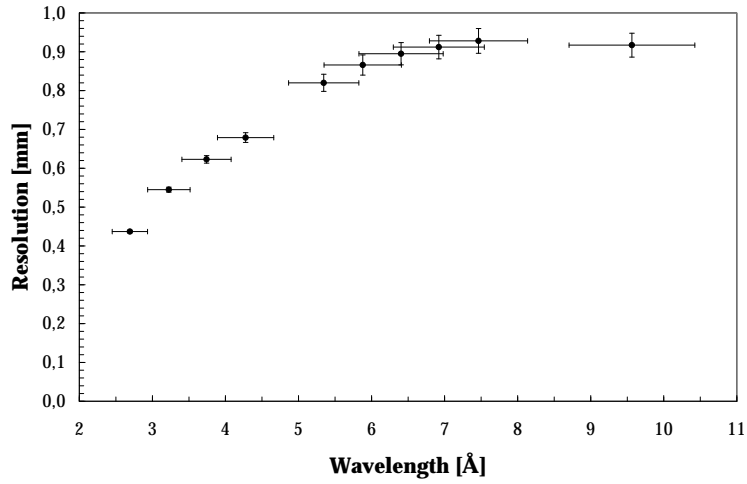


Figure 4.38: Spatial resolution as function of wavelength

as the wavelength increases up to about 7 Å after which it remains fixed at around 900 μm . From this wavelength on, the selector acceptance limits the divergence and functions as a collimator.

4.5.4 Experiments

Energy calibration

The neutron spectrum of the transmitted beam is only known from calculations. An actual measurement using a Time-of-Flight technique was not possible because of the limited space behind the selector. The energy calibration function shown in figure 4.35 is based on the following expression for the maximum of the transmitted spectrum [88]:

$$\lambda(v, \zeta) = \frac{A(\zeta)}{v} + B(\zeta) \quad (4.5)$$

The parameters A and B depend only on the tilting angle ζ , and were experimentally determined by another research group at SINQ using the same type of selector [88]. In order to verify this calibration a test sample was prepared consisting of different materials (Cu, Fe, Al, steel, Pb, PMMA and Teflon) with a thickness of 5 mm. For some of these materials tabulated cross-section data were available [89], allowing us to compare these with the measurements. For each selected energy a radiograph was made of the sample as well as an open beam image. From the resulting ratio I/I_0 and the attenuation law $-\ln(I/I_0) = \mu \cdot d$ the attenuation coefficient μ then followed. The results for Cu, Fe, steel, Teflon and PMMA are shown in figure 4.39.

For Fe and Cu the measurements can be compared to tabulated data [89]. Keeping the energy resolution of about 30% in mind there is a good qualitative agreement. Figure 4.39 b shows both Fe and steel. It is clear that there is only a small difference because both mainly consist of iron. PMMA (figure 4.39 d), better known as Plexiglass, is a hydrogen rich molecule ($C_5H_8O_2$) and therefore shows the typical monotonously increasing cross-section of hydrogen. Finally Teflon (figure 4.39 d) shows a somewhat unexpected behaviour. The decreasing cross-section for lower energies is particularly unusual. No obvious explanation was at hand.

Increasing spatial resolution

The possible improvement in spatial resolution is illustrated by 4.40. It features a dried hornet that was imaged⁷ twice, using a neutron beam at two different wavelengths, 2.7 and 5.3 Å. The specimen was fixed on a needle located at 2.5 cm from the converter plane. Both radiographs showed distinctly the three parts of the insect: the head with strong mandibles, the thorax with three pairs of legs attached and the abdomen tipped with the stinger. The wings were nearly transparent to neutrons and thus hardly visible on the radiographs. As expected, the monochromatic beam at 2.7 Å (short wavelength) yielded sharper edges and reproduced finer details in

⁷ Data analysed by Dr. S. Baechler of the University of Fribourg

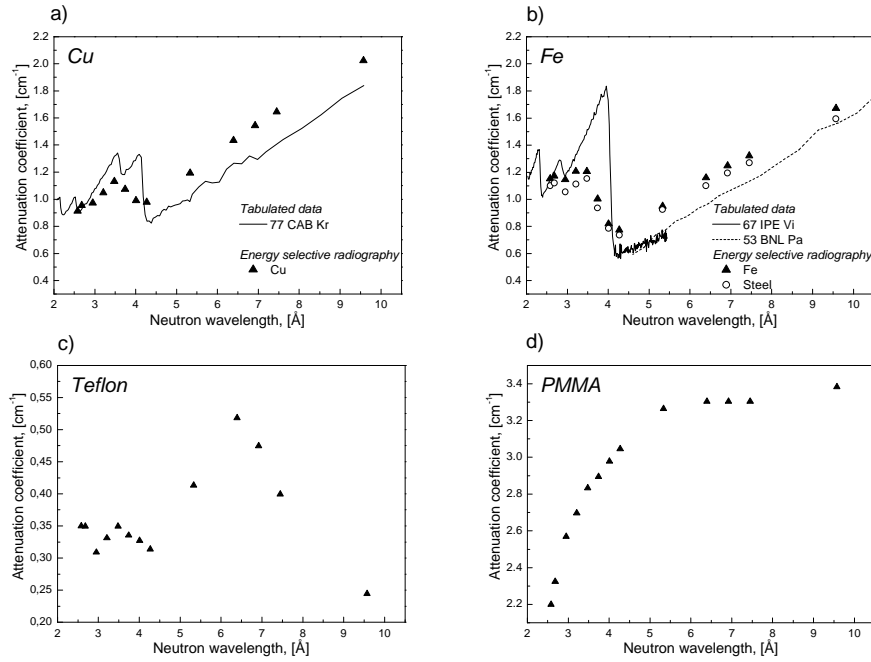


Figure 4.39: Measured attenuation coefficients μ of (a) Cu, (b) Fe and steel, (c) Teflon and (d) PMMA compared to tabulated data when available (a) and (b) [89]

the image. On the other hand, the contrast was improved at 5.3 \AA due to the increment of attenuation coefficient in organic material at higher wavelengths.

Changing the relative contrast

A first application was the inspection of an archaeological sample. An ancient Roman brooch that had already been investigated using standard thermal neutron radiography was now imaged using a monochromatic cold neutron beam. The brooch was known to be made of brass with a thin silver ornament on its surface. From tabulated cross-section data it was known that the attenuation in silver increased faster with decreasing energy than the one of copper, the main constituent of the brass. So to improve the contrast a wavelength of 6 \AA was chosen. A composition of both radiographs is shown in figure 4.41. The improved contrast in the monochromatic radiograph on the top is clear. The silver chain, barely visible in the thermal image, is now much more prominent. This shows that energy selective neutron radiography can yield much clearer information about a certain aspect of a sample, given a properly chosen energy.

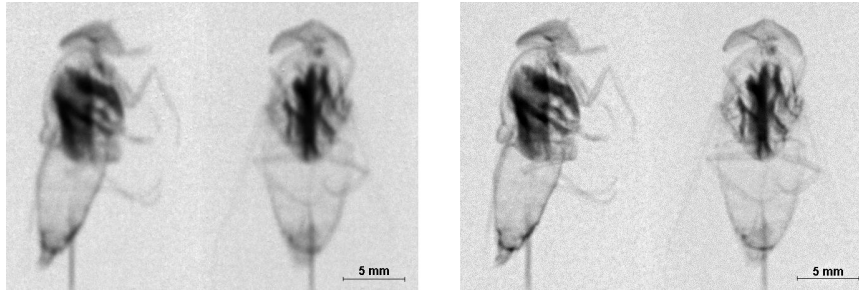


Figure 4.40: Spatial resolution at 5.3 Å (left) and 2.7 Å (right)

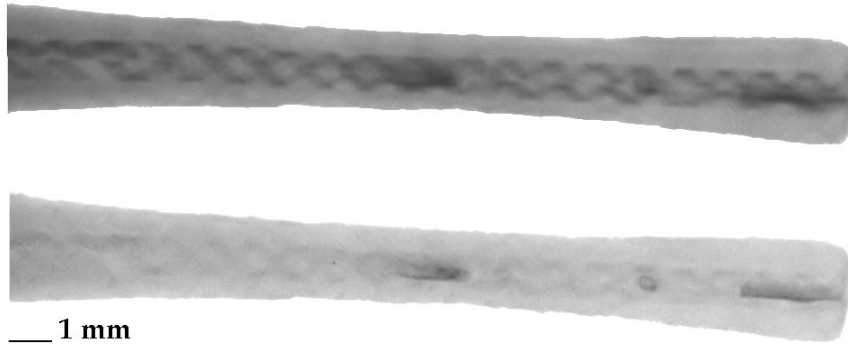


Figure 4.41: ESNR (top) vs. thermal radiography (bottom)

Using the Bragg cut-off phenomenon

The Bragg cut-off seen in polycrystalline materials can be used to enhance the transmission by selecting the energy where transmission is highest. To demonstrate this a steel step-wedge was prepared with thicknesses ranging from 30 to 45 mm in steps of 5 mm. Such a thick solid steel sample results in strong attenuation and thus small signal. The same sample was also measured using standard thermal radiography for comparison. The normalised absorption profiles are shown in figure 4.42. The clearest and strongest signal is found at a neutron wavelength of 4.0 Å, just above the Bragg cut-off for iron. Energies below or above this range result in even less signal and consequently more noise. The thermal neutron result is also plotted. Although transmission is slightly higher the signal to noise ratio is worse.

The Bragg cut-off can also be exploited in another way. From cross-section curves like the ones in figure 4.39 it follows that for a defined material there exist pairs of energies for which the attenuation coefficient is the same. When dividing two images taken at these energies the contribution for this material cancels out, thus effectively making it transparent. A test sample

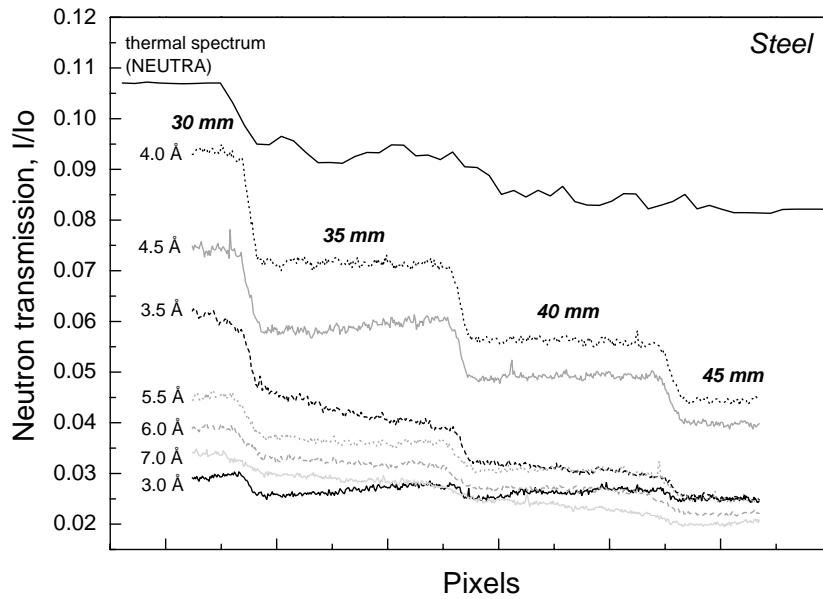


Figure 4.42: Normalised absorption profiles of a steel step wedge as function of energy

was prepared that contained a stack of 7 different materials, namely Teflon, Plexiglas, lead, steel, aluminum, iron and copper. This stack was imaged at different energies and the resulting images were divided two by two. Figure 4.43a) shows a regular radiograph of the stack taken at an energy of 3.0 Å. Fig. 4.43b), c) and d) show the division of the images taken at respectively 3.0 and 4.3 Å, 2.7 and 6.4 Å and finally 6.4 and 7.4 Å.

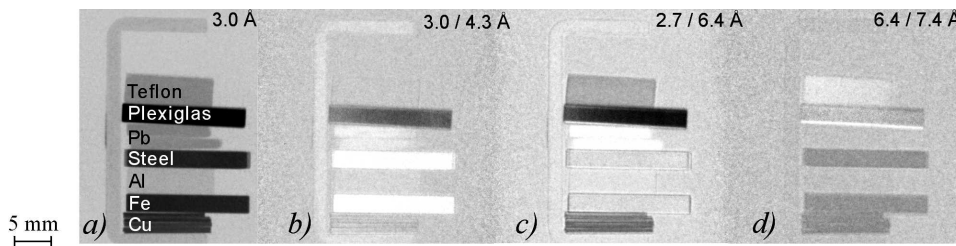


Figure 4.43: Dividing radiographs taken at different energies to make materials transparent.

A real world example of the possibilities of energy selective neutron radiography is the spark plug shown in figure 4.44. Figure 4.44 a) is a radiograph taken at 6.9 Å, b) was taken at 3.2 Å and c) is the result of the division of a) and b). The energies were chosen so that the steel of the spark plug was eliminated by the division. The resulting image clearly reveals inner

structure (in the centre of the image) that is invisible in either of the normal radiographs. Notice the edge effects. These are caused by the difference in beam divergence that occurs at different velocities of the selector as explained in 4.5.3.

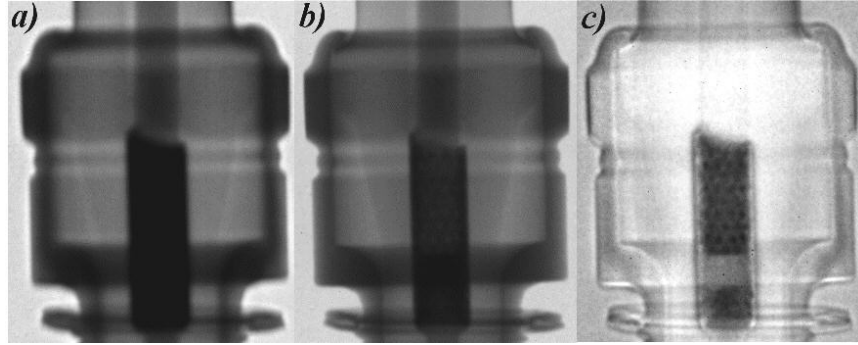


Figure 4.44: Energy selective investigation of a spark plug

Monochromatic Tomography

The advantages of energy selective neutron radiography are also valid for energy selective neutron tomography. Figure 4.45 illustrates the clearly better resolution of the monochromatic neutron tomography (right) as compared to that with a polychromatic beam (left and middle).

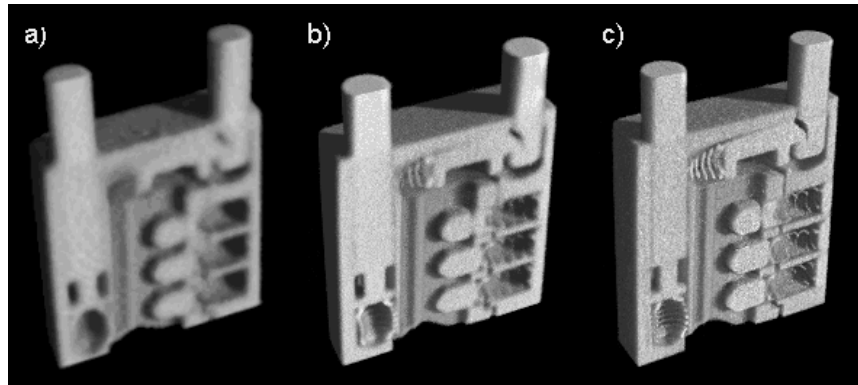


Figure 4.45: Tomography of a lock with a) white beam and the 420 μm screen b) white beam and 100 μm screen c) 2,7 \AA and 100 μm screen

4.5.5 Conclusion

A monochromatic beam offers clear advantages for neutron radiography and tomography. It was shown that it can provide better relative image contrast

and higher quality tomographic reconstructions. It can provide information that cannot be obtained using polychromatic beams. Finally it can be used in some cases for element identification. An obvious disadvantage of a monochromatic beam is the reduced neutron flux resulting in longer acquisition times. The results of these experiments were published in [\[90, 91\]](#).

4.6 Neutron Topography at TOPSI

4.6.1 Introduction

Topography is a technique to visualise the orientation of crystal planes inside a crystalline material. This technique was originally developed for X-rays and adapted for neutrons when sources with sufficiently high flux became available in the 70's [92, 93, 94]. The first neutron topography experiments were conducted by M. Ando and S. Hosoya in 1972 [95]. In recent years neutron topography has regained interest. New digital imaging methods allow new kinds of topography experiments [96, 97]. The basic idea is based on the Bragg law of diffraction. A sample is placed in a monochromatic and parallel beam. The camera looks at the sample under a chosen angle with respect to the incident monochromatic and parallel beam. If neutrons are recorded at a certain pixel position this means that somewhere along that ray a crystal plane in the sample is fulfilling the Bragg law. Topography uses large beam areas of several square centimetres. This allows to study complete samples in comparison to conventional point scanning methods using pencil beams.

Similar to classical tomography is the fact that along the line of sight the depth information is lost. Topo-tomography is then the logical extension to topography. This experiment was a feasibility study to assess the possibilities of neutron topo-tomography using a CCD/scintillator based camera system.

4.6.2 Two axis neutron diffractometer TOPSI

TOPSI is a θ - 2θ neutron diffractometer at SINQ. A non-focussing pyrolytic graphite monochromator extracts a monochromatic beam from the primary cold neutron beam. The energy can be chosen between 2 and 5 Å. The beam distribution is relatively homogeneous over about 4.0x4.0 cm². The transmitted beam size can be selected by three slit diaphragms, two before the sample position and one after. The θ -arm of the diffractometer is at a set angle to the primary beam and determines the energy of the incident monochromatic neutron beam. The 2θ -arm can be positioned between -125° and +130° with a precision of 0.002° using air cushions. The sample holder can be rotated from 0° to 360° (ω -rotation) with a precision of 0.002° and tilted between -20° and +20°. A ³He counting tube at the end of the 2θ -arm is used as a neutron detector to measure the neutron flux.

4.6.3 The setup

The experimental setup is shown in figure 4.46. The beam size was set at 2.5x3.0 cm². The camera is installed at the end of the 2θ -arm just in front of the ³He counting tube. The neutron flux is measured by this ³He counting

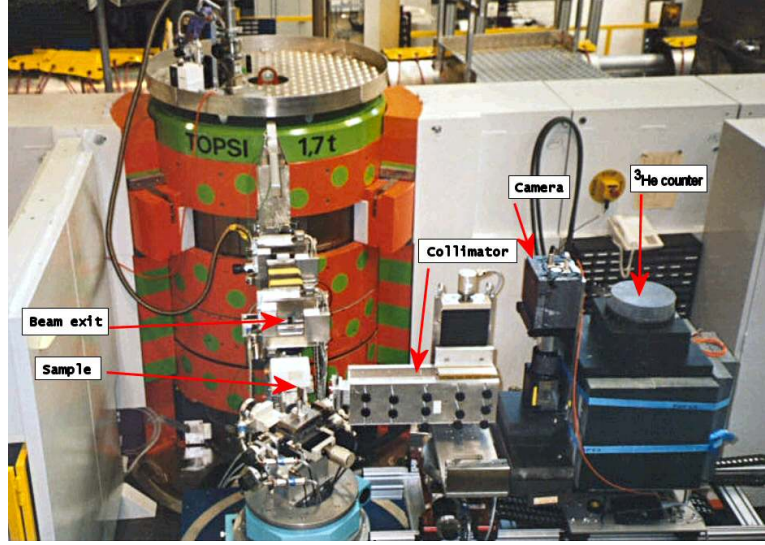


Figure 4.46: The setup at TOPSI

tube through the camera house in front of it. The CCD camera setup was basically the same as in the previous experiments. The field of view was approximately $3.6 \times 2.9 \text{ cm}^2$ giving a pixel resolution of about $29 \mu\text{m}$. The beam profile of the monochromatic beam before diffraction was measured first and is shown in figure 4.47 together with two line profiles taken horizontally and vertically through the centre. In a topography experiment it is essential to

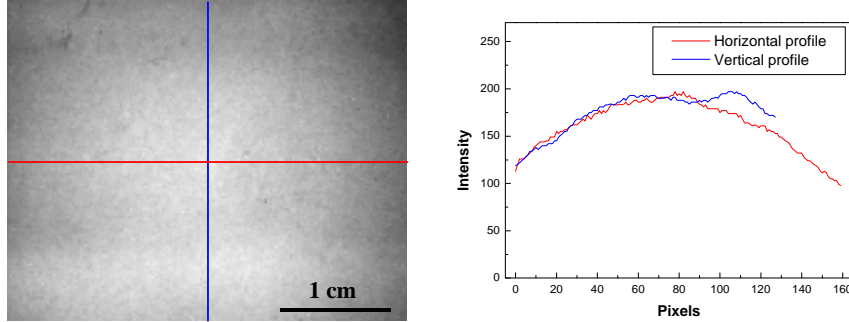


Figure 4.47: The beam profile at TOPSI

avoid radiation from different locations in the sample from overlapping on the detector. Therefore collimators have to be placed in front of it. These are Soller collimators as the one described in the previous chapter on the NCR experiments. A horizontal collimator with an angular acceptance of $20'$ was placed 15 cm in front of the scintillator screen. A vertical one with an acceptance of $15'$ was placed just next to it. The collimation determines both the spatial resolution in the sample and the angular resolution with

which the domain orientation is observed. The spatial resolution was calculated to be 2.3 mm in vertical direction and 3.1 mm in horizontal direction. The collimation setup is shown in figure 4.48. If the neutron beam is diffracted on two crystal domains with a disorientation of angle α it will show a divergence of α . From figure 4.49 it can be seen that the angular acceptance of the collimator limits the divergence of the neutron beam passing through it to the angle β . In this experiment the vertical angular resolution was $15'$ and the horizontal resolution $20'$.

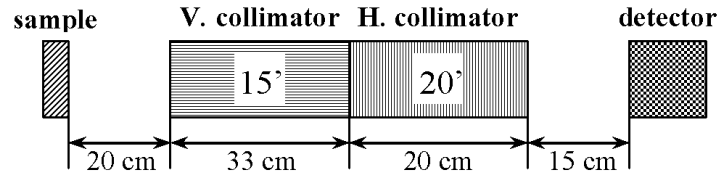


Figure 4.48: The collimator setup

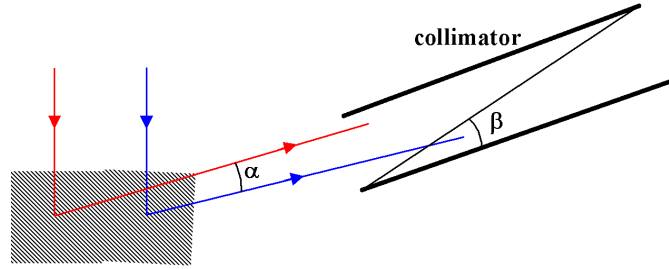


Figure 4.49: The angular resolution is determined by the collimation

Unlike most other experiments the detector system was not located inside a bunker but in the experimental hall, exposed to the ambient light. It was therefore critical to shield the system from stray light, given the long exposure times of several minutes. To verify this an exposure of 5 minutes was made without neutron beam. This showed no signal apart from the always present readout noise, and confirmed that the shielding was adequate. To protect the camera from scattered neutrons it was shielded with borated sheets. To avoid white spots in the image due to secondary gamma radiation an additional layer of lead shielding was placed around the camera.

The image acquisition

Normalisation of the recorded images is not possible using the standard methods. A beam profile cannot be recorded since there is no beam profile to normalise with without a sample to diffract the beam. It is also impossible to normalise for the beam intensity using an unobstructed region of the

beam since there cannot be a signal outside the sample area on the detector. Therefore a neutron monitor was installed in the monochromatic beam upstream from the sample. This gave a signal that was proportional to the incident neutron flux. This was connected to an analog input board in the acquisition PC.

The image acquisition was complicated much by two separate facts. First there turned out to be a large number of white spots in the images, despite the shielding with lead. This was due to the long exposures. Since a pixel loses all its information content when struck by a gamma ray this was clearly undesirable. In case of binning this is even more pronounced because pixels are combined in the camera hardware and so the fraction of pixels without useful signal increases even more. A solution was to divide the exposure time in smaller parts. This way the fraction of pixels per image that contained no information was reduced. The images were then combined to a final image after correction for the readout noise and spot filtering. The fact that readout noise now contributes a number of times instead of only once was verified to be less important. A typical single image and a resulting final image is shown in figure 4.50.

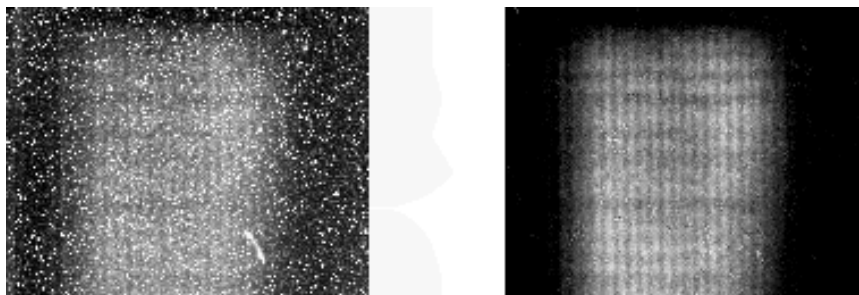


Figure 4.50: A single image (left) and the result from combined images (right)

Another reason was the fact that the TOPSI diffractometer control software was not linked to our image acquisition software. The scanning procedure of the diffractometer was such that it moved the arm to a given position, stayed there until a given number of neutrons had been recorded by the counter and then moved to the next position. This meant that the exposure time for the camera was not known (exactly) in advance, and since the control software does not allow the acquisition to be stopped without losing the image the same solution presented itself, namely dividing the exposure in a number of single exposures. The exposure time was set to about 1/10th of the expected total exposure time per position. When the signal from the counter indicated that the diffractometer was moving to the next position the acquisition was aborted, resulting in the loss of the last exposure. This way at least 90% of the available time was used, a good com-

promise between losing too much of the exposure time and accumulating too much readout noise.

4.6.4 Experiments

The experimental sequence for a single topography experiment was performed as follows:

- For each sample the angle 2θ was calculated for a Bragg reflection hkl with planar spacing d_{hkl} using the Bragg relation $2d_{hkl}\sin\theta = \lambda$ where θ is the reflection angle and λ the neutron wavelength.
- The 2θ arm of the diffractometer was set at the calculated 2θ value and a diffraction profile or so called 'rocking curve' was measured with the 3He detector rotating the sample through the angular interval $\omega=0...180^\circ$. Hereby the slit diaphragms were fully opened to a beam size of 2,5 by 3,0 cm² and no collimators were placed in the beam.
- Those angles where bright peaks were observed were stored and the sample was repositioned at one of those angles.
- If no peaks were found the sample was tilted at various angles and each time a new rocking curve was recorded ($\omega=0...180^\circ$) until a reflecting position was found.
- At the chosen reflection position the angles 2θ and ω were fine-tuned to maximize the signal in the 3He detector. Then the collimators were put into place by means of a motor system. These were rotated in fine steps around there initial position to obtain optimal alignment, again by maximizing the signal in the 3He detector.
- With the so adjusted setup, topography images were recorded using the CCD camera system.

Cu 220 monocrystal

A first possible application is quality control of monochromator crystals. A Cu220 monocrystal that serves as a monochromator crystal at the X-ray source at the linear accelerator in our research group was investigated. To verify the influence of the collimator on the angular resolving power the same crystal was scanned twice, once with Soller collimators and once without. The measurements were performed at a wavelength of 2 \AA and each topography image took 1 hour in total, measured in about 12 exposures of 5 minutes. Due to the lower flux the images with collimator show clearly worse statistics.

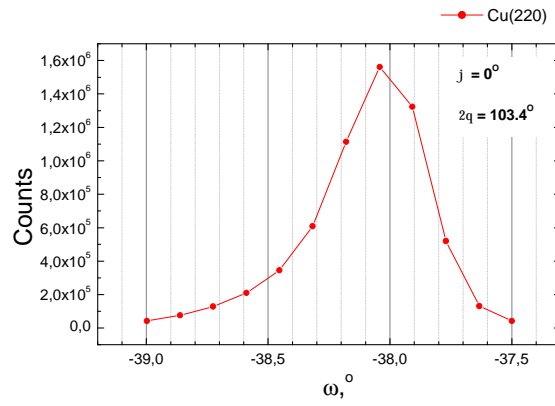


Figure 4.51: Diffractometer profile of a Cu 220 monocrystal

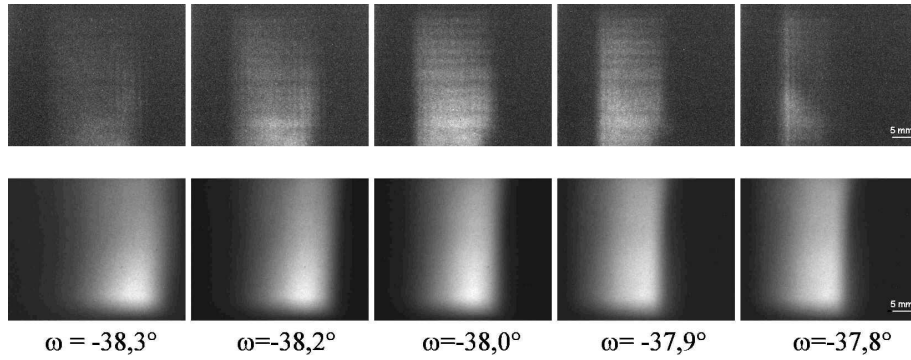


Figure 4.52: Topography images of a Cu220 monocrystal with (top) and without (bottom) Soller collimators

The measured diffractometer profile in figure 4.51 shows a clear reflection position around -38.0° . The topography images show good agreement with the diffractometer profile. The reflecting area is clearly better defined in the images with a collimator because the overlap of rays diffracted from

different regions in the crystal is eliminated. It is clear that this particular crystal shows a clear single orientation without obvious flaws, making it a good monochromator crystal.

MnSi polycrystal

A MnSi crystal (Fig. 4.53) was investigated to locate domains within the sample with a 111 orientation. The planar distance for this orientation is 2.63\AA . The chosen neutron wavelength was 2.44\AA and the corresponding 2θ angle was 55.2° . The diffractometer measurement revealed a strong



Figure 4.53: The MnSi crystal in its sample holder

reflection at $\omega=70.05^\circ$ as can be seen in figure 4.54a. The corresponding topography image in figure 4.54b shows a rather homogeneously reflecting domain within the crystal. When the sample was tilted over -5° the diffractometer profile looked essentially the same, as shown in figure 4.55a. The topography image 4.55b however shows a clearly different picture. This time the reflection seems to come from three more or less distinct areas in the sample. This distinction cannot be made from the diffractometer profiles alone. Finally an attempt was made to align the obtained topography images with a photograph of the sample. This is shown in figure 4.56.

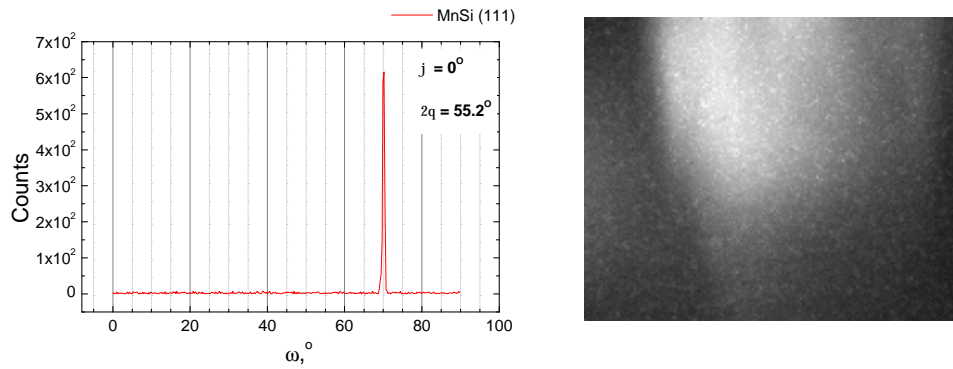


Figure 4.54: a) MnSi rocking curve at 0° b) MnSi topography image

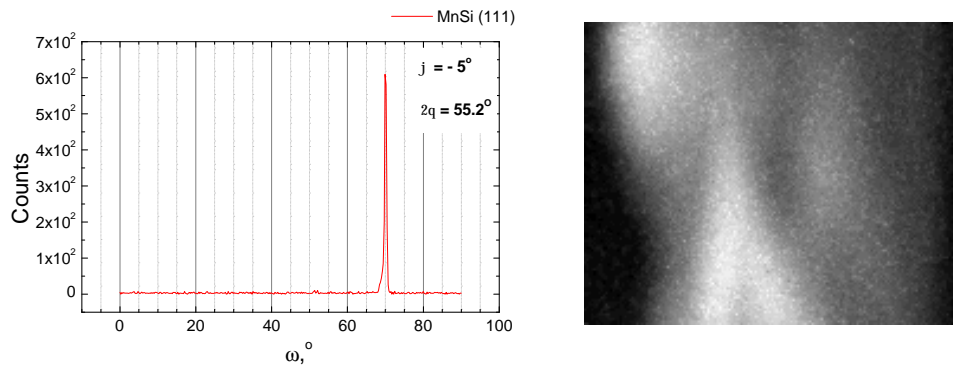


Figure 4.55: a) MnSi rocking curve at -5° b) MnSi topography image



Figure 4.56: Alignment of the topography images and a photograph of the sample.

4.6.5 Conclusion

These neutron topography experiments were the first to be performed at the SINQ facility at PSI. It was shown that topography is feasible under the given circumstances using a CCD/scintillator based camera system. It was shown that useful information can be obtained from real-life samples. The goal of performing topo-tomography was not obtained, but the feasibility was clearly proven. To achieve this a more sensitive camera system should be used. A higher dynamic range, a lower dark current (deeper cooling of the CCD), a more efficient scintillator or even additional components like image intensifiers may all contribute to reaching this goal. This will allow visualising crystal domain orientations in three dimensions, taking full benefit of the high penetrating power of neutrons. The results of these experiments were published in [98, 99].

4.7 Dynamic Tomography at ILL

4.7.1 Introduction

Dynamic radiography is a technique to visualise time-dependent phenomena by taking a series of radiographies of a fixed object. This requires high flux beams to ensure short exposure times. Neutrons are particularly suitable for dynamic radiography because of the high cross-section for hydrogen [100, 101]. This results in good contrast for water or organic fluids while being able to penetrate the bulk material relatively easy. It is commonly used to study for example fuel injection in engines. One particular application, the study of fluid flow in porous media, is of great importance to geology, archaeology, petrology, etc. [102]. It is also important for developing theoretical models [103, 104]. To study fluid flow many other techniques have been developed such as visual inspection or X-ray radiography. However, all these techniques are mainly limited to two dimensions. Visual inspection requires artificial circumstances to make the setup transparent for light, and X-ray inspection shows very little contrast due to the low cross section for fluids. Contrast agents are in most cases required to reveal the fluid. The need for better methods for visualizing fluid flow in porous media has been discussed in numerous articles [105, 106, 107] and dynamic neutron tomography provides a definite answer to this need.

This section describes the development and application of a high speed neutron tomography setup for studying transient fluid flows in porous media. The goal was to perform a complete tomography in less than a minute. This would allow the monitoring of dynamic phenomena that vary little on this time-scale in three dimensions. The setup was installed at the high flux Neutrograph beamline at the ILL in Grenoble (France). The first experiments were performed in April 2003 and an improved setup was used for a second run in October 2003. Possible applications include the study of transient flows in porous media, study of wood and its treatments, water uptake in building materials, fabrics, plant roots,...

4.7.2 The ILL Neutrograph beamline

A key factor in achieving a high speed setup is of course a high intensity neutron beam. The Neutrograph beamline at the ILL 58 MW research reactor (Grenoble, France) is one of the most intense neutron beams in the world. It delivers a thermal neutron flux of $2.9 \cdot 10^9$ n/cm²/s and a fast flux of $2 \cdot 10^7$ n/cm²/s. It has a mean L/D of about 120 and a useful beam area of 20x16 cm² making it ideally suited for high speed applications requiring average resolution. The experimental area is only about 3x2 m² making it quite difficult to work in. The walls are completely covered by 5 mm thick boron-carbide sheets to absorb scattered neutrons without causing activation. Before access to the bunker is possible, a big shutter inside the flighttube has

to close to block the neutrons. Because it takes several minutes to open or close this shutter a faster shutter was installed. This small shutter blocks only 99 % of the beam and is operated using air pressure so it can open and close within a second. It is used during the experiments to minimise the exposure of the inside of the bunker to the full neutron intensity. Still the activation poses a problem, especially the slowly decaying part. After every irradiation one has to wait for half an hour up to several hours, depending on the number and duration of previous runs. This requires careful planning of each experiment.

4.7.3 The setup

The setup is shown schematically in figure 4.57. The neutron beam arrives from the right. To control the fluid supply to the samples a remotely controlled proportional valve (a) was connected to a reservoir holding the fluid under study and was placed beside the sample. The fluid was guided through a thin aluminium pipe to a position near or above the sample where it could be released as needed. The proportional valve allowed for excellent control over the flow rate and volume. The valve was regulated using an analog output board. The motor stage (b) was placed as close as possible to the scintillator to minimize geometric blurring due to the relatively high divergence of the beam (see section 4.7.5). Depending on the size of the sample the rotational axis was between 3 and 5 cm away from the scintillator. The samples had to be placed in a dish to hold the fluid. Consequently this dish is present in all radiographies. Therefore the dish was made from aluminium to make it virtually invisible.

Because this beamline is situated at a flighttube it looks directly at the reactor core resulting in a significant portion of gamma radiation in the beam. Though the scintillator (c) is rather insensitive to these gamma rays they can scatter at the mirror (d) or other parts of the setup. Therefore the lightpath is bent over 180 degrees using two mirrors to avoid gamma radiation hitting the CCD (e) directly thus causing bright spots. To collect the maximum amount of light from the scintillator the light path was kept as short as possible and a fast 50mm/f1.4 Nikkor lens was used at maximum aperture. Everything was placed inside a light-tight box to avoid spurious exposure of the CCD. About 20 cm of lead was placed around and above the camera to shield it from gamma radiation. Exposed surfaces were covered with boron sheets to avoid activation by scattered neutrons.

4.7.4 Optimisation of the setup

The global speed of a tomography setup is determined by several factors. First there is of course the beam intensity which is available. Secondly there is the efficiency of the scintillator, the optics and geometry of the setup. The

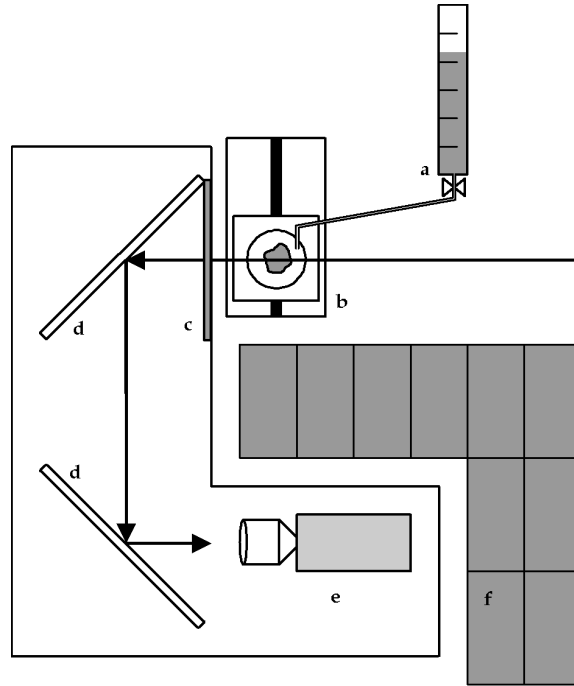


Figure 4.57: The setup for dynamic tomography at the ILL

existing setup was already optimized by using an efficient scintillator that is well matched to the camera's spectral sensitivity, by keeping the light-path short and by using a fast lens. Then there are hardware issues like readout time of the camera, speed of the motors and hard-disk speed. Little optimization is possible here. Finally there is the software that controls and synchronizes the different components. To achieve the high frame rates that were needed everything was implemented in a single programming environment, namely LabVIEW. This includes the camera control and readout, the motors and their limit switches, the valve control and the beam shutter control.

The existing motor controller proved to be the most important drawback. It was controlled with a serial communication protocol that was slow and did not offer much flexibility. With a response time of the order of 3 seconds a single tomography of 100 projections would take at least 5 minutes. Instead of using a new hardware controller it was decided to control the motors directly from Labview using an analog output board. This gave excellent flexibility and control over speed, torque, acceleration etc. and resulted in the possibility to drive the motor twice as fast as before without losing steps. More importantly the response time between giving the command and the actual start of the movement was reduced drastically to a few ms. The actual development of the motor controller is described in appendix A.

Optimizing the acquisition software was the next step towards the highest possible framerate. The camera control and readout was improved by directly embedding the low-level routines available from PCO's software development kit. This resulted in a faster readout and less overhead. The motor controller was also embedded in the software. Finally the sequence of steps in recording a tomography was addressed. Each projection is basically composed of three steps. First there is the exposure part, then readout of the image and writing it to hard-disk and finally moving the motor to the next projection angle. Normally these steps are executed in sequence. By putting the camera and motor control in two independent threads they can be executed simultaneously. Directly after exposure the readout starts and at the same time the motor starts moving. This reduces the time per projection by the smaller of the two contributions.

The final result was a setup that records a complete tomography of 100 projections (320x240 pixels) in just less than 10 seconds. This comes down to 100 ms per projection. Exposure takes 10 ms (see next paragraph). Camera readout and writing to hard disk each take about 9 ms. But this does not contribute to the total time because it is done while moving the motor which takes about 85 ms. Most of this 85 ms is acceleration and deceleration due to torque limitations of the motor. From this it is clear that the motors are still the limiting factor. Finally we observed that real time display on the computer screen reduced performance. The software was therefore adapted to minimize all windows during acquisition.

4.7.5 Beam characteristics

The two experimental runs had different setups. The first time our own PCO Sensicam SVGA camera having 1240x1024 pixels was used with a lightpath of 39 cm resulting in a field of view of 85x65 mm². The second time the experiments were done with the setup of the Neutrograph beamline. The only differences were the camera, a PCO Sensicam VGA with 640x480 pixels, and a longer lightpath of 65 cm resulting in a field of view of 120x90 mm² and a pixel size of 250 μ m. The characteristics described here refer to the second setup since it was the most advanced in terms of speed, the most relevant parameter in these experiments.

The beam profile was smooth and flat within a few percent over an area of 20x16 cm². From earlier experience we knew that the extremely high flux at the Neutrograph facility causes the scintillators to degrade more rapidly. This is clearly shown in figure 4.58 showing two beam profile images. The first was recorded before the first experiments while the last was recorded just before the last tomography. The exposure time needed to fill the entire dynamic range of the camera in binning 2x2 was measured to be 8 ms at the beginning of the experiments. During the experiments the scintillator efficiency decreased as a result of the enormous flux. Overall the light out-

put decreased by about 30% after 5 days of experiments. As a result the exposure time had to be increased to about 11 ms. More importantly the

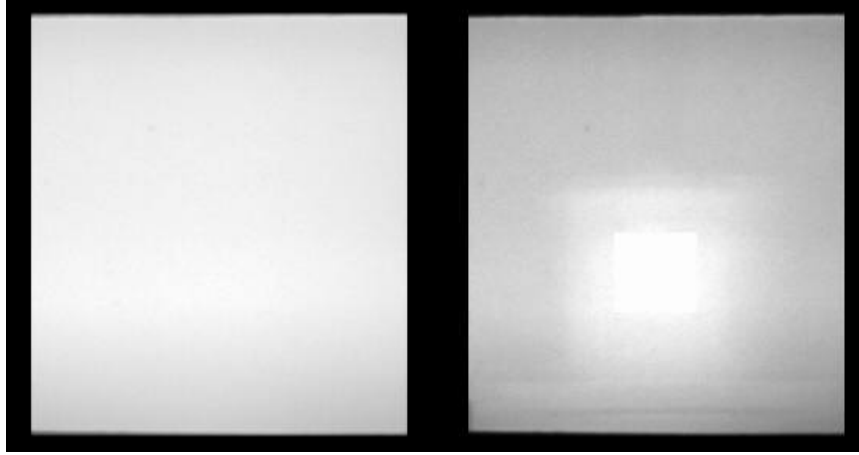


Figure 4.58: The recorded beam profile at the start (left) and end (right) of the experiments

area that was covered by the samples during the experiments showed a lower drop in light yield due to the lower exposure to neutrons. This caused the recorded beam profile to show inhomogeneities of the order of 20 %. It was therefore essential to record beam profile images regularly in order to have a good normalization. Visual inspection of the scintillator screen later showed a clear discoloration. We suspect that the epoxy base of the scintillator becomes brown due to the radiation.

The resolution was measured as usual using a thin Cadmium edge placed at 4 cm of the scintillator, on the rotational axis. The resulting 10%-90% resolution was 6 unbinned pixels or 1.5 mm. This means that the images can be binned 2x2 times to 320x240 pixels without significant loss of resolution. Since as a rule of thumb the number of projections should be about half of the number of pixels we opted for 100 projections per tomography.

4.7.6 Experiments

Initial tests

First some initial test were performed to assess what samples were suitable for tomographic imaging of fluid absorption. The first sample (B13) was a sandstone with a high porosity of 23,8%. Absorption of the water happened at a rate which proved too high to be considered for further tomographic investigation. The next sample (B173) had a much lower porosity of 4,6%. This time no absorption was recorded. Subsequent visual inspection however showed that some water had been absorbed in the stone. Therefore the

experiment was repeated with another sample of the same nature (B177) but this time using Boron as a contrast agent dissolved in the water. Now the absorption inside the stone could be observed. At this point it was clear which samples would be suitable for dynamic tomography and which ones would be limited to radiographic investigation.

A second initial test was based on the so called Karstenpipe test, a standard procedure for assessing the water absorbing properties of stones [108]. A glass tube with defined dimensions is placed on the side face of the stone using a sticky sealant. It is filled with water and the amount of water absorbed between the fifth and tenth minute is a measure for the absorptivity of the stone. This setup simulates the circumstances of falling rain on the stone surface. Figure 4.59 shows six frames from the radiography movie that was recorded. Although the absorptivity of this particular sample was too high to fit the requirements of the Karstenpipe procedure this initial test proved that neutron imaging can yield valuable additional information. Not only the amount of water that penetrates the stone can be measured, but also the way it penetrates (fingered flow or homogeneous) and the penetration depth as function of time.

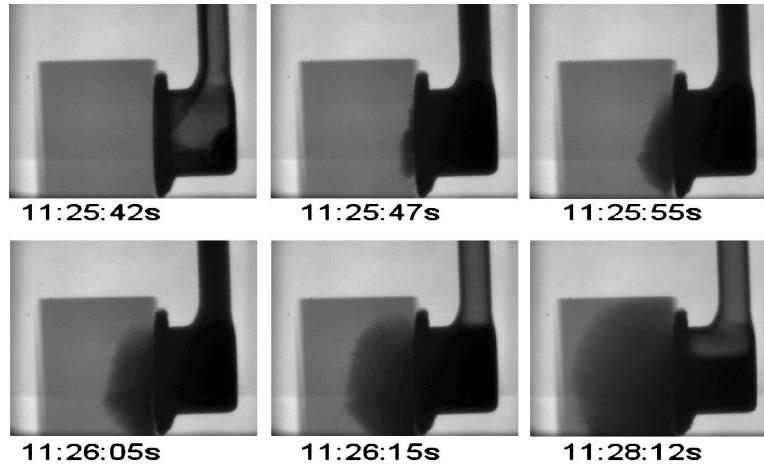


Figure 4.59: Dynamic radiography of the Karstenpipe standard test

Water uptake in Ytong, a porous building material

Ytong is a highly porous building material made of autoclaved aerated concrete. A sample was prepared of about $1 \times 1 \times 4 \text{ cm}^3$. Water was released on the bottom of the dish and a tomography recording was started. Figure 4.60 shows the resulting 3D reconstructions at different time intervals after the initial release of water. A closer study of the reconstructed slices makes it clear that the water rises along the outside edges first. It penetrates to the bulk of the stone much later. This conclusion could not be drawn from the

radiographic images. This immediately shows the possible value of tomography versus classical radiography for dynamic phenomena. This result is to our knowledge the first ever 3D dynamic neutron tomography.

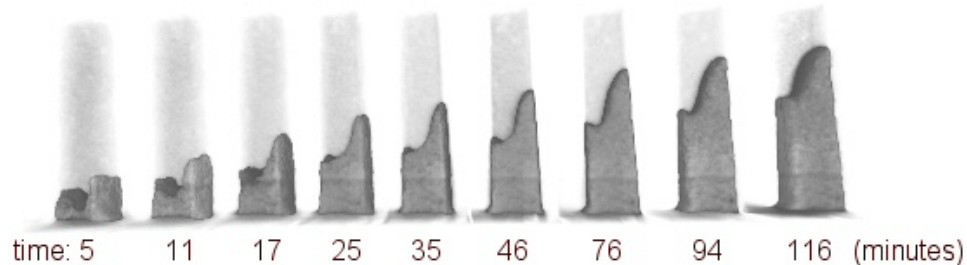


Figure 4.60: 3D rendering of water uptake in a porous building material

Water transport in naturally layered rock

A naturally layered rock was studied next. From visual inspection it was known to consist of two layers. The face between the two layers was standing upright. Water was released on the top surface and was quickly absorbed in one of the two layers. The fluid front could be followed throughout the volume. At a certain point in time the fluid front hardly moved any more. At that point some more water was added. This secondary front quickly propagated through the already wetted part.

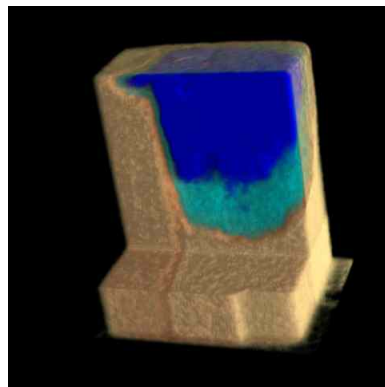


Figure 4.61: Water penetrating a layered natural rock

Figure 4.61 shows a cut through the 3D reconstructed volume showing clearly the two distinct stone layers. The one on the right is clearly more absorbing than the layer on the left. The secondary fluid front (dark blue) can be discriminated from the first (light blue).

The penetration of petrol in a porous limestone

The absorption of petrol fuel in a porous limestone was studied to illustrate the possible applications for petrology. The oil industry spends millions on research on the porosity of rocks. This results in valuable information on the potential oil yield of a given soil or rock bed. The sample was a $4 \times 4 \times 4$ cm³ cube of limestone of Maastricht, a homogeneous and soft porous rock. A small amount of petrol was released on top of the cube and monitored as it penetrated the rock. Figure 4.62 shows a typical radiography of the object under study. It is clear that the stone is easily penetrated and that

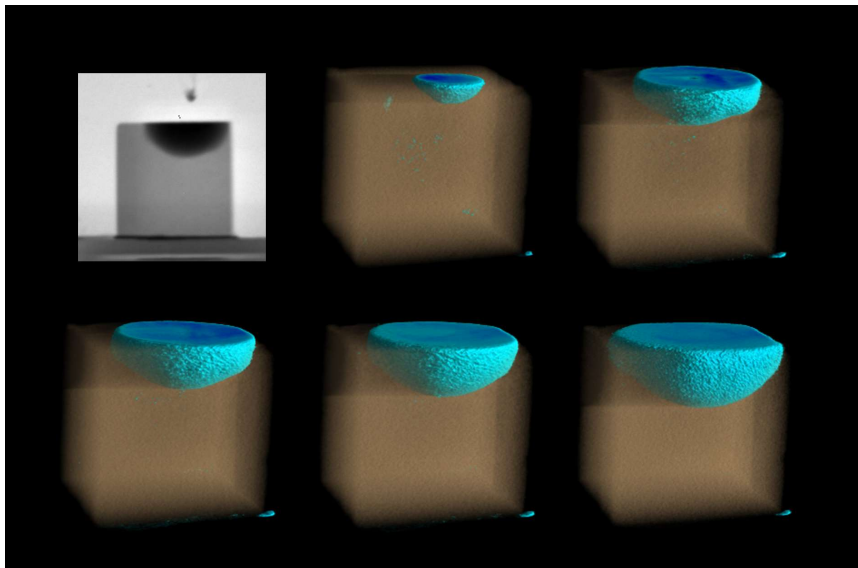


Figure 4.62: Fuel spreading in a porous rock as seen with neutrons

the fluid blocks a large fraction of the neutrons. Also shown are some of the resulting 3D reconstructions at different points in time. The stone itself is rendered semi-transparent to show the fluid as it penetrates the bulk of the sample. The colour gradient indicates higher densities towards darker blue. The fluid can easily be discerned. Figure 4.62 shows a single radiography (top left) clearly revealing the fluid in the stone. The top centre figure shows the reconstruction recorded between 10 and 20 seconds after the release of a single drop of fluid. Then more fluid was released and the reconstruction of the absorbed fluid between 10 and 20 seconds after this second release is shown top right. The bottom series shows the situation 1, 2 and 3 minutes later. This particular sample shows a very spherical and distinct flow front. Based on these 3D reconstructions the speed of the flow front can be measured at different locations in the sample. The flow front itself can be extracted as a surface.

The treatment of porous building materials

As a more complex sample we show a sandstone of Bray, a commonly used building material in many European historical monuments. Much research is done on treatments to protect these against the negative influences of water. Consolidants are applied to reinforce brittle surfaces. Hydrophobic agents are used to prevent water penetrating the stone. In this particular sample the stone is treated with hydrofuge. Goal of this experiment was to try and see if the product could be detected with tomography, to measure how deep it penetrates the stone and finally to evaluate its hydrophobic properties. For practical reasons the application of the product had to be performed outside the bunker. By the time the sample had been positioned on the motor stage, the door of the bunker had been closed and the shutter had opened at least 3 minutes had passed. As expected the product could clearly be observed in the stone. At this point it remained uncertain whether the product would still be visible after the solvent had evaporated. The solvent was a mixture of ethanol and methanol. Because of its high hydrogen content it is expected to contribute significantly to the recorded signal. After drying for 24 hours the sample was again scanned. The product could be identified

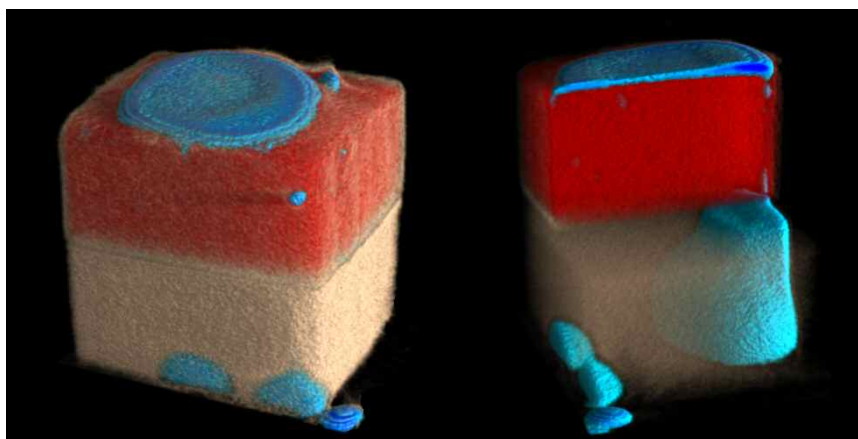


Figure 4.63: Water spreading in porous sandstone treated with hydrofuge

in the stone (Figure 4.63). Next water was released on the top surface where the hydrophobic behaviour became clearly apparent since the water now formed a big droplet instead of being absorbed. More water was added until it spilt over the side. Figure 4.63 shows the result after 40 seconds. In this rather complicated 3D reconstruction a cut was made in the top half of the volume. The stone itself is rendered almost transparent. The hydrofuge (red) penetrated almost half of the stone i.e. 2 cm deep. The water (blue) can be seen lying on the top surface without penetrating the treated part of the stone. Some of this water spilt over the sides and fell to the bottom, mostly on the right side where it is being absorbed in the untreated part of

the stone and rises up to the treated part of the stone. This illustrates a common problem with such treatments. Water that gets trapped behind the treated layer will expand when freezing, causing the treated layer to break off.

The same product was applied to a limestone of Maastricht with a porosity of 52%. A similar procedure as described above was followed. The reconstructions shown in figure 4.64 show that the product did not penetrate quite as fast and deep as with the previous sample. Similar experiments were repeated on samples with different porosities and using different types of agents. No detailed analysis of those samples will be presented because this is beyond the scope of this work which is to develop the technique itself.

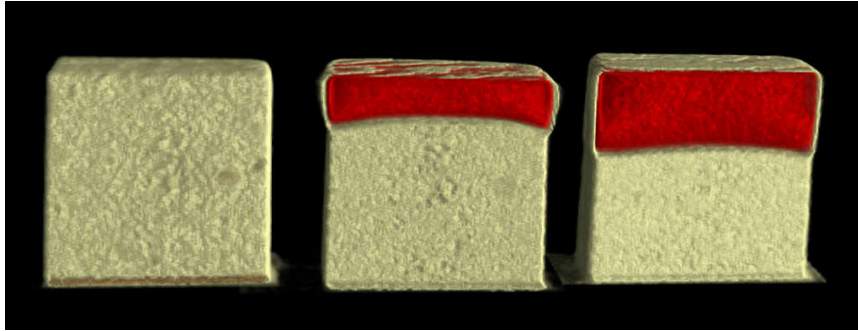


Figure 4.64: Hydrofuge agent penetrating a porous limestone

Study of motion artefacts in dynamic tomography

The quality of a dynamic tomography depends on the speed of the acquisition relative to the rate of changes to be monitored. Ideally the changes in the scanned volume should be smaller than one voxel in the course of a complete scan of 180 degrees. Faster changes will result in artefacts in the reconstructions. To evaluate such artefacts a specific experiment was set up. An artificial sample was prepared by drilling a fine hole with a 2 mm diameter in a piece of Ytong. This sample was positioned on the motor stage with the hole on the top. A scan was started and water was released on the top face of the sample.

Figure 4.65 shows three projections from this scan. The first projection was taken at 60 degrees, the second at 120 degrees and the third image shows the last projection at 180 degrees. Clearly the changes in the sample during this single scan were larger than one pixel. When we consider the slice indicated by the horizontal red line (slice 280) we see that no water is present in the first projection, but there is water present in the second and third projection. This is also evident in the corresponding sinogram which is

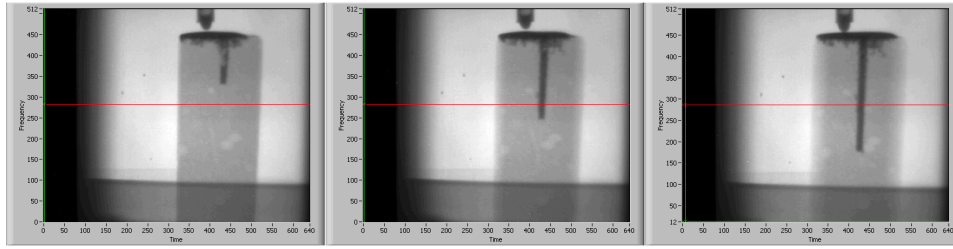


Figure 4.65: Projections showing clear motion during the acquisition

shown in figure 4.66. Note that the vertical axis shows the first projections

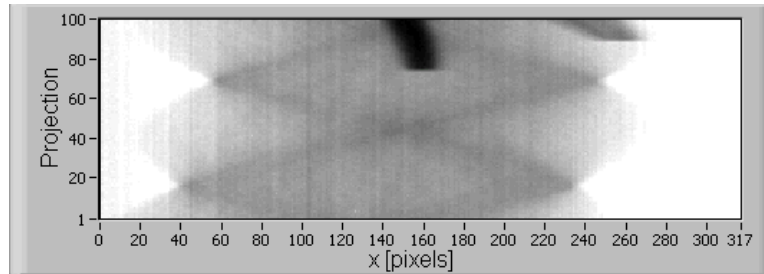


Figure 4.66: Resulting sinogram showing the transition

at the bottom. An abrupt change occurs around projection number 75, the moment at which the moving fluid front passes the slice under consideration. The resulting reconstruction is shown in 4.67. A typical X-shaped artefact is the result. This is caused by the strong signal from the water which contributes to the reconstruction only over the limited angular range where it was present. It should be noted that this is an extreme and artificial case. Real life situations will be less obvious, yet we learned from experience that these artefacts are very recognizable. This type of artefact cannot be corrected.

4.7.7 Outlook

It was already mentioned that the motor stage is still the limiting factor. A new motor system is under development that allows recording of a complete tomography under the same conditions in less than 3 seconds. This will bring many more dynamic processes within reach, and will reduce the artefacts due to the movement of the fluid front during the acquisition. The way to achieve this is to step away from the classic sequential recording of a tomography namely taking the acquisition and moving the motor alternately. In the new configuration the motor rotates continuously and the acquisition is done while rotating. This way there is no more acceleration/deceleration slowing down the motor. As an additional advantage the motion is much

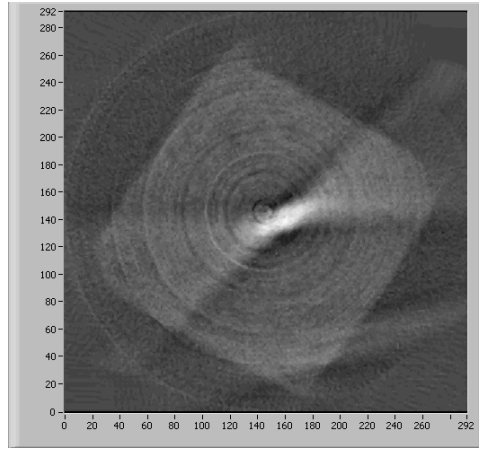


Figure 4.67: Resulting reconstruction showing typical artefact.

smoother reducing the possible unwanted influence of the repeated deceleration/acceleration as seen in a classical sequence. As long as the exposure time remains small compared to the time between exposures, or in other words as long as the angular change during a single exposure is small compared to the angular step between two projections the resulting artefacts are negligible.

4.7.8 Conclusion

These experiments are to our knowledge the first dynamic tomography experiments with neutrons ever performed. The feasibility of the technique was proven. Some clear advantages over the existing 2D techniques have been demonstrated, as well as possible applications and improvements. A particularly interesting application is the study of fluid flows in porous media as was clearly demonstrated. Preprocessing, reconstructing and visualising the high number of tomographies required the development of specially adapted routines to do much of the work automatically. The results have been published in [109] and [110]. Other experiments will follow, increasing the acquisition rate further and extending the range of applications.

Chapter 5

CONCLUSION and OUTLOOK

5.1 Conclusion

The experimental setup

In the course of this work acquisition and control software was developed to handle all the practical aspects of a variety of tomography experiments. This includes the camera control and readout, the motor control, and control and monitoring of peripherals such as beam monitors, counters, triggers and shutters. Many aspects were developed specifically for individual experiments performed during this research, such as special acquisition sequences for time dependent applications or statistical procedures for extreme low light applications. A software based stepper motor controller was developed to enable faster and much more flexible motor control. This proved crucial in a series of experiments for high speed tomography. Finally everything was successfully integrated into a single user interface. The result proved to be a highly flexible and adaptable tool that served at a number of beamlines under very different conditions.

The reconstruction software

For the actual reconstruction of the acquired data the Octopus reconstruction software was developed. In the course of this work it evolved from a set of basic routines to a full featured package for tomographic research. It includes routines for data preprocessing, for the actual reconstruction and for image postprocessing. The effect of each processing step on the end result was investigated. A number of algorithms were developed to optimize the speed and quality of the reconstruction. A server client structure was implemented to allow the reconstructions to be distributed over a network. In this way multiple computers can assist with the reconstruction, reduc-

ing the calculation time drastically. The reconstruction of a tomographic dataset is a time consuming and often repetitive task. Therefore a full automatic reconstruction mode was implemented. This proved indispensable for the time dependent experiments where tens of tomographies were recorded for each sample. The software can handle datasets for all common beam geometries, making it applicable in other domains than neutron tomography too. Additionally an extensive image viewer was written for detailed analysis of the data. Octopus was, and will continue to be, a key element in our tomography research, both in X-ray and neutron applications.

Experimental results

Our first neutron tomography experiments took place at the PGA beamline at PSI. The main goal was to become familiar with the technique, with its possibilities and its limitations. We characterized the setup in detail and used it to explore new possible applications, scientific and/or industrial. As a next step improvements were made in terms of spatial resolution by applying thinner scintillators, neutron collimators and a combination of both. Similar experiments were repeated at another beamline at PSI called NCR. Back at the PGA beamline our experimental expertise was broadened with the installation of a neutron lens in an attempt to further improve the spatial resolution by magnifying the recorded shadow image. Although not entirely successful the approach proved to have potential but needs further technological developments.

Then we turned our attention from the spatial domain to the energy domain. An experiment was set up based on a neutron velocity selector, a device to extract a relatively monochromatic neutron beam from an incoming polychromatic beam. This way we could exploit the energy dependence of the neutron attenuation to retrieve more information from the samples. Although the acquisition times are subsequently longer, clear advantages for neutron radiography and tomography were demonstrated. Using both artificial and real-life samples it was shown that mono-energetic neutron imaging can provide better relative image contrast and higher quality tomographic reconstructions. It can provide information that cannot be obtained using polychromatic beams. It also offers the additional advantage of an increased spatial resolution. Finally it can be used in some particular cases for element identification by matching the recorded energy dependence of the neutron attenuation to tabulated data.

A second experiment that was situated in the energy domain was neutron topography at the TOPSI diffractometer at PSI. Topography, originally an X-ray technique, is a technique using monochromatic beams to visualise the orientation of crystal domains. The extremely low neutron flux made this experiment a real challenge. Special measures were taken concerning the acquisition setup and procedure to cope with the long exposure times.

It was shown that it is possible to retrieve 3D crystal plane orientations from real-life samples using neutrons. The orientation of crystal domains was successfully visualised in a number of different crystals. The goal of extending the experiment to topo-tomography was not obtained, due to the long exposure times, but the feasibility was clearly proven. Future developments will allow visualising crystal domain orientations in three dimensions, taking full benefit of the high penetrating power of neutrons, compared to the X-ray based topography techniques.

In a final series of experiments we addressed the time domain. Most research done in the field of time dependent neutron imaging focusses on high speed radiography. Tomography of time dependent phenomena had, to our knowledge, not been attempted yet. A setup was designed specifically for high speed applications. This setup was successfully installed at the high flux Neutrograph beamline at ILL. A full 180 degree tomographic scan could be realised in less than 10 seconds. This made it possible to monitor for example the distribution of fluids propagating in bulk materials in 3D. These experiments are to our knowledge the first dynamic tomography experiments with neutrons ever performed. The feasibility of the technique was proven. Some clear advantages over the existing 2D techniques have been demonstrated, as well as possible applications and improvements. We demonstrated for example how treatments of building materials against water penetration can be evaluated for their effectiveness, and how fuel or water penetrate porous rocks. In addition some specially adapted routines were developed for preprocessing, reconstructing and visualising the high amounts of data that come with such experiments. Without these routines 3D dynamic tomography experiments would not have been practically possible.

5.2 Outlook

5.2.1 Improvements of the setup

The tomography setup can be improved in a number of ways. We will continue to evaluate new neutron scintillators for spatial resolution and light yield as they appear on the market. We are also considering a replacement for the CCD camera. The current camera is six years old and has suffered from the numerous hours in high level radiation environments. It served not only at neutron beams but also at numerous X-ray and gamma-ray setups. As a result a number of dead pixels and even complete dead columns have appeared. A new camera like for example the PCO1600 from PCO, in many ways a successor to the camera used in this work, will offer many advantages and will open up new possibilities. A much shorter minimal exposure time would enable high speed experiments to study for example running engines. On the other side the maximum exposure time of several days combined with

a reduced dark current would enable even more extreme low-light experiments. This could make the topo-tomography experiments possible within reasonable acquisition times. The higher dynamic range would result in better tomographic reconstructions due to the better statistics. Finally such a camera offers the possibility of a large on-board memory. This way complete tomographies can be recorded in the camera's own memory at very high speed. After the acquisition the data can then be transferred at a slower rate to the PC's memory or hard-disk. In high-speed applications this could result in higher throughput. For dynamic tomography this would result in less motion-artefacts.

Another development that was already mentioned earlier is the flat panel detector. This emerging new type of detector has some clear advantages and will become in our opinion a very important type of detector in the near future, given the enormous interest from the medical radiology world in digital radiography. The main advantage is the high efficiency due to the direct coupling of the scintillator to the detector. There are two leading technologies, amorphous silicon and CMOS based flat panels. Both are indirect conversion panels that use scintillators to convert the radiation to visible light. We already performed tests with a CMOS type flat panel, a Shad-o-Box 4K from Rad-icon Imaging Corp. [111] at an X-ray source. To serve as a neutron detector however these detectors have to be fitted with neutron sensitive scintillators, which sometimes poses problems. This is one option we will try to explore in collaboration with other research groups and the manufacturers of such systems.

5.2.2 Software development

The development of the software will also continue, with the main focus on the reconstruction routines since this remains the most time-consuming part. The current algorithms will be further improved and optimized. The client program is currently being modified to enable the distributed processing of other calculations besides the actual reconstruction. We are currently looking into the implementation of filtered backprojection algorithms that can reduce the calculation complexity from $O(N^3)$ to $N^2 \log(N)$. There exist a number of such algorithms [78, 79, 80] and we will evaluate which is suited best for implementation and integration into the existing software. We are also developing algorithms for so called limited angle tomography. In particular cases it is not possible to rotate the sample over a full 180 degrees. This results in an incomplete dataset, causing artefacts when reconstructed. For adequate reconstruction of such data iterative algebraic methods are required.

Furthermore we will include another important scanning geometry called helical scanning. It was explained that the Feldkamp method for cone beam geometry is an approximate method. This approximation is caused by the

scanning geometry which does not sample the complete frequency space, resulting in reconstruction artefacts. The most common solution to this problem is the so called helical scanning geometry. To achieve this the sample is not only rotated during the acquisition, but also translated vertically. For a detailed explanation and derivation of the formulas we refer to [76]. We also plan an extensive study of algorithms for correcting a number of second order errors in tomographic data such as beam hardening effects, metal artefacts, scattering artefacts, deconvolution of blurry images... Each of these effects has its own particular causes and implications, and can be very detrimental for the reconstruction quality. The beam hardening correction is already in an advanced stage of development and is already included in Octopus. The others require further research.

5.2.3 Further experiments

The experiments on dynamic tomography will be further developed. The technique is now ready for routine measurements. Currently an improved setup is under development that will take the time for recording a single tomography further down to less than 3 seconds. To achieve this the synchronised sequence of rotation-exposure-rotation... will be abandoned. Instead the sample will rotate continuously at a constant speed and the camera will be externally triggered at regular intervals. This has the additional advantage that the sample no longer experiences repeated acceleration and deceleration, resulting in much smoother motion. As a result the dynamics that are observed are less likely to be compromised by the acquisition procedure. We are currently evaluating the effects of the rotation of the sample during the actual exposure of each projection. Under the circumstances at the Neutrograph beamline the exposure time using the improved setup will be of the order of 5 milliseconds. During this interval the sample will rotate over $\frac{180.5 \cdot 10^{-3}}{3}$ or roughly a quarter of a degree. This is small compared to the 1.8 degree angular interval between successive projections. It is therefore expected not to pose problems. A detailed criterion to assess this problem is under study. This new setup will enable true 3D monitoring of a broader range of fluid flow processes.

We also intend to participate in experiments at the new PGA facility at the FRM-II reactor in Munich (Germany). The original setup at PSI was dismantled and transported to Munich. There it is currently being rebuilt [112, 113]. The flux will be about 10^9 n/s/cm² or eight times higher than at SINQ. Also the beam area will be more than 5 times larger at 5 cm x 11.5 cm. The facility will be commissioned hopefully next year.

5.2.4 Other tomography experiments

Besides our neutron tomography activities we will also continue the X-ray based research at our own laboratory. There will be two main paths of development. The first will be the development of a gamma-ray tomography setup at the linear accelerator. This setup will use high energy X-rays (1 MeV mean energy) for the study of large and/or high density objects (up to at least 30 cm of rock or 10 cm of steel). The production of these X-rays will occur in a specially developed Bremsstrahlung target made from Tungsten, combined with filters to eliminate lower energy contributions. The high energy radiation offers the added advantage that almost no beam hardening occurs because of the relative independence of the attenuation on the energy. The problem of Compton-scattering however, the dominant process at these energies, will need further investigation based on Monte-Carlo simulations.

The second main path of development will be the construction of a multifunctional high-resolution X-ray tomography facility that will achieve sub-micron resolution. This facility will meet the ever increasing demand, both from within the university as from outside, for non-destructive high resolution imaging. The X-ray beam will feature a smallest spot size of less than 1 μm resulting in a detail detectability of the order of 300 nm. The range of applications is huge. There is already interest from micro-electronics, medicine, biology, geology, material physics, space technology etc. This facility will be unique in Belgium. We opted for a modular construction for maximum flexibility and applicability. The setup will be able to handle samples ranging from 0,5 mm diameter up to 20 cm, depending on the density and energy used.

The integration of the high energy tomography beamline and the high resolution tomography setup will provide a non-destructive X-ray imaging facility covering the widest possible range of sample sizes and resolutions available with current technology. More information can be found on <http://ssf.ugent.be/linac/>.

Appendix A

Stepper Motor Controller

A.1 Introduction

One of the key elements in a tomography setup is the rotation stage to rotate the sample. To achieve accurate positioning one normally applies stepper motors with a high number of primary steps. Most stepper motor systems are composed of a digital controller, a driver (amplifier) and the motor itself. Digital pulses are sent to the controller and translated to voltage levels that are in turn amplified and sent to the motor's windings. The controllers and amplifiers available for our experiments were custom built by the electronic workshop of the University of Fribourg. The controllers received commands from the PC through a serial port connector and these commands were then processed by software that was stored in EPROM chips.

There were a few problems with this approach. First of all it was slow. One cycle of sending a command, executing the motion and receiving confirmation took about 4 seconds. For high speed experiments like dynamical tomography this is orders of magnitude too slow. Secondly there was only limited control over parameters such as speed, acceleration and step resolution. Finally the EPROM chips started to fail due to the deterioration of the chips. EPROMs have a typical lifetime of 7-10 years in good conditions. High radiation environments like an accelerator bunker caused failure even sooner.

So a new motor controller system was required. The motors were present, the amplifiers were present, all that was needed was a controller to control the amplifiers. Some research quickly showed that the custom built system could not be fitted with an industry standard controller because of the particular way the amplifiers were wired to the motors. Therefore a radical approach was taken by deciding to generate the voltages for the motor windings directly from LabVIEW using an analog output board, eliminating the need for a separate controller. This would give us excellent control over the motors and allow for the best integration within the existing software.

A.2 Stepper Motor Theory

There are too many different types and configurations of stepper motors to describe in detail. We will therefore limit the description to those types relevant for our setup. Stepper motors are based on attraction and repulsion of magnetic poles. Most types have a rotor with permanent magnets on their axis and a stator consisting of coils. When energized with electric current these create a magnetic field causing the rotor to rotate.

The first distinction to make is unipolar or bipolar control. Unipolar control has only one positive power supply. There are two subsets of coils inside the motor with opposite windings to be able to create both senses of magnetisation. Bipolar control has a positive and negative power supply allowing both polarisations from one set of coils. This reduces the number of connections to make to the outside world at the cost of a more complex and expensive power supply. The motors used in our experiments are bipolar.

The second distinction is the operation mode. The most commonly used switching sequence is full step mode. The sequence for bipolar control is shown in table A.1. To double the number of steps one can use the half step mode. In full step mode both sets of coils are energised at the same time and the rotor holds halfway between two main steps. In half step mode one of both coils is not energised, causing the rotor to hold at a main step. The sequence for bipolar control is shown in table A.2. Advantages of half step mode are smoother motion and twice as many possible positions. A more advanced control sequence is microstepping. Here the sets of coils are not energized at full power but only fractionally in such a way that the rotor balances at a certain position between two main steps. Simply put, when one set is energized for 10% and the other for 90% the rotor will hold at 10% from the first main step. In reality there is no linear relationship between current and angle but rather a sinusoidal relationship as can be seen in figure A.2. This way the number of steps can be increased by a factor of ten or more.

| STEP | 1 | 2 | 3 | 4 | 1 |
|--------|---|---|---|---|---|
| PHASE0 | + | + | - | - | + |
| PHASE1 | + | - | - | + | + |

Table A.1: Full step sequence

| STEP | 1 | 2 | 3 | 4 | 5 | 6 | 7 | 8 | 1 |
|--------|---|---|---|---|---|---|---|---|---|
| PHASE0 | + | + | + | 0 | - | - | - | 0 | + |
| PHASE1 | + | 0 | - | - | - | 0 | + | + | + |

Table A.2: Half step sequence

A.3 Wiring

The controller runs on a PC in the LabVIEW environment and controls an analog output board. Two analog output channels carry the voltages for the two phases of the motor to the input of the amplifier. The amplifier converts these signal level voltages into power level voltages. These are connected with heavy wiring to the motor. The wiring of the motor is quite particular since only three wires connect the amplifier and the motor. Standard bipolar setups have four. In this case the two coils share a common connection to ground (0 V).

Linear motor stages often have limit switches to prevent hitting the edges of the shaft in case of a wrong command. This can be implemented in many different ways. In this case two switches, one at each end, are wired in series with a 100 k resistor each. One side is tied to +5V and the other to ground. The signal is taken between the two switches and read with one analog input signal. The switches are normally closed types, opening when hit. It follows then that during normal operation the 5V is divided equally over both 100k resistors, returning a voltage of 2.5V to the analog input channel. When either of the switches opens the voltage gets tied to the side that stays closed, returning a voltage of 5V or 0V. When this occurs all operations are halted within 5 ms.

A.4 Labview Implementation

The code consists of two main parts, a control loop executing the user commands, and a so called watchdog loop to check the limit switches during motion. The subroutine seen exactly in the centre of the control loop is the core program. It calculates the voltage sequence that has to be put on the motor coils to execute a certain motion. The parameters for this are the current position (phase), the step mode (halfstep, microstepping), the ramp length (slow start in case of heavy loads), the amplitude of the signal and finally of course the number of steps to move. This results in a sequence like the one shown in figure A.2. Notice the slower start and stop to avoid missing steps due to inertia. Also notice the last sample of the sequence. This is the pair of voltages that remains on the coils after motion has finished, because unlike main step mode, microstepping requires a permanent current through the windings to hold position. The hold voltages can be reduced as compared to voltages during motion. This is important to avoid excessive heating of the motor. The requirement is that they keep the same ratio and thus the same angular position between main steps. This is controlled with a parameter, called hold value, and is implemented to avoid excessive heating of the motor.

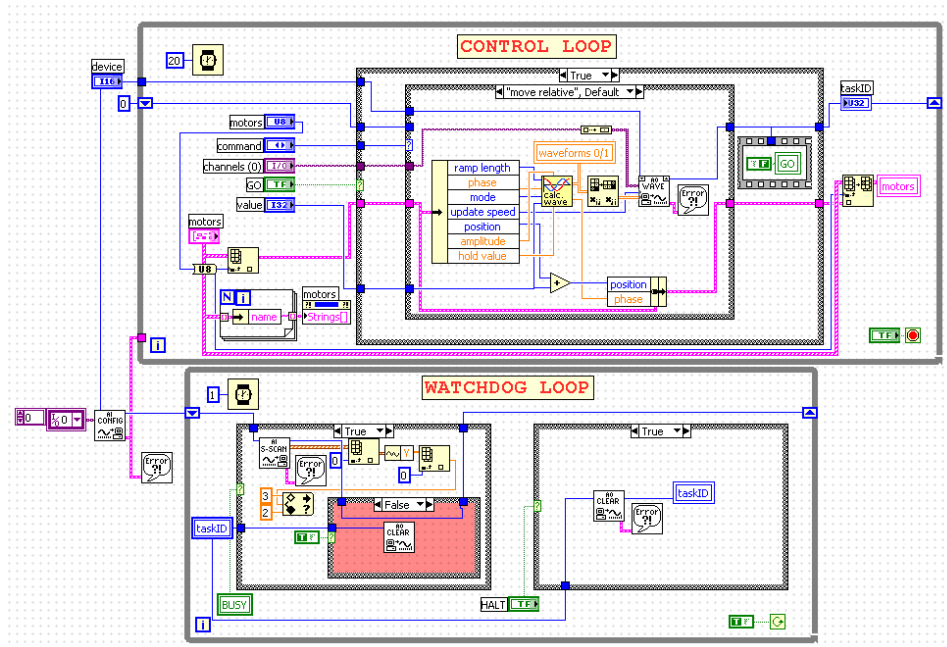


Figure A.1: The stepper controller code

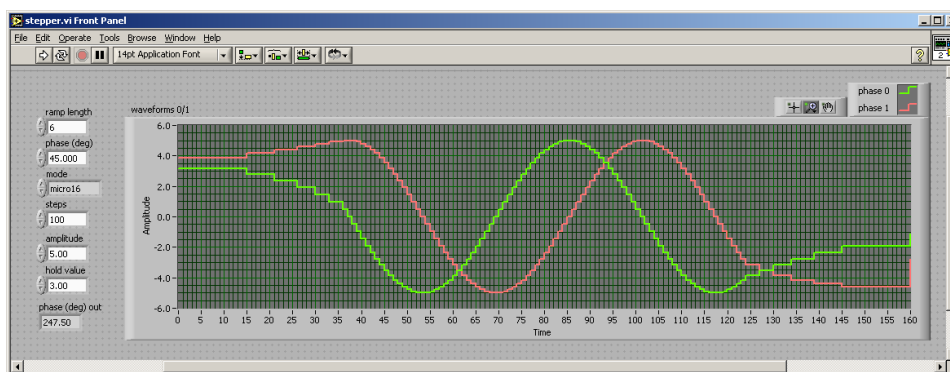


Figure A.2: The output of the core routine

A.5 Conclusion

This stepper motor controller really showed its value in the dynamical tomography experiments at the ILL. We succeeded in doing a complete tomography of 100 projections in less than 10 seconds, or less than 100 ms per projection. The exposure typically took 10 ms. Readout took about 9 ms while saving the image took 11 ms. This leaves just 85 ms for the motor part. Most of this time is due to limited acceleration/deceleration of the motor. Together with the LabVIEW based camera control routines, the tomography setup is now completely running in one single programming environment, from data acquisition and hardware control to data processing and visualisation. This yields excellent flexibility given the ever changing requirements of different setups and beamlines.

Appendix B

CCD camera characterisation

B.1 Basic concepts

Charge Coupled Devices (CCDs) were invented in October 19, 1969, by William S. Boyle and George E. Smith at Bell Telephone Laboratories [43]. Charge Coupled Devices (CCDs) are silicon-based integrated circuits consisting of a dense matrix of photodiodes. When photons interact with the photosensitive area of the silicon, electron-hole pairs are created through the photo-electric effect. The CCD chip is structured in such a way that the freed charges remain trapped inside potential walls that define the individual photosites or pixels. After the exposure the accumulated charges are transferred across the chip through parallel shift registers (columns) and transferred through a serial shift register (row) to a low noise pre-amplifier. The amplified signal is then digitised by a single ADC. This way a digital image file is generated that can be transferred to a computer. Different CCD architectures and charge transfer schemes exist. For an extensive overview of CCD technology we refer to [114] or [115]. A brief overview of the most important concepts in CCD technology follows below:

- **Full well capacity** : each pixel is defined by potential barriers resulting in a potential well. This well or bucket can only hold a given number of electrons before overflowing. This number is called the full well capacity. When the pixel is overexposed electrons can cross the potential barriers and leak into neighbouring pixels, resulting mostly in bright streaks along a single direction, an effect called blooming or bleeding. Scientific cameras are equipped with special technologies to reduce blooming. The camera used in this thesis has an anti-blooming factor of 1000, meaning that blooming only occurs after a pixel has been overexposed by a factor of 1000. As a result blooming has never posed a problem in the experiments for this thesis.
- **Dynamic range versus bit depth** : the dynamic range of a CCD is defined as the maximum signal divided by the camera noise, where

the maximum signal is determined by the full well capacity, and noise is the sum of all noise contributions (see further), both expressed in number of electrons. Most often dynamic range is expressed in dB according to the following equation :

$$DynamicRange = 20.log \frac{N_{full}}{N_{noise}} \quad (B.1)$$

A full well depth of for example 25000 electrons and a read noise of 8 electrons results in a dynamic range of 3125 or 69 dB. Dynamic range is closely related to and often confused with the bit depth of a CCD camera. The bit depth used by the ADC defines the number of discrete digital values that are generated to represent the analog charge signal. To digitise a dynamic range of 3125 adequately an ADC with a bit depth of at least 12 bit or 4096 greylevels is required. Choosing the bit depth too low will result in image information loss. Making it too high will result in a higher price and a slower digitisation without added information.

- **Linearity** : One of the great advantages of a CCD based detection system is its excellent linearity. Ideally the output signal should be exactly linear with exposure time (under ideal exposure conditions, i.e. constant photon flux). In reality there is some deviation of this linearity, especially near full exposure. The linearity (or non-linearity) is calculated using a linear least-squares fit to the data. The maximum deviations of the data relative to the fit, in positive and negative sense (ΔP and ΔN) are used to define the linearity as:

$$Linearity[\%] = \frac{\Delta P + \Delta N}{MAXSIGNAL}.100 \quad (B.2)$$

When carefully corrected for the different noise contributions the camera used in this thesis achieves non-linearities below 1%. Using lookup tables, values of less then 0.1% can be achieved.

- **Noise** : The three main noise contributions in CCD cameras are:
 - **Photon noise** n_{photon} : recording an image using a CCD camera is a counting process. In such cases the end result has an uncertainty that follows a Poisson distribution. In the case of the camera used in this thesis 1 greylevel or analog-digital unit (ADU) corresponds to approximately five photons. As a result the photon noise n_{photon} equals the standard deviation on a greylevel of 4000 which is equal to $\frac{\sqrt{5 \cdot 4000}}{5}$ or roughly 28 greylevels.
 - **Dark current noise** n_{dark} : thermally generated electrons contribute to the final signal. This is called dark current and is proportional to the exposure time. This current is highly dependent

on the temperature of the chip (roughly doubling every 10 °C). Therefore CCD chips are often cooled using Peltier elements or in extreme cases liquid nitrogen. The camera used in this thesis has a dark current of less than 0.02 greylevels per second which is almost never of significance.

- **Readout noise** $n_{readout}$: The readout noise is that part of the noise contribution from the electronics that is time-independent. It mainly originates in the preamplifier just before the ADC. The camera used in this thesis has a readout noise of slightly more than 1 greylevel and this is therefore of no importance.

Because these noise contributions are not correlated, the total number of noise electrons is given by:

$$n_{total} = \sqrt{n_{photon}^2 + n_{dark}^2 + n_{readout}^2} \quad (B.3)$$

From this then follows another important concept, the signal to noise ratio which is defined as:

$$\frac{S}{N} = \frac{n_{signal}}{n_{noise}} = \frac{n_{photon}^2}{\sqrt{n_{photon}^2 + n_{dark}^2 + n_{readout}^2}} \quad (B.4)$$

The maximum signal to noise ratio is found when the pixel is exposed up to the full well capacity and is equal to the dynamic range.

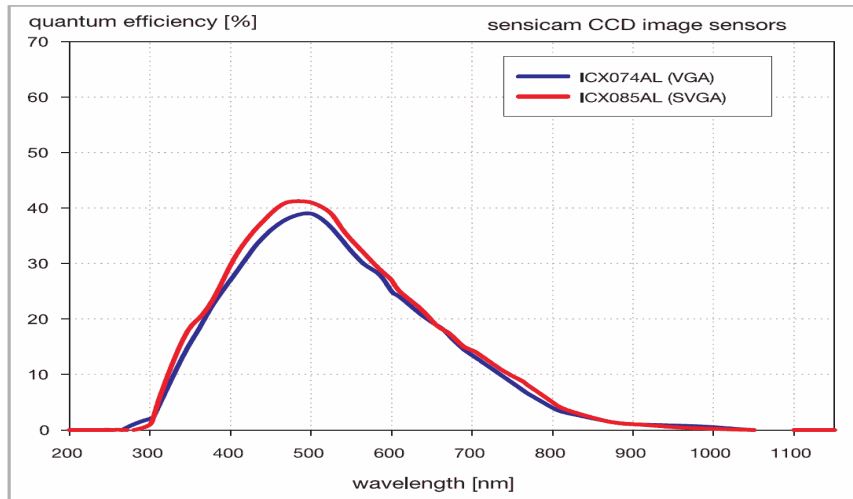
- **Binning** : Pixel binning is a charge transfer scheme that combines the charge collected by several adjacent CCD pixels before transferring it to the ADC. This way the number of pixels is reduced, the sensitivity is increased and the noise is reduced resulting in an improved signal-to-noise ratio and a higher frame rate.
- **Fill factor** : The fill factor of a CCD is the fraction of pixel area that is sensitive to light. Depending on the type of CCD this can range between 40 and 100%. CCD architectures that have low fill factor often use micro-lens arrays to increase the effective fill factor. Each pixel has a small lens at its surface that redirects the incoming light onto the photo-sensitive area of that pixel.
- **Quantum efficiency** : The quantum efficiency of a CCD is defined as the number of electron-hole pairs created and successfully readout by the device for each incoming photon. It depends on the wavelength of the incoming photon, the CCD architecture and on the fill factor of the CCD chip.

B.2 Characteristics of the PCO Sensicam LE SVGA

B.2.1 Main Features

- make : PCO Computer Optics GmbH (<http://www.pco.de>)
- model : Sensicam Long Exposure (LE)
- CCD architecture : Interline CCD with microlens array on chip
- 12bit digitisation, 67 dB dynamic range
- high resolution (1280 x 1024 pixel, SVGA)
- long exposure times from 1ms - 1000s
- low noise, down to 7e- rms
- 8 frames per second at full CCD resolution (SVGA)
- thermo-electrical cooling (Peltier) down to -12°C
- dimensions : 205 x 93 x 77 mm (LxWxH)

B.2.2 Quantum Efficiency



B.2.3 Technical Data

| SensiCam | VGA | SVGA | SensiCam QE |
|--|--|--------------------|---|
| Sensor Type | CCD-Interline Progressive Scan with "lens-on-chip" | | |
| Number of Pixels | 640(H) x 480(V) | 1280(H) x 1024(V) | 1376(H) x 1040(V) |
| Pixel Size | 9.9µm x 9.9µm | 6.7µm x 6.7µm | 6.45µm x 6.45µm |
| Sensor Format | 1/2" | 2/3" | 2/3" |
| Scan Area | 6.3mm x 4.8mm | 8.6mm x 6.9mm | 8.9mm x 6.7mm |
| Cooling Type | 2-stage peltier cooler with forced air cooling | | |
| CCD Temperature | -15°C | -12°C | -12°C |
| Full Well Capacity | 35.000 e- | 25.000 e- | 18.000 e- |
| Scan Rate | 12.5 MHz | 12.5 MHz | 16 MHz |
| Readout Noise @12.5 MHz | 13 ... 14 e- | 7 ... 8 e- | 4 ... 5 e- (Gain High) 5 ... 6 e- (Gain Low) |
| A/D-Converter | 12 Bit @12.5MHz | | |
| A/D Conversion Factor | 7.5 e-/count | 5 e-/count | 2 e-/count (Gain High) 4 e-/count (Gain Low) |
| Max. Quantum Efficiency monochrome, @ 520nm | > 40% | | > 60% |
| Spectral Response (monochrome) | 280 ... 1000nm | | |
| Spectral Response (color) | RGB primary colors | | not available |
| Average Dark Charge ⁷⁾ | < 0.1 e-/pixel.sec | < 0.1 e-/pixel.sec | < 0.1 e-/pixel.sec |
| Extinction Ratio ¹⁾ | 1:2000 1:2000 | 1:2000 | |
| Smear ²⁾ | < 0.005% | < 0.005% | < 0.005% |
| Anti Blooming ³⁾ | > 1000 | > 1000 | max. 100 |
| CCD Quality | grade 0 | grade 0 | grade 0 |
| Non-Linearity | < 1% | < 1% | < 1% |
| Readout Frequency (Full Frame) | 30 fps | 8 fps | 10 fps |
| Binning Horizontal | 1...8 | | 1...8 |
| Binning Vertical | 1...32 | | 1...16 |
| Blemishes | | | |
| Point Defects ⁴⁾ | 0 0 | 0 | |
| Cluster Defects ⁵⁾ | 0 0 | 0 | |
| Column Defects ⁶⁾ | 0 0 | 0 | |
| Warm Pixels ⁷⁾ typ. | | | |
| # pixels > 100 e- | 0 0 | 0 | |
| # pixels > 5 e- | 0 - 2 | 0 - 2 | 0 - 2 |
| # pixels > 1 e- | 250 - 1000 | 500 - 2000 | 500 - 2000 |
| Non-Uniformity in darkness ⁸⁾ typ. | 1 count | 1 count | 1 count |
| Non-Uniformity in brightness ⁹⁾ typ. | 0.2% | 0.6% | 0.6% |
| # pixels > 12% | 0 | 0 | 0 |
| # pixels 8 ... 12% | 0 | 0 - 2 | 0 - 2 |
| # pixels 4 ... 8% | 0 | 10 - 50 | 10 - 50 |
| # pixels 2 ... 4% | 0 - 5 | n.a. | n.a. |
| Optical Input | C-Mount with adjustable focus length | | |
| Dimension | Head: 93(W) x 78(H) x 210(L) mm | | |
| Weight | 1.6 kg | | |
| Operating Temperature | 0...40°C | | |
| Storage Temperature | -20...+70°C | | |
| Humidity | 10...90% non condensing | | |
| C-Mount Back Focal Length | 17.92 mm | | |
| Maximum lens screw-in depth | 9.5mm (with optional filter glass: 6mm) | | |

Appendix C

Optics

C.1 Optimal lens coupling

The imaging system used in this thesis is a lens coupled system. The scintillator is imaged on the CCD chip using a single lens. There exist also tandem designs, using two lenses. Although more light efficient such systems are impractical in the experimental situations encountered in this work. Therefore only the single lens design using one objective will be considered here. In most cases the image size is fixed (the size of the CCD-chip) and the object size is given (the size of the scintillator one wants to image). The question is how to design the most effective setup in terms of light efficiency. To find the best combination of objective and position of the camera the following considerations apply:

Let us call the size of the field of view S , the chip size C , the object distance OD and the image distance ID , as shown in figure C.1. The thin lens equation then fixes the relation between the object distance, the image distance and the focal length of the objective:

$$\frac{1}{f} = \frac{1}{OD} + \frac{1}{ID} \quad (C.1)$$

From this it follows that:

$$\frac{1}{ID} = \frac{1}{f} - \frac{1}{OD} \quad (C.2)$$

The field of view S and the chip size C are related as follows:

$$\frac{S}{OD} = \frac{C}{ID} = 2.\tan(\alpha) \quad (C.3)$$

Suppose we want to image a given scintillator with size S onto the chip. The aim is to collect the maximum amount of light possible. The previous equation can be rearranged as follows:

$$S = 2.\tan(\alpha).OD = C.\frac{OD}{ID} = C.OD.\left(\frac{1}{f} - \frac{1}{OD}\right) = C.\left(\frac{OD}{f} - 1\right) \quad (C.4)$$

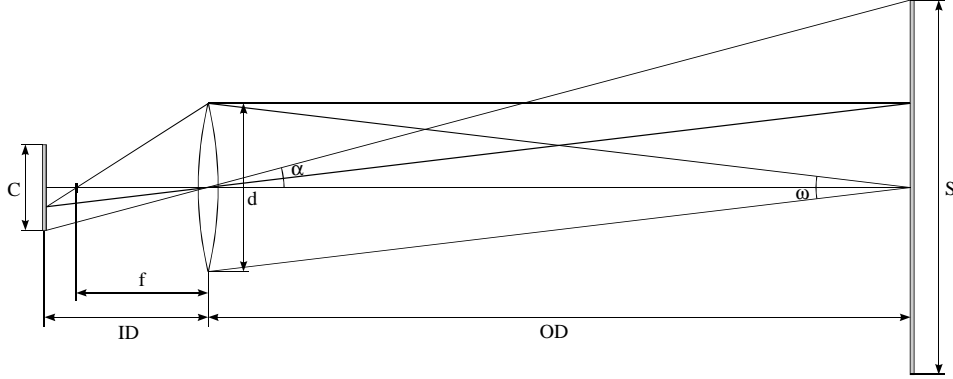


Figure C.1: Optimal lens coupling

In this expression $(\frac{OD}{f} - 1)$ represents the reduction factor. This implies that the field of view is defined by solely the ratio $\frac{OD}{f}$, meaning that we can use an objective with long focal distance placed further away, or one with a shorter focal distance placed closer by the scintillator. The efficiency of the design is determined by the fraction of light emitted by the scintillator that eventually reaches the CCD chip. This fraction is defined by the solid angle subtended by the lens as seen from a point on the scintillator. This solid angle is calculated as follows:

$$\omega = \frac{A_{lens}}{4\pi OD^2} \quad (C.5)$$

The surface area A_{lens} of the objective is defined by what is commonly called the 'speed' of the lens, or its f-stop value $f/\#$, which is defined as the ratio between the focal distance and the diameter of the objective:

$$f/\# = f/d \quad (C.6)$$

with d the diameter of the objective. From this it follows that:

$$d = \frac{f}{f/\#} \quad (C.7)$$

As a result the solid angle becomes:

$$\omega = \frac{A_{lens}}{4\pi OD^2} = \frac{1}{4\pi OD^2} \frac{\pi d^2}{4} = \frac{1}{16\pi OD^2} \left(\frac{f}{f/\#} \right)^2 \quad (C.8)$$

Because the ratio $\frac{f}{OD}$ is fixed for a given field of view this result is only dependent on the f-stop value $f/\#$. Lenses with relatively short focal distances (up to 50 mm) can be made with $f/\#$ of 1.2 or even lower (lower means larger diameters). For larger focal distances this becomes increasingly difficult and inconvenient because of the physical dimensions (a 200

mm lens with a speed of 1.0 would require a front element with a diameter of 200 mm, which is impossible). The conclusion is that the optimal lens coupling is done by using the fastest possible lens, which will inevitably be one with a relatively short focal distance and thus will be placed relatively close to the scintillator. The final design can of course also depend on other parameters such as physical limitations of the setup.

Appendix D

Nederlandse samenvatting

Titel : Tomografische beeldvormingstechnieken gebruik makende van koude en thermische neutronen

Het onderwerp van dit doctoraatsonderzoek is neutronentomografie. Deze relatief nieuwe techniek voor niet-destructieve beeldvorming maakt gebruik van het doordringend vermogen van neutronen om het inwendige van objecten te bestuderen en te visualiseren. Het basisprincipe van tomografie is dat de inwendige structuur van een object kan berekend worden op basis van een reeks twee-dimensionele projecties (genaamd radiografieën). Deze worden opgenomen vanuit verschillende hoeken, door draaiing van het object om een vaste as, met een vorm van doordringende straling. De meest gekende vorm van tomografie is de medische CT of computer-tomografie. Deze gebruikt X-stralen om de interne weefsels en organen van een patiënt te onderzoeken. In tegenstelling tot medische CT gaat dit doctoraatsonderzoek over het gebruik van neutronen als probe voor tomografie. De te onderzoeken objecten zijn geen levende organismen, maar samples met een wetenschappelijk of industrieel belang. Zoals gezegd is neutronentomografie als techniek relatief nieuw en het hoofddoel van het hier beschreven onderzoek is dan ook in de eerste plaats: **de ontwikkeling van deze techniek, het verkennen en uitbreiden van de mogelijke toepassingen en het ontwikkelen van de nodige instrumentatie (zowel software als hardware) om dit mogelijk te maken.**

Context van dit onderzoek

X-stralentomografie

Dit doctoraatsonderzoek werd verricht binnen de onderzoeksgroep Stralingsfysica van de vakgroep Subatomaire en Stralingsfysica van de Universiteit Gent. Tomografie is reeds 7 jaar lang één van de onderzoeksthema's binnen de groep. Oorspronkelijk werd alle onderzoek rond tomografie uitgevoerd aan de 15 MeV lineaire elektronenversneller van de vakgroep. Deze machine produceert hoge intensiteit elektronenbundels met een energie die continu variabel is tussen 2 en 15 MeV. Een gedetailleerde beschrijving van de machine is te vinden in [1]. En van de vier bundellijnen die voorhanden zijn voor het onderzoek produceert een monochromatische X-stralenbundel met een energie die continu variabel is tussen ruwweg 50 en 140 keV. Deze werd ontwikkeld in samenwerking met de Nuclear Physics onderzoeksgroep PAN van de Universiteit van Fribourg (Zwitserland), toen onder leiding van Prof. J. Jolie die het originele concept had geformuleerd. Het is aan deze bundellijn dat de eerste beeldvormingsexpertise binnen de groep werd verworven. Met deze bundel was het namelijk mogelijk om aan element-gevoelige X-stralentomografie te doen. Vanwege de lage bundelintensiteit was deze opstelling echter beperkt tot het scannen van een 2D laagje. Dezelfde techniek werd verder ontwikkeld in een reeks experimenten aan het ESRF synchrotron in Grenoble (Frankrijk) waar de veel hogere X-stralenintensiteit volwaardige 3D element-gevoelige tomografie mogelijk maakte.

Neutronentomografie

Een ander onderzoeksgebied van de onderzoeksgroep uit Fribourg was Prompt Gamma Activation (PGA), een techniek voor identificatie van elementen in samples door middel van koude neutronen. Deze opstelling bevond zich aan het Paul Scherrer Instituut (PSI) in Villigen (Zwitserland). De neutronenbundel die gebruikt werd voor dit onderzoek had enkele bijzondere karakteristieken die het mogelijk maakten om aan tomografie te doen, met name een hoge neutronenflux en een homogene intensiteitsverdeling over een voldoende grote oppervlakte. De samenwerking met de universiteit van Fribourg werd dan ook verder uitgebreid en een reeks experimenten rond tomografie met koude neutronen werd opgezet.

Radiografie en tomografie met neutronen biedt interessante perspectieven voor niet-destructief onderzoek (NDT). De sterk verschillende eigenschappen van neutronen als doordringende probe in vergelijking met X-stralen maakt nieuwe toepassingen mogelijk. Zo zijn neutronen bijzonder gevoelig voor water of andere waterstofrijke stoffen zoals organische materialen, solventen, oliën, vetten... Anderzijds zijn neutronen bijzonder ongevoelig voor enkele metalen zoals aluminium of zelfs een zwaar metaal als lood. Hierdoor kunnen neutronen informatie opleveren in gevallen waar

andere NDT-technieken tekort schieten. Neutronentomografie heeft reeds zijn nut bewezen in allerlei vakgebieden zoals archeologie, geologie, biologie, luchtvaart. . . Momenteel blijft neutronentomografie nog grotendeels beperkt tot grote onderzoeksinstellingen vanwege het gebrek aan voldoende sterke en gemakkelijk inzetbare neutronenbronnen. Bovendien is het ruimtelijk oplossend vermogen (de resolutie) nog vrij beperkt ($\pm 200 \mu\text{m}$) in vergelijking met bestaande X-stralentechnieken, dit omwille van de detectortechnologie die voorhanden is en vanwege de aard van de neutronenbronnen. Niettemin is neutronentomografie als techniek volop in ontwikkeling en neemt het aantal opstellingen, de performantie en toepasbaarheid van bestaande opstellingen snel toe. De eerste commerciële neutronenbeeldvormingsdiensten duiken nu reeds op [13].

Neutronentomografie biedt voldoende potentieel om een standaard NDT techniek te worden in een ruim spectrum van toepassingen, zowel industrieel als wetenschappelijk. Tegelijk blijven er nog grote uitdagingen en is er nog veel ontwikkeling mogelijk. Dit alles maakt van neutronentomografie een interessant en uitdagend onderzoeksonderwerp. Daarom werd ervoor gekozen om dit doctoraatsonderzoek te richten op de verder ontwikkeling van neutronentomografie als beeldvormingstechniek en op de uitbreiding van het toepassingsgebied. Hiervoor dienden een ruim aantal experimentele tools te worden ontwikkeld, zowel software als hardware.

Resultaten van dit doctoraatsonderzoek

Het kader

Om de experimenten mogelijk te maken zijn er twee grote vereisten (naast een neutronenbron uiteraard). Vooreerst moet er een werkende opstelling ontwikkeld worden voor het registreren van de beelden. Dit omvat zowel hardware- als software-ontwikkeling. Ten tweede is er de nood aan software voor de reconstructie van de bekomen data. Deze is minstens zo belangrijk vermits tomografie een digitale beeldvormingstechniek is waarvan de uitkomst het resultaat is van computerberekeningen.

De experimentele opstelling

De basisopstelling voor elk tomografie-experiment bestaat uit de volgende onderdelen: een motorsysteem voor de positionering en rotatie van het sample en een scintillator die het schaduwbeeld van het sample omzet tot een zichtbaar signaal. Dit licht wordt vervolgens door een CCD-camera geregistreerd en gedigitaliseerd waarna het door de computer verwerkt wordt. Gedurende dit onderzoek werden acquisitie- en controlesoftware ontwikkeld die alle praktische aspecten van de uiteenlopende experimenten behelsden. Dit omvat de sturing en uitlezing van de camera, de aansturing van de

motoren, de bediening en uitlezing van allerlei randapparatuur zoals bundelmonitoren, shutters, counters en triggers. Verscheidene aspecten werden specifiek voor individuele experimenten ontwikkeld, zoals aangepaste acquisitie-sequenties voor tijdsafhankelijke experimenten of statistische procedures voor 'extreme low-light' experimenten. Er werd een stappenmotor-controller ontwikkeld die volledig software-gebaseerd is. Deze maakte een veel snellere en flexibelere sturing van de motoren mogelijk. Deze bewees zijn nut in een reeks experimenten rond hoge-snelheidstomografie van dynamische fenomenen. Het eindresultaat van al deze ontwikkelingen is een experimentele opstelling die meermaals bewezen heeft een hoge performantie en efficiëntie te koppelen aan de flexibiliteit die nodig is voor de sterk uiteenlopende experimentele omstandigheden.

De reconstructiesoftware

Na de registratie van de data moet deze 'gereconstrueerd' worden, wat inhoudt dat door middel van een reeks wiskundige berekeningen op basis van de bekomen 2D projecties een 3D volume van attenuatie-coëfficiënten wordt bekomen dat een representatie vormt van het onderzochte object. Dit vereist veel handmatige input van de gebruiker en vereist tevens veel rekentijd, al gauw van de orde tientallen minuten tot enkele uren op een degelijke reken-PC. Daarom werd Octopus ontwikkeld, een softwarepakket geschreven in de programmeeromgeving LabVIEW, waarmee vrijwel alle in dit werk getoonde reconstructies werden gerealiseerd. Octopus is geëvolueerd van een set eenvoudige scripts tot een volwaardig pakket met functies voor pre-processing, reconstructie en postprocessing van de data. Een server-client architectuur werd geïmplementeerd om de reconstructie te verdelen via een klassiek Ethernet-gebaseerd netwerk. Op die manier kunnen meerdere PC's meehelpen waardoor de reconstructietijden drastisch dalen. Er is tevens een volautomatische reconstructiemodus die enkel de ruwe projectiedata als input vraagt. Deze bleek van groot nut tijdens de experimenten rond hoge-snelheidstomografie van dynamische fenomenen. De grote hoeveelheden data zouden manueel niet te verwerken zijn geweest. De software is bruikbaar voor de meest voorkomende bundelgeometrieën zodat ze ook kan ingezet worden in andere domeinen dan neutronentomografie.

De experimentele resultaten

De eerste reeks experimenten vond plaats aan de Prompt Gamma Activation (PGA) bundellijn aan het Paul Scherrer Instituut (PSI) in Zwitserland. Het doel van het onderzoek was in de eerste plaats vertrouwd te raken met de techniek van neutronentomografie, en met de mogelijkheden en beperkingen ervan. De opstelling werd eerst grondig gekarakteriseerd en vervolgens werden allerlei samples gescand en de resultaten geëvalueerd. Op het vlak

van spatiale resolutie werd een grote verbetering bekomen door gebruik te maken van dunnere scintillatoren. Verder werd er geëxperimenteerd met een neutronenlens. Het was de bedoeling hiermee de oorspronkelijk parallelle neutronenbundel te focuseren in een 'brandpunt'. Dit fungeert dan als puntbron, waardoor een vergroting bekomen wordt van het schaduwbeeld. Hoewel de resultaten veelbelovend zijn is er verdere technologische ontwikkeling nodig om deze benadering nuttig te maken.

Vervolgens hebben we onze aandacht gericht op de informatie die vervat lag in de energie van de neutronen. Er werden experimenten uitgevoerd met een neutronen-snelheids-selector, een toestel waarmee uit een polychromatische neutronenbundel een relatief monochromatische bundel kan geselecteerd worden. Deze werd eerst grondig gekarakteriseerd en vervolgens werden allerlei tests uitgevoerd. Niettegenstaande de langere belichtingstijden werden enkele belangrijke voordelen aangetoond voor zowel radiografische als voor tomografische toepassingen. Het blijkt mogelijk om een hoger relatief beeldcontrast te bekomen en om betere kwaliteit tomografische reconstructies te krijgen. Verder kan er informatie uit de samples gehaald worden die met een gewone polychromatische bundel verloren gaat. Daarbij biedt deze techniek nog het bijkomende voordeel van een hogere spatiale resolutie door een collimerende werking van de selector. Tot slot werd aangetoond dat deze techniek in bepaalde gevallen kan gebruikt worden voor element-identificatie.

Een tweede reeks experimenten die steunde op de energie-informatie gebeurde aan een andere bundellijn aan het PSI, namelijk de TOPSI diffractometer. Daar werd een opstelling geïnstalleerd voor neutronen-topografie. Topografie is een techniek uit de X-stralenwereld om de oriëntatie van kristalvlakken te visualiseren door middel van diffractie. Het doel was diezelfde techniek ook met neutronen toe te passen. De extreem lage neutronenintensiteit die voor dit experiment beschikbaar was maakte dit een grote uitdaging. De oriëntatie van kristalvlakken in enkele kristallijne samples werd met succes gevisualiseerd. De oorspronkelijke bedoeling om de techniek uit te breiden tot topo-tomografie, waarbij een volledig 3D beeld van alle kristaloriëntaties wordt bekomen, was met de huidige opstelling niet haalbaar vanwege de urenlange belichtingstijden, maar het werd wel bewezen dat neutronentopo-tomografie in principe mogelijk is.

Een laatste reeks experimenten situeerde zich in het tijdsdomein. Tot nog toe werden steeds statische samples bestudeerd. De studie van dynamische fenomenen, zoals de beweging van vloeistoffen in poreuze materialen, is ook binnen de neutronenbeeldvorming heel actueel, maar is steeds beperkt tot radiografische opnames. Echte 3D tomografie van dynamische fenomenen was voor zover we weten, nog nooit verwezenlijkt. Daarom werd de bestaande opstelling geoptimaliseerd zodat aan veel hogere snelheid scans konden worden opgenomen. Deze opstelling werd geïnstalleerd aan de hoge intensiteit Neutrograph bundellijn aan het ILL in Grenoble (Frankrijk). Een

volledige tomografische scan kon verwezenlijkt worden in minder dan 10 seconden. Dit stelde ons in staat om de distributie van vloeistoffen in poreuze materialen in 3D te volgen met een tijdsresolutie van 10 seconden. Dit is voor zover we weten de eerste maal dat dit in 3D kon worden gedaan. De voordelen ten opzichte van vergelijkbare 2D technieken liggen voor de hand. Verscheidene toepassingen werden met succes bestudeerd, onder meer de behandeling van poreuze bouwstenen ter bescherming tegen water. Zowel het product als het water konden worden in beeld gebracht.

Outlook

Verbeteringen aan de opstelling

De huidige tomografie-opstelling kan op verschillende vlakken verder verbeterd worden. Op het vlak van de lenzen bestaan er nog meer lichtsterke (efficiëntere) lenzen. We zullen ook nieuwe neutronenscintillatoren testen naar hun efficiëntie en oplossend vermogen. Maar de grootste verbetering is mogelijk op vlak van de CCD-camera. We overwegen dan ook een vervanging van de huidige camera. Deze is bijna zes jaar oud en draagt de sporen van de tientallen experimenten in intense stralingsomgevingen, zowel met neutronen als X-stralen en gammastralen. Een nieuwe camera, zoals bijvoorbeeld de PCO1600, een opvolger van de door ons gebruikte camera, zou de huidige mogelijkheden sterk uitbreiden. Een veel kortere minimale belichtingstijd zou hoge-snelheidsexperimenten zoals doorlichting van werkende motoren mogelijk maken. Anderzijds kan de veel langere maximale belichtingstijd van meerdere dagen, in combinatie met de lagere donkerstroom, benut worden in experimenten met extreem lage lichtopbrengst. Dit zou tevens de topo-tomografie-experimenten kunnen mogelijk maken binnen redelijke tijdsspannes. Het hogere dynamisch bereik zou in alle gevallen leiden tot betere tomografische reconstructies vanwege de betere statistiek in de data. Tot slot bieden nieuwe camera's het voordeel dat grote hoeveelheden geheugen in de camera zelf kunnen worden voorzien. Op die manier zouden volledige tomografische scans kunnen opgenomen worden in de camera zelf aan heel hoge snelheid om daarna aan lagere snelheid te worden getransfereerd naar het geheugen of de harddisk van de PC. Met name voor dynamische tomografie zou dit de bewegingsartefacten sterk kunnen verminderen.

Software ontwikkeling

Ook de software zal verder ontwikkeld worden, met de klemtoon op de reconstructie-algoritmes vermits de reconstructie de meest tijdrovende stap blijft. De bestaande algoritmes zullen verder geoptimaliseerd worden. Momenteel onderzoeken we de mogelijke implementatie van algoritmes die de

computationele complexiteit reduceren van de huidige $O(N^3)$ tot $N^2 \log(N)$ (met N het aantal beeldpixels in 1 dimensie). Er bestaan verscheidene varianten van dergelijke algoritmes [78, 79, 80] en we zullen evalueren welke best geschikt zijn voor onze toepassingen en voor integratie in de reeds bestaande software. Verder zullen enkele nieuwe reconstructiemodes toegevoegd worden. Een eerste is zogenaamde 'limited angle tomografie' voor reconstructie van datasets waarbij niet over de gangbare 180 graden kan worden gescand maar slechts over een beperkt bereik. Dit vereist iteratieve algebraïsche reconstructie-algoritmes. Ten tweede zal er nog een algoritme ontwikkeld worden voor een belangrijke bundelgeometrie die nog niet ondersteund is, namelijk 'helicale scanning' [76]. Dit is een vorm van cone-beam scannen die een theoretische exacte reconstructie mogelijk maakt, daar waar de klassieke cone-beam acquisitie steeds een benaderende methode blijft. Tot slot voorzien we nog de implementatie van een aantal routines voor correctie van een aantal fenomenen die aanleiding geven tot reconstructie-artefacten. Zo is er o.a. beam-hardening, een gevolg van de verschillende absorptiekenmerken voor de verschillende energieën in een bundel. Dit geeft aanleiding tot verkeerd berekende attenuatiecoëfficiënten. Deze correctie is reeds geïmplementeerd, maar daarnaast zijn er nog o.a. metaal-artefacten, scattering-artefacten,...

Verdere experimenten

De experimenten rond dynamische tomografie zullen verdergezet worden. Momenteel is een verbeterde opstelling in ontwikkeling die het mogelijk zal maken om de opnametijd voor een volledige tomografie verder zal reduceren tot minder dan 3 seconden. Hiertoe zal afgestapt worden van de klassieke acquisitie-sequentie van rotatie-belichting-rotatie. In de plaats daarvan zal het sample continu draaien met een vaste snelheid, en zal de camera met geregelde intervallen extern getriggerd worden. Dit biedt het bijkomend voordeel dat het sample minder versnellingen ondergaat waardoor de geobserveerde fenomenen minder zullen beïnvloed worden. De nieuwe opstelling zal het toepassingsgebied verder uitbreiden en door de betere tijdsresolutie snellere fenomenen kunnen monitoren.

Naast de activiteiten rond neutrontomografie wordt momenteel ook hard gewerkt aan de uitbouw van een multifunctionele hoge resolutie X-stralen tomograaf. Dit toestel zal beantwoorden aan de sterk toenemende vraag naar niet-destructieve 3D beeldvorming met hoge resolutie, zowel vanuit de universiteit als daarbuiten. Het toestel zal een oplossend vermogen hebben van minder dan $1 \mu\text{m}$, resulterend in een 'detail detectability' van de orde van 250 nm. Anderzijds zullen door de modulaire opbouw en het ruime energiebereik van de gekozen X-stralenbuis (tot 160 keV) samples tot 20 cm groot kunnen gescand worden. Een dergelijk groot bereik in combinatie met een zeer hoog oplossend vermogen zal deze faciliteit uniek maken in

zijn soort. Het toepassingsgebied is enorm en omvat onder andere micro-elektronica, geologie, biologie, bouwkunde, etc. Deze faciliteit sluit perfect aan bij de mogelijkheden die reeds beschikbaar zijn aan de lineaire versneller. Daar kunnen samples vanaf 10 cm tot 50 cm gescand worden met hoge energie X-stralen (>1 MeV). De combinatie van deze beide opstellingen zal dit de meest functionele tomografiefaciliteit maken in België.

Bibliography

- [1] W. Mondelaers. *Productie en toepassing van intense elektronen- en fotonenbundels in het energiegebied tot 15 MeV*. PhD thesis, Universiteit Gent, 1999¹. 6, 164
- [2] M. Bertschy, J. Jolie, and W. Mondelaers. A tunable monochromatic gamma-ray source .1. Concept of the source. *Nucl. Instr. and Meth. B*, 95:431–436, march 1995. 7
- [3] M. Bertschy, J. Jolie, and W. Mondelaers. A tunable monochromatic gamma-ray source .2. Realisation of the RFCT geometry at the Ghent 15 MeV linac. *Nucl. Instr. and Meth. B*, 95:437–443, march 1995. 7
- [4] M. Bertschy, J. Jolie, and W. Mondelaers. A tunable monochromatic gamma-ray source .3. Feasibility study of heavy element tomography. *Nucl. Instr. and Meth. B*, 103:330–338, nov 1995. 7
- [5] M. Bertschy, J. Jolie, and W. Mondelaers. A tunable monochromatic gamma-ray source .4. The FCMT operation mode. *Nucl. Instr. and Meth. B*, 117:333–338, sep 1996. 7
- [6] Masschaele B., Jolie J., Mondelaers W., Materna T., Cauwels P., and Dierick M. Improvement of the tuneable monochromatic gamma-ray source at the 15 MeV linac of the University of Gent. *Nucl. Instr. and Meth. B*, 179:286–288, 2001. 7, 107
- [7] T. Materna, J. Jolie, W. Mondelaers, and B. Masschaele. Near K-edge measurement of the X-ray attenuation coefficient of heavy elements using a tuneable X-ray source based on an electron linac. *Radiation Physics and Chemistry*, 59:449–457, dec 2000. 7, 107
- [8] M. Bertschy, J. Jolie, and W. Mondelaers. Heavy-element tomography using tunable gamma-ray beams. *Applied Physics A*, 62:437–443, may 1996. 7

¹The last number(s) in each reference refers back to the citing page(s)

- [9] T. Materna, J. Jolie, and W. Mondelaers. Mapping elemental distributions of heavy elements using tunable gamma-ray beams. *Nucl. Instr. and Meth. B*, 149:141–146, jan 1999. 7, 107
- [10] T. Materna, J. Jolie, W. Mondelaers, B. Masschaele, V. Honkimaki, A. Koch, and T. Tschentscher. Uranium-sensitive tomography with synchrotron radiation. *Journal of Synchrotron Radiation*, 6:1059–1064 part 5, sep 1999. 8, 59, 86
- [11] T. Materna, J. Jolie, W. Mondelaers, B. Masschaele, V. Honkimaki, A. Koch, and T. Tschentscher. Heavy element sensitive tomographies using synchrotron radiation. *Applications of Accelerators in Research and Industry*, CP475, 1999. 8
- [12] Masschaele B., Baechler S., Cauwels P., Cloetens P., Dierick M., Jolie J., and Mondelaers W. Element sensitive X-ray micro tomography for determination of the metal diffusion in teeth with amalgam fillings. *Radiation Physics and Chemistry*, 61:625–626, june 2001. 8
- [13] <http://www.nray.com>. 9, 33, 165
- [14] <http://www.cost524.com/>. 13
- [15] Wilhelm Conrad Röntgen. On a new kind of rays. *Nature*, 53:274–277, 1896. 15
- [16] <http://www.xray.hmc.psu.edu/rci/centennial.html>. 15
- [17] Nobel Lectures. Physics 1901-1921, Elsevier Publishing Company, 1967. 15
- [18] J. Radon. Über die bestimmung von funktionen durch ihre integralwerte längs gewisser mannigfaltigkeiten. *Ber. Ver. Sächs. Akad. Wiss. Leipzig, Math-Phys. Kl.*, 69:262–277, April 1917. In German. An english translation can be found in S. R. Deans: *The Radon Transform and Some of Its Applications*, app. A. 16
- [19] G. N. Hounsfield. Computerized transverse axial scanning tomography: Part I description of the system. *British Journal of Radiology*, 46:1016–1022, 1973. 16
- [20] Nobel Lectures. Physiology or Medicine 1971-1980, World Scientific Publishing Co., 1992. 16, 33
- [21] Webb S. From the watching of the shadows, the origins of radiological tomography. *Bristol/New York: Adam Hilger*, 1990. 16
- [22] <http://www.siemensmedical.com>. 16

- [23] <http://www.feinfocus.com/>. 16
- [24] <http://www.microfocus-x-ray.com/>. 16
- [25] A. Takeuchi, Y. Suzuki, and H. Takano. *J. Synchrotron Rad*, 9:115, 2002. 17
- [26] Cherry S, Dahlbom M, and Hoffman EJ. Three-dimensional PET using a conventional multi-slice tomograph without septa. *Journal of Computer Assisted Tomography*, 15:655–668, 1991. 17
- [27] Townsend DW, Spinks T, Jones T, Geissbuhler A, Defrise M, Gilardi MC, and Heather J. Three-dimensional reconstruction of PET data from a multi-ring camera. *IEEE Transactions in Nuclear Sciences*, 36:1056–1066, 1989. 17
- [28] Gullberg G, Zeng G, Datz D, Christian P, Tung C, and Morgan H. Review of convergent beam tomography in SPECT. *Physics in Medicine and Biology*, 37:507–534, 1992. 17
- [29] V.A. Markel and J.C. Schotland. Symmetries, inversion formulas, and image reconstruction for optical tomography. *Physical Review E*, 70:56616–1–19, 2004. 17
- [30] York T. Status of electrical tomography in industrial applications. *JOURNAL OF ELECTRONIC IMAGING*, 10:608–619, 2001. 17
- [31] Deschamps F and Trampert J. Mantle tomography and its relation to temperature and composition. *PHYS EARTH PLANET IN*, 140:277–291, 2003. 17
- [32] Haltmeier M., Scherzer O., and Burgholzer P. et al. Thermoacoustic computed tomography with large planar receivers. *Inverse Problems*, 20:1663–73, 2004. 17
- [33] PRJ. Cornely. Flexible prior models: Three-dimensional ionospheric tomography. *RADIO SCIENCE*, 38:Art. No. 1087, 2003. 17
- [34] A. C. Kak and M. Slaney. Principles of Computerized Tomographic Imaging. *IEEE Press*, 1988. 19, 27, 29, 72
- [35] Anil K. Jain. Fundamentals of digital image processing. *Prentice Hall*, 1989. 24
- [36] Tuy H. An inversion formula for cone-beam reconstruction. *SIAM journal of Applied Mathematics*, 43:546–552, 1983. 32
- [37] Feldkamp L.A., Davis L., and Kress J. Practical cone beam algorithm. *Journal of the Optical Society of America*, 1:612–619, 1984. 32, 72

- [38] Grangeat P, Sire P, Guillemaud R, and La V. Indirect cone-beam threedimensional image reconstruction. *Studies in Health Technology and Informatics*, pages 29–52, 1997. 32
- [39] Noo F. Clackdoyle R, Defrise M. Early results on general vertex sets and truncated projections in cone-beam tomography. *Computational radiology and imaging: therapy and diagnostics, IMA Volumes in Mathematics and its Applications, Berlin:Springer*, pages 113–136, 1999. 32
- [40] E.H. Lehmann et al. Status and prospects of neutron tomography in Europe. *Proc. 15th World Conference on Non-destructive testing, Rome (Italy)*, 2000. 33
- [41] Kallman H. *Research*, 1:254, 1948. In J. of Physics E, Scientific Instruments, volume 5, pages 497510. 1972. 33
- [42] Chadwick J. Letter to the editor: Possible existence of a neutron. *Nature*, 129:312, 1932. 33, 34
- [43] W. Boyle and G. Smith. Charge coupled semiconductor devices. *Bell System Technical Journal*, 49:587–593, 1970. 33, 153
- [44] B. Schillinger. *Neue Entwicklungen zu Radiographie und Tomographie mit thermischen Neutronen und zu deren routinemaessigem Einsatz*. PhD thesis, Technische Universitaet München, 1999. 33
- [45] K. et al. Hagiwara. Review of particle physics. *Physical Review D*, 66:010001+, 2002. 34
- [46] <http://physics.nist.gov/PhysRefData/Xcom/Text/XCOM.html>. 35
- [47] E.B. Saloman, J.H. Hubbell, and J.H. Scofield. X-ray attenuation cross sections for energies 100 ev to 100 kev and elements $z = 1$ to $z = 92$. *Atomic Data and Nucl. Data Tables*, 38:1, 1988. 35
- [48] E.B. Saloman and J.H. Hubbell. X-ray attenuation coefficients (total cross sections): Comparison of the experimental data base with the recommended values of henke and the theoretical values of scofield for energies between 0.1-100 kev. *NBSIR*, pages 86–3431, 1986. 35
- [49] F. H. Attix. Introduction to radiological physics and radiation dosimetry. *Wiley-Interscience*, 1986. ISBN 0-471-01146-0. 35
- [50] Hughes D. J. and Schwartz R. B. Neutron cross sections. *BENL-325, Brookhaven Natl. Lab.*, 1958. 36

- [51] Kardjilov N, Lehmann E, Steichele E, and et al. Phase-contrast radiography with a polychromatic neutron beam. *Nucl. Instr. and Meth. A*, 527:519–530, 2004. 36
- [52] S. Baechler et al. Non-destructive analysis of a bulky sample from a natural fossil reactor. *Journal of Radioanalytical and Nuclear Chemistry*, 250:39–45, 2001. 38
- [53] <http://sinq.web.psi.ch/>. 38
- [54] <http://www.ill.fr/>. 38
- [55] <http://www.frm2.tu-muenchen.de/>. 39
- [56] <http://www.hmi.de/bensc/>. 39
- [57] <http://www.isis.rl.ac.uk/>. 39
- [58] <http://www.bnc.hu/>. 39
- [59] <http://www.fz-juelich.de/portal/>. 39
- [60] <http://www.gkss.de/>. 39
- [61] <http://www-llb.cea.fr/>. 39
- [62] <http://www.ujf.cas.cz/>. 39
- [63] <http://lansce.lanl.gov/>. 40
- [64] <http://www.science.mcmaster.ca/mnr/>. 40
- [65] <http://www.ncnr.nist.gov/>. 40
- [66] <http://hanaro2005.kaeri.re.kr/>. 40
- [67] <http://www.jaeri.go.jp/english/>. 40
- [68] <http://www.necsa.co.za/index.asp>. 40
- [69] <http://www.sns.gov/>. 40
- [70] P. Vontobel, E.H. Lehmann, A. Ellenberger, and E. Manfrin. Neutron tomography setup at SINQ: Status and first results. *PSI-Annual-Report 1999; Annex VI*, page 64, 1999. 41
- [71] M Spahn, V Heer, and R Freytag. Flat-panel detectors in X-ray systems. *RADIOLOGE*, 43:340, 2003. 42
- [72] WA Kalender. The use of flat-panel detectors for ct imaging. *RADIOLOGE*, 43:379–387, 2003. 42

- [73] Samei E and Flynn MJ. An experimental comparison of detector performance for direct and indirect digital radiography systems. *MEDICAL PHYSICS*, 30:608–622, 2003. 42
- [74] M. Estermann, E. Lehmann, G. Frei, and P. Vontobel. The performance of an Amorphous Silicon Flat Panel for neutron imaging under the conditions at NEUTRA. *PSI Scientific Report 2003*, III, 2003. 43
- [75] <http://www.iana.org/assignments/port-numbers>. 57
- [76] Henrik Turbell. *Cone-Beam Reconstruction Using Filtered Backprojection*. PhD thesis, Institute Of Technology, Linköpings Universitet, 2001. 72, 145, 169
- [77] Sorokin Nikolay. *An FPGA-based 3D Backprojector*. PhD thesis, Universität des Saarlandes, 2003. 72
- [78] S. Basu and Y. Bresler. $O(N^2 \log_2 N)$ filtered backprojection reconstruction algorithm for tomography. *IEEE Trans. on Image Processing*, 9:17601772, 2000. 75, 144, 169
- [79] Stefan Nilsson. *Application of fast backprojection techniques for some inverse problems of integral geometry*. PhD thesis, Department of Mathematics, Linkping University, Sweden, 1997. 75, 144, 169
- [80] Potts D. and Steidl G. A new linogram algorithm for computerized tomography. *IMA Journal of Numerical Analysis*, 21:769–782, 2001. 75, 144, 169
- [81] Baechler S., Masschaele B., Cauwels P., Dierick, M. Jolie J., Materna T., and Mondelaers W. The new cold neutron tomography set-up at SINQ. *Nucl. Instr. and Meth. A*, 481:397–405, 2002. 94
- [82] M. A. Kumahkov and V. A. Sharov. A neutron lens. *Nature*, 357:390–391, 1992. 95
- [83] Masschaele B., Baechler S., Cauwels P., Dierick M., Jolie J., and Mondelaers W. First results of micro-neutron tomography by use of a focussing neutron lens. *Radiation Physics and Chemistry*, 61:623–624, 2001. 99
- [84] G. Kühne, internal communication. 101, 102
- [85] T. Materna, S. Baechler, G. Kühne, R. Erne, E. Lehmann, and M. Dierick. Set-up of CCD based detection system at the NCR beamline (PSI). *COST 524 STSM Report*, pages 1–12, 2001. 105
- [86] Wagner V., Friedrich H., and Wille P. Performance of a high-tech neutron velocity selector. *PHYSICA B*, 180:938–940, june 1992. 108

- [87] Friedrich H., Wagner V., and Wille P. A high-performance neutron velocity selector. *PHYSICA B*, 156:547–549, jan-feb 1989. 108
- [88] <http://sans.web.psi.ch/SANSDoc/node35.html#nvs>. 113
- [89] Experimental Nuclear Reaction Data File (EXFOR [CSISRS]), <http://www-nds.iaea.or.at/exfor/>. 113, 114
- [90] Baechler S., Kardjilov N., Dierick M., Jolie J., Kuhne G., Lehmann E., and Materna T. New features in cold neutron radiography and tomography - part 1: Thinner scintillators and a neutron velocity selector to improve the spatial resolution. *Nucl. Instr. and Meth. A*, 491:481–491, 2002. 118
- [91] Kardjilov N., Baechler S., Basturk M., Dierick M., Jolie J., Lehmann E., Materna T., Schillinger B., and Vontobel P. New features in cold neutron radiography and tomography - part 2: Applied energy-selective neutron radiography and tomography. *Nucl. Instr. and Meth. A*, 501:536–546, 2003. 118
- [92] M. Schlenker, J. Baruchel, and R. Perrier de la Bathie. Neutron-diffraction section topography: Observing crystal slices before cutting them. *J. Appl. Phys.*, 46:2845–2848, July 1975. 119
- [93] A. Boeuf, S. Lagomarsino, F. Rustichelli, J. Baruchel, and M. Schlenker. White beam neutron topography. *Phys. Stat. Sol.*, A 31:K91, 1975. 119
- [94] J. Baruchel, M. Schlenker, A. Zarka, and J. F. Petroff. Neutron diffraction topographic investigation of growth defects in natural lead carbonate single crystals. *Journal of Crystal Growth*, 44:356–362, 1978. 119
- [95] Masami Ando and Sukeaki Hosoya. Q-switch and polarization domains in antiferromagnetic Chromium observed with neutron-diffraction topography. *Phys. Rev. Lett.*, 29:281–285, 1972. 119
- [96] Wroblewski T, Jansen E, Schfer W, and Skowronek R. Neutron imaging of bulk polycrystalline materials. *Nuclear Instruments and Methods in Physical Research A*, 423:428–434, 1999. 119
- [97] T. Wroblewski, J. Almansttter, O. Clauss, M. Moneke, T. Pirling, and P. Schade. Strain mapping by diffraction imaging. *Materials Science and Engineering A*, 288:126–131, sept 2000. 119
- [98] N. Kardjilov, S. Baechler, M. Dierick, B. Masschaele, and J. Stahn. Neutron topography at TOPSI. *TUM Annual Report, Institute for Experimental Physics E21*, pages 55–56, 2002. 127

- [99] N. Kardjilov, S. Baechler, M. Dierick, B. Masschaele, and J. Stahn. Neutron topography at TOPSI. *PSI Scientific Report 2002*, 3:61, 2002. 127
- [100] Lehmann E.H. and Vontobel P. Investigation of hydrogen distributions in various base materials by neutron radiography methods. *Proc. 15th World Conference on Non-destructive testing (Rome)*, Oct 2000. 129
- [101] Balaskó M. and Sváb E. Dynamic neutron radiography instrumentation and applications in Central Europe. *Nuclear Instruments & Methods in Physics Research A*, 377:140–143, 1996. 129
- [102] Balaskó M., Körösi F., and Sváb E. Modelling of oil infiltration and distribution in sandstone applying dynamic neutron radiography. *Abstract Volume, Sixth World Conference on Neutron Radiography (Osaka, Japan)*, 36:200–201, May 1999. 129
- [103] D. A. Lockington and J.-Y. Parlange. Anomalous water absorption in porous materials. *J. Phys. D: Appl. Phys.*, 36:760–767, 2003. 129
- [104] Abd El-Ghany El Abd and Jacek J Milczarek. Neutron radiography study of water absorption in porous building materials: anomalous diffusion analysis. *J. Phys. D: Appl. Phys.*, 37:2305–2313, 2004. 129
- [105] Darnault C.J.G., D.A. DiCarlo, T.W.J. Bauters, A.R. Jacobson, J.A. Throop, C.D. Montemagno, J.-Y. Parlange, and T.S. Steenhuis. Measurement of fluid contents by light transmission in transient three-phase oil-water-air systems in sand. *Water Resour. Res.*, 37:1859–1868, 2001. 129
- [106] DiCarlo D.A., T.W.J. Bauters, T.S. Steenhuis, J.-Y. Parlange, and B.R. Bierck. High-speed measurements of three-phase flow using synchrotron X-rays. *Water Resour. Res.*, 33:569–576, 1997. 129
- [107] Pleinert H. and Degueldre C. Neutron radiographic measurement of porosity of crystalline rock samples: a feasibility study. *J. Cont. Hyd.*, 19:29–46, 1995. 129
- [108] [Rilem Test Method 11.4](#). 134
- [109] B. Masschaele, M. Dierick, L. Van Hoorebeke, V. Cnudde, and P. Jacobs. The use of neutrons and monochromatic X-rays for non-destructive testing in geological materials. *Environmental Geology*, 46:486–492, aug 2004. 140
- [110] M. Dierick, J. Vlassenbroeck, B. Masschaele, V. Cnudde, L. Van Hoorebeke, and A. Hillenbach. High speed neutron tomography of dynamic processes. *Proceedings of the 5th International Topical Meeting on Neutron Radiography (ITMNR-5)*, sep 2004. 140

- [111] <http://www.rad-icon.com/ShadoBox.htm>. 144
- [112] Materna T., Baechler S., Jolie J., Masschaele B., Dierick M., and Kardjilov N. The cold neutron tomography set-up at SINQ. *Nucl. Instr. and Meth. A*, 525:69–73, 2004. 145
- [113] P. Kudejova, Th. Materna, J. Jolie, A. Tuerler, S. Baechler, Zs. Kasztovszky, Zs. Rvay, and T. Belgia. On the construction of a new instrument for cold-neutron prompt gamma-ray activation analysis at the frm ii. *J. Radioanal. Nucl. Chem.*, 2005. accepted for publication. 145
- [114] Concepts in Digital Imaging Technology, <http://micro.magnet.fsu.edu/primer/digitalimaging/>. 153
- [115] Roper Scientific CCD Primer, <http://www.roperscientific.de/theory.html>. 153